Titre: Title:	Low Profile and Multiband Electromagnetic Bandgap Antennas for Avionics Applications
Auteur: Author:	Omar Masood Khan
Date:	2025
Type:	Mémoire ou thèse / Dissertation or Thesis
Référence: Citation:	Khan, O. M. (2025). Low Profile and Multiband Electromagnetic Bandgap Antennas for Avionics Applications [Thèse de doctorat, Polytechnique Montréal]. PolyPublie. https://publications.polymtl.ca/66936/

POLYTECHNIQUE MONTRÉAL
affiliée à l'Université de Montréal

Low Profile and Multiband Electromagnetic Bandgap Antennas for Avionics Applications

OMAR MASOOD KHAN
Département de génie électrique

Thèse présentée en vue de l'obtention du diplôme de *Philosophiæ Doctor*
Génie électrique

Juillet 2025

POLYTECHNIQUE MONTRÉAL
affiliée à l'Université de Montréal

Cette thèse intitulée :

Low Profile and Multiband Electromagnetic Bandgap Antennas for Avionics Applications

présentée par **Omar Masood KHAN**
en vue de l'obtention du diplôme de *Philosophiæ Doctor*
a été dûment acceptée par le jury d'examen constitué de :

Chahé NERGUIZIAN, président
Elham BALADI, membre et directrice de recherche
Jean-Jacques LAURIN, membre et codirecteur de recherche
Ke WU, membre
Halim BOUTAYEB, membre externe

DEDICATION

To my dear Parents, Teachers, Family and Friends . . .

ACKNOWLEDGEMENTS

Firstly, I would like to thank my supervisor and mentor Professor Jean-Jacques Laurin, for giving me an opportunity to work on this project, for providing me a vision to identify the problems, for teaching me invaluable knowledge to understand difficult concepts, for trusting and encouraging me for the new ideas and initiatives, and for always being very patient with me in all the phases of my research and thesis in this challenging field of avionics. I would also like to thank my supervisor Professor Elham Baladi, for all the prompt support she has given to me.

I would also like to thank Professor Chahé Nerguizian, Professor Ke Wu and Professor Halim Boutayeb, for taking time to read my thesis and for evaluations and valuable feedback.

I would like to thank all former and current Poly-Grames Research Center staff members, Traian Antonescu, Maxime Thibault, Steve Dube, and Jean-Sebastien Decarie, for their technical skills, support and working in the completion of this project.

I would like to thank Professor Rene Jr Landry, Jean Marc Gagné and their team from École de technologie supérieure (ÉTS), for working together in our research project and for providing their technical and logistics support.

I would also like to thank Dr. Reza Shamsaee Malfajani, from Poly-Grames Research Center, for his expertise in testing and measurements.

Last but not the least, I would like to thank my Parents, without there encouragement it would not have been possible. And I would also like to thank my Family and Friends, for their support throughout the time of this project.

RÉSUMÉ

Les antennes d'avion présentent de nombreux défis de conception, car leur placement à l'extérieur de la cellule augmente la traînée, la consommation de carburant, les risques d'interférences électromagnétiques et peut affecter l'interopérabilité des systèmes avioniques. Cette thèse présente la conception d'antennes multibandes à profil bas réduisant le nombre d'antennes placées sur la cellule et pouvant être intégrées à une radio avionique logicielle (SDAR) gérant les radios avioniques sur une plateforme matérielle unique. Une antenne radioaltimètre (RadAlt) présente de faibles niveaux de lobes secondaires et des caractéristiques d'isolation élevées sur toute la bande de fréquences de fonctionnement de 4,2 GHz à 4,4 GHz grâce à la conception d'un réseau de patchs empilés avec une structure de bande interdite électromagnétique unidimensionnelle circulaire conçue pour supprimer les courants de surface dans le plan H. Une analyse de traînée est réalisée et démontre que l'antenne RadAlt à profil bas proposée a un effet minimal sur la traînée globale de l'avion. Un concept d'antenne multibande est présenté pour les équipements de mesure de distance (DME), les systèmes anticollision (TCAS), la surveillance dépendante automatique en diffusion (ADS-B) et les applications RadAlt. Des configurations à un ou deux ports sont proposées pour l'antenne multibande. Des rayonnements omnidirectionnels sont obtenus pour les systèmes TCAS, DME et ADS-B dans la bande de fréquences de 0,96 GHz à 1,215 GHz, en concevant un résonateur à cavité alimenté par sonde. Les rayonnements directionnels sont réalisés en plaçant un réseau de patchs sur les couches supérieures de la cavité pour un rayonnement directionnel adapté aux applications RadAlt. Tout d'abord, un concept d'antenne à deux ports est réalisé en fournissant deux alimentations isolées pour le réseau de patchs et la cavité. En alternative, et dans le contexte d'un système radio basé sur SDAR, une antenne monoport est réalisée en concevant un répartiteur de puissance tridimensionnel pour alimenter la cavité inférieure et le réseau de patchs supérieur avec un seul port d'alimentation. Une structure à bande interdite électromagnétique est conçue et placée à l'intérieur de la cavité afin de supprimer le signal RadAlt. La réponse en fréquence et les diagrammes de rayonnement des antennes fabriquées sont mesurés en chambre anéchoïde et des essais en vol sont effectués pour vérifier la validité des performances de l'antenne réelle. Enfin, un concept d'antenne à profil bas pour système d'atterrissage aux instruments (ILS) est proposé pour les applications de descente avec une fréquence opérationnelle comprise entre 329 MHz et 335 MHz. Une structure à bande interdite électromagnétique est conçue et placée sous une antenne papillon et au-dessus du plan de masse afin de supprimer les réflexions du plan de masse. L'antenne à profil bas est placée sur des surfaces d'avion courbes et larges afin de démontrer ses caractéristiques de rayonnement.

Les antennes multi-bandes et à profil bas conçues proposent un concept d'antenne unique pour plusieurs systèmes avioniques de DME, TCAS, ADS-B et RadAlt et sont adaptées pour être intégrées aux radios avioniques définies par logiciel.

ABSTRACT

Aircraft antennas presents many design challenges as placing the antennas outside the airframe of the aircraft increases drag, fuel consumption, electromagnetic interference hazards and can effect the avionics systems interoperability. This thesis presents design of low profile and multiband antenna concepts that reduces the number of antennas placed on the aircraft airframe and can be integrated with software defined avionics radio (SDAR) managing avionics radios in a single hardware platform. A Radio Altimeter (RadAlt) antenna is presented with low sidelobe levels and high isolation characteristics in the whole frequency band of operation from 4.2 GHz to 4.4 GHz by designing stacked patch array with circular one-dimensional electromagnetic bandgap structure designed for suppressing surface currents in H-plane. A drag analysis is performed and it is demonstrated that the proposed low profile RadAlt antenna has minimal effect on the overall drag of the aircraft. A multiband antenna concept is presented for Distance Measuring Equipment (DME), Traffic Collision Avoidance System (TCAS), Automatic Dependent Surveillance-Broadcast (ADS-B) and RadAlt applications. One-port and two-port design configurations are proposed for the multiband antenna. Omnidirectional radiations are achieved for TCAS, DME and ADS-B system in the frequency band of 0.96 GHz to 1.215 GHz, by designing a probe-fed cavity resonator and directional pattern radiations are realized by placing a patch array on the upper layers of the cavity for directional pattern radiation suitable for the RadAlt applications. Firstly a two-port antenna concept is realized by providing 2 isolated feeding for the patch array and cavity. As an alternative, and in the context of SDAR based radio system, a one-port antenna is realized by designing three-dimensional power splitter for providing excitations for both the lower cavity and upper patch array with single feeding port. Electromagnetic bandgap structure is designed and placed inside the cavity for suppressing RadAlt signal within the cavity. Frequency response and radiation patterns are measured in anechoic chamber for the fabricated antennas and flight test is done for the validity of antenna performance during actual flight. Finally, an Instrument Landing System (ILS) low profile antenna concept is proposed for glideslope applications with operational frequency from 329 MHz to 335 MHz. An electromagnetic bandgap structure is designed and placed below a bowtie antenna and above the ground plane for suppressing reflections from ground plane. The low profile antenna is placed on curved and large aircraft surfaces for demonstrating the radiation characteristics of the antenna. The designed multiple band and low profile antennas propose single antenna concept for multiple avionics systems of DME, TCAS, ADS-B and RadAlt and are suitable to be integrated with the software-defined avionics radios.

TABLE OF CONTENTS

DEDICATION iii

ACKNOWLEDGEMENTS iv

RÉSUMÉ v

ABSTRACT vii

TABLE OF CONTENTS viii

LIST OF TABLES x

LIST OF FIGURES xi

LIST OF SYMBOLS AND ABBREVIATIONS xvii

CHAPTER 1 INTRODUCTION 1
- 1.1 Motivation and Background 1
- 1.2 Thesis Objectives 2
- 1.3 Methodology 3
- 1.4 Thesis Outline 4

CHAPTER 2 LITERATURE REVIEW 7
- 2.1 Background 7
- 2.2 Aircraft Antennas Siting Design 7
- 2.3 Aircraft Antenna Types 9
- 2.4 Radio Altimeter Antennas 11
- 2.5 Distance Measuring Equipment Antennas 12
- 2.6 Traffic Collision Avoidance System Antennas 15
- 2.7 Instrument Landing System Antennas 18
- 2.8 Electromagnetic Bandgap Structures for Antenna Applications 18
- 2.9 Conclusion 20

CHAPTER 3 ARTICLE 1: HIGH ISOLATION AND BAND ENHANCED RADIO ALTIMETER ANTENNA FOR AVIONICS APPLICATIONS 22
- 3.1 Abstract 22

3.2 Introduction 22
3.3 Antennna Design 24
3.4 Layered 1D EBG Unit Cell Design and Analysis 26
3.5 Simulation and Analysis 27
3.6 Conclusion 35

CHAPTER 4 ARTICLE 2: MULTIBAND DISTANCE MEASURING EQUIPMENT, TRAFFIC COLLISION AVOIDANCE SYSTEM AND RADIO ALTIMETER ANTENNA FOR AVIONICS APPLICATIONS 36
4.1 Abstract 36
4.2 Introduction 36
4.3 Antenna Design 38
4.4 Feeding Structures 40
4.5 EBG Unit Cell and Layer Design and Analysis 43
4.6 Simulation and Measurements 49
4.7 Conclusion 54

CHAPTER 5 LOW PROFILE INSTRUMENT LANDING SYSTEM BOWTIE ANTENNA 55
5.1 Introduction 55
5.2 Bowtie Antenna Design 57
5.3 Unit Cell EBG Design and Analysis 62
5.3.1 Interdigital EBG 62
5.3.2 Multilayered 1D EBG: Addendum to Chapter 3 63
5.4 Coplanar Waveguide Balun Feed Design 64
5.5 Antenna Analysis on Large Metal Surface 67
5.6 Antenna Analysis on Conformal and Aircraft Metal Surface 68
5.7 Conclusion 72

CHAPTER 6 CONCLUSION 73
6.1 Summary of Works 73
6.2 Future Research 75

REFERENCES 76

LIST OF TABLES

Table 1.1	Avionics Systems Antenna Frequency Bands and Radiation Pattern Specifications [1–8].	4
Table 3.1	Performance comparison of proposed antenna with similar published papers and commercial products. "-" indicates non available data. . .	29
Table 3.2	Measured and simulated gain and sidelobe levels of the proposed antenna	33

LIST OF FIGURES

Figure 1.1 Details of the antenna placement in aircraft. Adapted from [9], p. 100. 2

Figure 2.1 Summary of the antenna siting design on the aircraft. 8

Figure 2.2 Aircraft antenna types [9], (a) Dipole antenna, (b) Slot antenna, (c) Blade antenna, (d) Reflector antenna, (e) Monopole antenna, (f) Loaded monopole antenna T-shaped, (g) Disc loaded monopole antenna, (h) Helical antenna, (i) Spiral antenna, (j) Array antenna, (k) Patch antenna, and (l) Slotted waveguide array antenna. 10

Figure 2.3 Radio altimeter antennas, (a) Triplexer antenna for RadAlt, WLAN and ISM bands [10], (b) Triplexer antenna frequency response [10], (c) Two layered Radio Altimeter antenna [11], (d) Frequency response [11], (e) RadAlt antenna mounted under aircraft [12], and (f) Commercial RadAlt antenna and frequency response [13] 12

Figure 2.4 Low profile omnidirectional antennas, (a) Wideband L probe fed patch antenna [14], (b) L probe patch antenna frequency response [14], (c) Monopole wire patch antenna [15], (d) Monopole wire patch antenna frequency response [15], (e) Low profile monopole patch antenna [16], (f) Monopole patch antenna frequency response [16], (g) Loop array monopole antenna [17], and (h) Loop array monopole antenna frequency response [17]. 13

Figure 2.5 Distance measuring equipment antennas, (a) Low profile wideband monopole antenna [18], (b) Low profile wideband antenna frequency response [18], (c) Printed DME antenna [19], (d) Printed DME antenna frequency response [19], (e) Cavity backed nonprotruding antenna [20], (f) Cavity backed antenna frequency response [20], (g) DME antenna mounted under aircraft [21], and (h) Low profile DME antenna [22]. . 14

Figure 2.6 Traffic Collision and Avoidance System antennas, (a) Multiport directional TCAS antenna [23], (b) Multiport antenna radiation patterns in various directions [23], (c) TCAS antenna with beam switching design [24], (d) Beam switching TCAS antenna frequency response [24], (e) TCAS antenna mounted on aircraft [25], (f) TCAS commercial low profile antenna [26], and (g) TCAS commercial blade antenna [27]. . . 16

Figure 2.7 Instrument Landing System antennas, (a) ILS Marker beacon antenna mounted at the lower fuselage of aircraft [21], (b) Commercial Marker antenna [28], (c) ILS Glideslope and Localizer antennas installed at the nose of large aircraft [29], (d) ILS Glideslope and Localizer antennas zoomed image [29], (e) Commercial ILS localizer antenna [30], (f) Commercial ILS Glideslope antenna [31], (g) ILS Localizer and Glideslope antenna on tail of smaller aircraft, and (h) Commercial ILS localizer and glideslope antenna [32]. 17

Figure 2.8 Electromagnetic bandgap structures, (a) Side and top views of the top patches connected with ground plane with metallic vertical vias [33], (b) Uniplanar compact bandgap periodic metal sheet and unit cell structure [34], (c) Interdigital periodic metallic layer and unit cell structure, [35], (d) EBG superstrate layer on antenna elements, [36], (e) Slotted EBG, [37], and (f) EBG layer below slotted dipole. [38]. . 19

Figure 2.9 Electromagnetic bandgap antenna applications [33], (a) Vertical monopole antenna on ground plane generating surface waves, (b) Suppressed surface waves using EBG, (c) Radiation pattern vertical monopole antenna on ground plane with nulls and lobes, (d) Smoothed radiation pattern vertical monopole using EBG, (e) Patch antenna on metal ground plane, (f) Patch antenna on EBG, (g) Patch antenna radiation pattern with and without EBG, (h) Horizontal antenna on ground plane, (i) Horizontal antenna on EBG, (j) Radiation pattern of horizontal antenna with and without EBG. 20

Figure 3.1 Proposed ringed stacked radio altimeter antenna (a) Perspective view with dimensions, DA=135.10 mm, DV=2 mm, PL=22.62 mm, PW=15.3 mm, PPL=19.69 mm, PPW=27.21 mm, LW=1.41 mm, TW=2.83 mm, IL=3.50 mm, SH=1.575 mm, (b) Side view. 23

Figure 3.2 Detailed view of proposed ringed stacked radio altimeter antenna. . . 24

Figure 3.3 Proposed 1D layered ringed EBG unit cell diagram and labels, RL3=11.85 mm, RW3=4.42 mm, Rl2=3.0 mm, RW2=4.42 mm, RL1=3.0 mm, RW1=4.42 mm, RL4=5.5 mm, RV=2.0 mm, SH=1.575 mm, RP2= 9.95 mm, RP1=8.0 mm. 25

Figure 3.4 Simulated 1D ringed EBG unit cell analysis for ring length. 26

Figure 3.5 Simulated 1D ringed EBG unit cell analysis for via. 26

Figure 3.6 Simulated complex E-fields of proposed unit cell of one dimensional three layered ringed and via EBG (a) 3.8 GHz, (b) 4.0 GHz, (c) 4.1 GHz, (d) 4.2 GHz, (e) 4.3 GHz, (f) 4.4 GHz, (g) 4.5 GHz, (h) 4.9 GHz, (i) 6.0 GHz. 28
Figure 3.7 Simulated and measured return loss response of proposed antenna. . . 29
Figure 3.8 Measured isolation of proposed antenna. 30
Figure 3.9 Simulated surface currents of proposed antenna at 4.3 GHz, (a) without metallic vias and circular rings, (b) with metallic vias and circular rings. 30
Figure 3.10 Proposed ringed radio altimeter antenna fabricated layers (a) Middle, (b) Top and (c) Bottom. 31
Figure 3.11 Proposed stacked antenna fabricated views (a) Top and (b) Bottom. . 31
Figure 3.12 Measured and simulated 2D H-plane radiation patterns of proposed antenna and measurement setup. 32
Figure 3.13 Measured co and cross polarization H-Plane radiation patterns 33
Figure 3.14 CST simulated 3D radiation pattern of proposed antenna at 4.3 GHz. 34
Figure 3.15 Setup used for drag coefficient computation in OpenVSP software of antennas placed under Cessna 210 fuselage, (a) Top View, (b) bottom view. 34
Figure 4.1 Proposed single port distance measuring equipment and radio altimeter antenna perspective view with dimensions, MD = 182.4 mm, RD = 135.1 mm, FD = 19 mm, VP = 63.5 mm, VD = 3.175 mm, SH = 1.575 mm and RH = 9.52 mm. 38
Figure 4.2 Detailed view of proposed hybrid distance measuring equipment and radio altimeter antenna (a) Dual Port, (b) Single Port. 39
Figure 4.3 Proposed 2-port antenna feeding design, (a) Feed placement, (b) Detail zoomed view. 41
Figure 4.4 Proposed 1-port antenna 3D power splitter design, (a) Power splitter placement, (b) Zoomed view labeled, (c) Side view labeled, (d) Dimensions, FD = 19 mm, FR = 4.1 mm, FL = 1.5 mm, FV = 1.5 mm and FG = 8.2 mm. 42
Figure 4.5 Simulated frequency response of 2-port antenna and 1-port antenna with and without EBG. The required 10-dB return loss bands are shaded in blue. 43
Figure 4.6 EBG layer design and placement within cavity. 44
Figure 4.7 Designed EBG unit cell, (a) Labeled diagram, (b) Analysis for patch length AL. 45

Figure 4.8 Simulated 3D gain of proposed single port antenna at 4.3 GHz, (a) Without EBG, (b) With EBG. 46
Figure 4.9 Simulated maximum surface currents of the proposed single port antenna at 4.3 GHz, (a) Without EBG, (b) With EBG. 47
Figure 4.10 Simulated frequency response analysis for optimizing DME (blue shaded band), TCAS (green shaded band) and ADS-B (red shaded band) frequency bands in one-port antenna, (a) Diameter of top cavity patch MD on layer M6, (b) Cavity via placement radius from center VP, and (c) Diameter of the splitter outer ring FD on metallic layer M5. . . . 48
Figure 4.11 Simulated single port antenna omnidirectional 3D gain patterns for the DME, TCAS and ADS-B applications 49
Figure 4.12 Proposed 1-port antenna maximum surface currents at (a) 0.96 GHz , (b) 1.030 GHz, (c) 1.090 GHz, (d) 1.215 GHz. 50
Figure 4.13 Proposed antenna fabricated layers, (a) Top ring M12 above substrate S7, (b) Connecting rings M11 below substrate S7, (c) Parasitic patches M10 above substrate S6, (d) Connecting rings M9 below substrate S6, (e) Patch array M8 above substrate S5, (f) RadAlt ground M7 below substrate S5, (g) Cavity top M6 above substrate S4, (h) Splitter M5 for 1-port antenna above substrate S3, (i) Splitter ground for 1-port antenna below substrate S3, (j) Feed patch for 2-port antenna above substrate S3, (k) Rexolite layer S2, and (l) EBG layer above substrate S1. 51
Figure 4.14 Measured frequency responses of the 1-port and 2-port proposed antennas. Required 10-dB return losses are shaded in blue. 52
Figure 4.15 Measured and simulated 2D radiation patterns of proposed antennas; RadAlt Band (a) 2-port antenna, (b) 1-port antenna; DME, TCAS and ADS-B bands (c) 2-port antenna phi 0 degrees, (d) 1-port antenna phi 0 degrees, (e) 2-port antenna phi 90 degrees, (f) 1-port antenna phi 90 degrees, (g) Measurement setup in compact range chamber for RadAlt band, and (h) Measurement setup in Satimo starlab near-field system for DME, TCAS and ADS-B bands. 53
Figure 5.1 Proposed low profile IDC EBG bowtie antenna with dimensions, BL = 302.00 mm, BW = 160.00 mm, SL = 512.96 mm, SW = 256.48 mm, BH = 3.15 mm and SH = 12.60 mm. 55
Figure 5.2 Proposed IDC EBG bowtie antenna layers details. 56

Figure 5.3 Proposed antenna on metal ground (a) Without EBG, (b) With IDC EBG, and (c) Simulated frequency response of proposed antenna, with and without IDC EBG 57
Figure 5.4 Proposed antenna design (a) Dipole antenna, (b) Bowtie antenna. . . 58
Figure 5.5 Simulated frequency response analysis of dipole antenna length. . . . 59
Figure 5.6 Simulated frequency response analysis of proposed bowtie antenna length and width. 59
Figure 5.7 Interdigital Capacitor EBG design and analysis (a) Unit cell design and dimensions, EL = 133.30 mm, EW = 3.50 mm, ES = 93.60 mm, ER = 14.8 mm, EH = 15.75 mm and EP = 43.3 mm, (b) Simulated reflection phase analysis, (c) Simulated reflection magnitude analysis. 61
Figure 5.8 Multilayered 1D EBG design phases, (a) Phase 1, one layered EBG, (b) Zoomed view phase 1 design, (c) Phase 2, two layered EBG, (d) Zoomed view phase 2 design, (e) Phase 3, three layered EBG, (f) Zoomed view phase 3 design, (g) Phase 4, three layered EBG with coupling rings, and (h) Zoomed view phase 4 design. 64
Figure 5.9 Proposed antenna CPWG balun feed design details, (a) Marchand balun schematic [39], (b) Labeled side view, (c) Dimensions view, CF = 181.15 mm, CL = 381.15 mm, CS = 175.27 mm, (d) Front view, (e) Feed balun zoomed left end section details, (f) Feed balun zoomed center section details and dimensions, CP = 0.75 mm, CG = 1.5 mm, CW = 5.5 mm, (g) Feed balun zoomed right end section details. . . . 65
Figure 5.10 Proposed antenna CPWG balun feed length CL analysis. 66
Figure 5.11 Proposed antenna large metallic surface placement and simulated results (a) Proposed antenna, (b) Antenna 3D gain plot without large ground plane at 0.335 GHz, (c) Placement on large metal surface with length and width of RL = 2.3 meters, (d) Surface currents at 0.335 GHz, (e) 2D radiation patterns with and without IDC EBG on large ground plane, and (f) 3D gain plot on large ground plane at 0.335 GHz. 67
Figure 5.12 Proposed antenna large curved surface placement and simulated results (a) Placement on large curved metal surface with length RL = 2.3 meters and width RM = 1.9 meters, (b) Placement side view with curve angle RA = 120 degrees, (c) 3D gain plot at 0.335 GHz, and (d) Surface currents at 0.335 GHz. 69

Figure 5.13 Proposed antenna large cylindrical surface placement and simulated results (a) Placement side view with diameter of RW = 0.73 meters and cylindrical center angle of RB = 90 degrees, (b) Placement front view with length RL = 2.3 meters, (c) Surface currents at 0.335 GHz, and (d) 3D gain plot at 0.335 GHz. 70

Figure 5.14 Proposed antenna aircraft placement and simulated results (a) Aircraft [40], (b) Aircraft 3D model fuselage length PL = 26.00 meters and wingspan PW = 28.37 meters (c) Proposed antenna placement under aircraft nose, fuselage diameter PR = 2.77 meters, front section diameter PN = 2.31 meters, (d) 2D radiation pattern with and without EBG, (e) 3D gain plot, (f) 2D gain plot details, (g) Surface currents, and (h) Surface currents zoomed view. 71

Figure 6.1 Proposed RadAlt and DME-TCAS-RadAlt antennas flight testing aircraft and placements (a) Antennas placement under aircraft fuselage, (b) Bottom view of antennas placement under aircraft fuselage. . . . 74

LIST OF SYMBOLS AND ABBREVIATIONS

DME	Distance Measuring Equipment
TCAS	Traffic Control and Avoidance System
RadAlt	Radio Altimeter
ADS-B	Automatic Dependent Surveillance - Broadcast
TIS-B	Traffic Information Services - Broadcast
SatCom	Satellite Communications
GPS	Global Positioning System
MOPS	Minimum Operational Performance Standards
ILS	Instrument Landing System
UAT	Universal Access Transceiver
EBG	Electromagnetic Bandgap

CHAPTER 1 INTRODUCTION

1.1 Motivation and Background

Antenna designing plays a critical role in the optimal performance of commercial and military aircraft communication, surveillance and navigation systems. Many antenna systems protruding and mounted outside the aircraft airframe creates drag by disrupting the airflow, that reduces the aircraft efficiency and increases the fuel consumption and cost. The numerous antennas with many ports and cable creates hazards of electromagnetic interference in the aircraft that can cause avionics equipment malfunctions and communication interruptions. The mounting of antenna system on the aircraft also distorts the radiation pattern of the antenna, due to large airframe of the aircraft with many segments, edges and corners. The software defined avionics radios brings new capabilities by integrating and dynamically controlling the aircraft radios, resources and hardware [41].

The motivation of this thesis is to design single and low profile antenna system for multiple aircraft wireless communication applications so that proposed antenna system can be integrated with the aircraft's software defined avionics radio. Single antenna for multiple avionics radios will improve the aircraft efficiency by improving the drag and will decrease the EMI hazards. The challenge is to propose technique for designing low-profile antenna that retains the radiation characteristics of the original antenna once they are mounted on the large metallic aircraft airframe.

The placement of antennas on aircraft airframe site is optimized for mitigating interference and meeting the aerodynamics requirements of the aircraft. Designing and selection of the type of antennas depends on the specific applications such as Radar Altimeter (RadAlt) and weather Radar that are standalone systems, and Instrument Landing System (ILS) that requires communications with the ground stations. The antenna placement on the aircraft airframe site depends on the communications of the system such as Global Positioning System (GPS) and Satellite Communications System (SatCom). The antennas of these systems are placed at the top of the aircraft fuselage as they communicate with the satellites. The Distance Measuring Equipment (DME) antenna is placed at the lower end of the aircraft fuselage and the Traffic Control and Avoidance System (TCAS) antennas are placed on both lower and upper aircraft fuselage. RadAlt antennas are also placed at the lower fuselage of the aircraft as the Radar Altimeter system is used for measuring the distance beneath the aircraft and above the terrain [9]. The detailed layout of various antenna placements on the aircraft is shown in Figure 1.1.

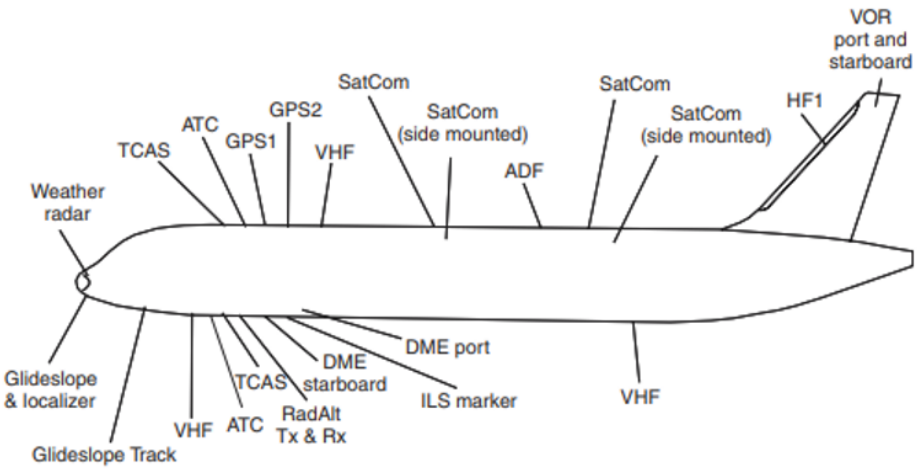

Figure 1.1 Details of the antenna placement in aircraft. Adapted from [9], p. 100.

1.2 Thesis Objectives

The general thesis objectives are as follows:

- Design and development of low profile antenna system that can be mounted on the aircraft with smooth radiation pattern without distortion that is suitable for the avionics systems;
- Design and development of single antenna system for multiple avionics systems that can be integrated with software defined avionic radio.

The specific objectives of the thesis are as follows:

- Design and development of a low profile radio altimeter antenna with gain of more than 10 dB, side lobe levels less than – 40 dB and high isolation level of more than 85 dB between the transmit and receive antennas in the whole the radio altimeter frequency band of operation from 4.2 GHz to 4.4 GHz;
- Design and development of hybrid single multiband antenna for the DME, TCAS, ADS-B and Radar Altimeter avionics systems placed on the lower side of the aircraft fuselage, according to the specifications provided in the Minimum Operational Performance Standards (MOPS), as detailed in Table 1.1;
- Design and develop a low profile Instrument landing system glideslope antenna for aircraft applications at the frequency band of 329 MHz to 335 MHz;

- Fabrication, frequency response and radiation pattern measurements, and flight-testing of the proposed developed antenna systems for the verifications of the operations of the DME, TCAS, ADS-B and Radar Altimeter avionics systems.

1.3 Methodology

A radio altimeter antenna is designed with patch antenna configuration for low profile configuration. The gain of more than 10 dB will be achieved with a 2 x 2 array and the bandwidth enhancement of the antenna will be done by stacking parasitic patch layer above the patch array. A low side lobe level of -40 dB will be achieved by designing electromagnetic bandgap structure for suppressing the currents around the patch array in the frequency band of operation from 4.2 GHz to 4.4 GHz. High isolation of more than 85 dB is achieved by reducing the sidelobe levels in the H-plane that corresponds to the forward direction for placement of the transmit and receive radio altimeter antennas under the fuselage of the aircraft.

A single multiband avionics antenna system for DME, TCAS, ADS-B and RadAlt communication systems is developed based on the location and placement requirements of the avionics system antennas on the fuselage of the aircraft. The omnidirectional radiation pattern characteristics are achieved by exciting a low profile cavity at the center with feeding probe and center fed patch. Frequency specifications for DME, TCAS and ADS-B systems required band from 960 MHz to 1215 MHz and enhancement in bandwidth is achieved by using circularly placed metallic vias passing vertical through the cavity. The additional resonance from this partial ring will be superimposed to the first resonance from the cavity by optimizing the location of the metallic vias, diameter of the cavity and diameter of the center feeding patch. Two feeding configurations will be designed with 2-port and 1-port respectively. The 2-port feeding design will provide separate feeding ports for both the lower placed cavity (L-band) and upper placed patch array (C-band), whereas 1-port feeding will be achieved by designing a three-dimensional power splitter for simultaneously feeding both the cavity and patch antenna array. An electromagnetic band gap structure will be designed for suppressing radio altimeter signals within cavity. Concept validation of the single hybrid multiband antenna system will be done by the analysis of the surface currents and radiation patterns of the antenna.

An instrument landing system low profile antenna will be designed by printed bowtie antenna placed over a ground plane. For suppressing the reflections from the closely placed metallic ground plane with the antenna, an electromagnetic band gap structure will be designed at the frequency band of 329 MHz to 335 MHz for providing required radiation characteristics for

Table 1.1 Avionics Systems Antenna Frequency Bands and Radiation Pattern Specifications [1–8].

No	Application	Frequency Band	Bandwidth/ VSWR	Gain	Radiation Pattern	Polarization
1	Distance Measuring Equipment (DME)	960 MHz - 1215 MHz	255 MHz/ 2:1	5 dB	Omni-directional	Vertical
2	Automatic Dependent Surveillance-Broadcast (ADS-B)	1090 MHz	±1 MHz/ 2:1	5 dB	Omni-directional	Vertical
3	Traffic Control and Avoidance System (TCAS)	1030 MHz - 1090 MHz	60 MHz/ 2:1	3-5 dB	Omni-directional	Vertical
4	Radar Altimeter (RadAlt)	4200 MHz - 4400 MHz	200 MHz/ 2:1	8-11 dB	Directional	Horizontal
5	Instrument Landing System (ILS) Glideslope	329 MHz - 335 MHz	6 MHz / 6:1	2 dB	Omni-directional	Horizontal

ILS glideslope avionics systems. Printed grounded coplanar waveguide balun will be designed for providing matching and feeding to the two arms of the bowtie antenna. Verification of the radiation patterns will be performed by placing and conforming the designed antenna with large metallic planes and aircraft models.

The designing of the TCAS, DME, ADS-B, RadAlt and ILS antenna systems will be done in CAD high frequency simulation softwares CST Microwave studio and Ansys-HFSS. The antennas will be 3D designed and analyzed for the frequency response, radiation patterns and current distributions. The antennas will be optimized for achieving the required specifications according to the avionics minimum operational performance standards. Optimally designed DME, TCAS, RadAlt, ADS-B antenna systems will be fabricated and lab tests will be performed on vector network analyzer and anechoic chamber for the verification of the frequency response and radiation patterns respectively. The proposed ILS antenna concept will be simulated for the verification of the frequency response and radiation characteristics. The ILS antenna placement on aircraft and radiation pattern simulations will be performed in CST Microwave studio frequency domain solver.

1.4 Thesis Outline

Chapter 2 presents the background and literature review of aircraft antennas. The aircraft siting design process is presented and summarized that is an essential step of placing the

antennas on the aircraft to avoid EMI hazards and operational effectiveness of the avionics systems. The aircraft antenna types are discussed that comprises of wired as well as aperture antennas that are suitable for aircraft systems. The RadAlt, DME, TCAS and ILS antennas are discussed in more detail as this thesis presents design concepts for these systems. Electromagnetic bandgap (EBG) concept and benefits in antenna designing are presented. EBG finds its applications in low profile aircraft applications.

Chapter 3 presents design of low profile Radio Altimeter antenna with enhanced bandwidth and high isolation levels. The antenna is designed in patch array configuration with stacked parasitic patches for bandwidth enhancement. One-dimensional circular EBG concept is presented that is used for reducing the sidelobe levels of the antenna by suppressing the surface currents in H-plane and therefore improving the isolation between the transmitting and receiving RadAlt antennas.

Chapter 4 presents design of a multiband antenna for DME, TCAS, ADS-B and RadAlt systems and is suitable for integrating with software-defined avionics radios (SDAR) that manages the avionics radio in one hardware platform. Two antenna concepts with 2-port and 1-port feeding is designed and presented. The 2-port antenna is designed with two separate feeding mechanisms, where one feed port is for lower cavity that produces omnidirectional radiations for DME, TCAS and ADS-B applications, and the other feed port is for upper RadAlt patch array that produces directional radiations. The second antenna presents a single feeding design for the objective of integration with SDAR. A power splitter is presented for simultaneously feeding the lower cavity as well as upper patch array. Electromagnetic bandgap is designed and placed within the cavity for suppressing RadAlt signals within the cavity. The antennas are fabricated and the frequency response and radiation patterns are presented for the validation of the concept.

Chapter 5 presents design of low profile Instrument Landing System (ILS) glideslope antenna that is designed for placing on the aircraft airframe. The design of low profile printed conical bowtie antenna design is presented that is placed on top of EBG that provides and in-phase current due to the high impedance surface and reinforces the radiation pattern of the antenna closely placed on the metal ground plane. The electromagnetic bandgap is designed using interdigital capacitor structure for compact size. Printed grounded coplanar waveguide balun design is presented for feeding the two arms of the conical bowtie antenna. The low profile antenna concept is demonstrated by placing the proposed antenna on large metal surfaces and aircrafts, and the frequency response, radiation patterns and surface currents are presented.

Chapter 6 presents summary of the designed low profile and multiband avionics EBG antennas for the DME, TCAS, ADS-B, RadAlt and ILS applications. Future recommendations

and next research design steps are also presented in this chapter. The result analysis for the flight testing of DME, TCAS, ADS-B and RadAlt antennas will be performed. In the next step, the proposed single antenna will be integrated with the software defined avionics radio. ILS glideslope antenna will be fabricated for verification of radiation characteristics on flat and curved surfaces. Radomes will be designed for the proposed antennas.

CHAPTER 2 LITERATURE REVIEW

2.1 Background

The designing of the aircraft antennas is verified and analyzed for ensuring the avionics systems optimal communications performance as well as satisfying the aircraft aerodynamics requirements. Minimum Operational Performance Standards (MOPS) for the airborne communication systems are studied and implemented in the designing of the aircraft antennas for the achieving the optimal performance requirements for each communication system functioning in the aircraft during the flight operations [1–8]. Aircraft antenna requirements are studied for designing with respect to the specific requirements of each avionics communication system such as Distance Measurement Equipment (DME) operated in the frequency range of 960-1215 MHz, Traffic Control and Avoidance System (TCAS) with omni-directional radiation pattern requirements, Automatic Dependent Surveillance-Broadcast (ADS-B) and Traffic Information Services-Broadcast (TIS-B) systems with Universal Access Transceiver (UAT) requiring vertical polarization. Instrument Landing System (ILS) with specific requirements of ground station communications requires omni-directional radiation patterns with horizontal polarizations. The details of the avionic system specifications are given in Table 1.1.

2.2 Aircraft Antennas Siting Design

Antennas siting and layout design on the aircraft has paramount importance for the simultaneous operations of communication systems. The antennas siting is iteratively designed as the antenna radiation characteristics not only depends on its type but also varies with the location of the placement on the aircraft airframe for small, medium and large aircrafts [9]. Summary of the aircraft antenna siting design process is shown in Figure 2.1.

In the initial design stage of the antenna siting, the antenna and system level specifications and requirements are collated. The polarization and frequency of the antennas will determine the location and orientation of the antenna placement as the antenna separation and isolation is dependent on the electrical distance between the radiating elements. The vertical and horizontally polarized antennas can be placed in close proximity such as the VHF antennas and the ILS Glideslope antennas as there will be no coupling between these differently polarized antennas. The system level specifications includes the power of the transmitters and sensitivity of the receivers that depends on the range of the communications. The initial

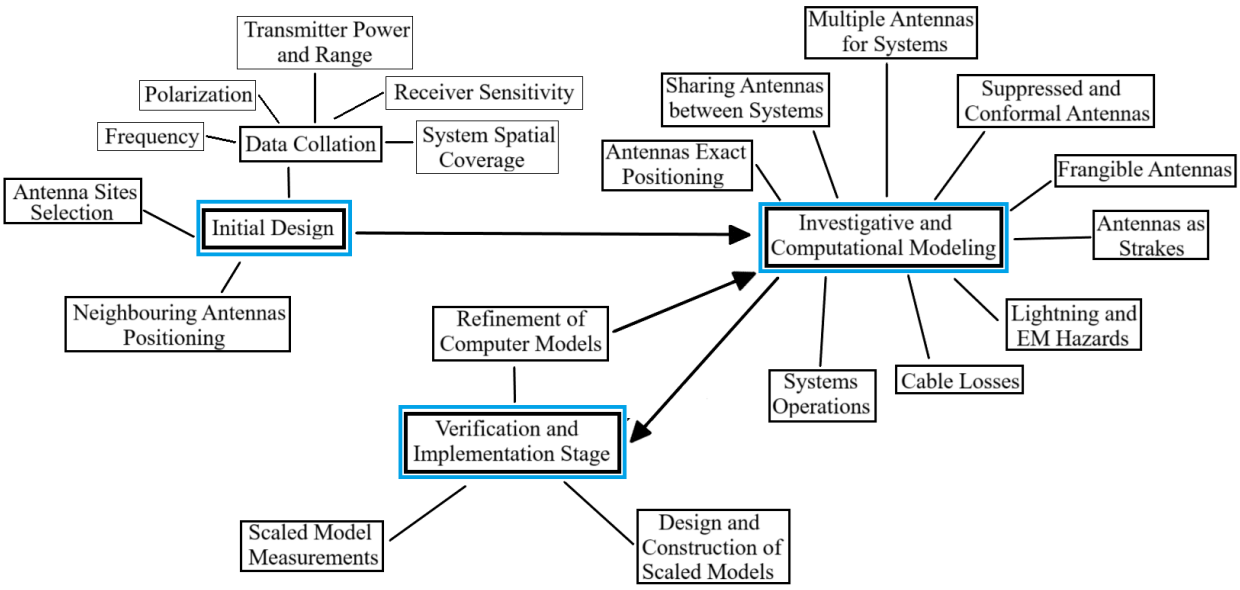

Figure 2.1 Summary of the antenna siting design on the aircraft.

placement of the antennas on the airframe of the aircraft is done based on the profile of the airframe and avoiding any obstruction of the line of sight from the different radiating elements and segments of the airframe for ensuring the desired spatial coverage of the communication systems.

The exact location of the antennas on the airframe is determined in the second stage of the siting design by computational modeling of the airframe with the radiating elements. Various antenna systems can be placed at the aircraft and the radiation pattern analysis can be achieved by the synthesis of characteristic model computations for the multiband radiations of these mounted antenna systems [42]. For the optimal placement of the antennas and performance of the systems, it is determined if an antenna from one system can be used and shared with other systems or if multiple antennas are required by a single system such as TCAS, where one antenna is placed at the upper fuselage and the antenna is placed at the lower fuselage.

Antenna placement on the aircraft can be modeled and the effects of the various aircraft sections such as aircraft wings can be incorporated in the computations of the antenna systems for the verification of the MOPS requirements of the frequency response return loss and far-field radiation patterns of the installed antennas [43]. The antennas can be conformed along the profile of the airframe so that they do not protrude, like the RadAlt antennas. Currently most aircrafts use the patch antennas that are more low profile antennas

and are suitable for the RadAlt systems [9].

The computational modeling and placement of the antennas are also optimized by incorporating the lightning hazard zones on the aircraft. In these zones, the placement of the antennas are avoided and the hazard zones are covered with lightning strips. These strips provide an ionized channel so that the lightning can travel through it and avoid any harm to the aircraft passengers and important instruments [44]. The placement positions of the strakes and frangible antennas are determined in the computational modeling, where the strakes are used for stabilization of the aircraft and are placed behind the protrusions to reduce the turbulence effects and the frangible antennas are placed at the lower fuselage for protecting the airframe in case of emergency landing. In the third stage of the siting design, the scaled model is designed and constructed for the measurements of the radiation characteristics and isolation of the antennas and the computer based model is iteratively optimized for the placement of the antennas on the airframe.

2.3 Aircraft Antenna Types

Aircraft communication systems use different types of antennas depending on the frequency, range and spatial coverage requirements of various applications. Types of antennas used on the aircraft systems are shown in Figure 2.2 [9]. The radiation characteristics of the antennas vary with and without metallic ground plane and the radiation patterns can distort when placed on the large airframe of the aircrafts. Dipole antennas are designed with two wires as shown in Figure 2.2(a), and are used in Telemetry and VHF Omnidirectional Ranging (VOR) systems. Different sized dipoles can be designed for various gain and beamwidth requirements. Circularly polarized dipole antennas can be designed by using two dipoles in cross configuration and feeding one of the dipole with 90 degrees phase difference [9].

Notch antennas are designed by removing a slot and replacing by dielectric material in the metal sheet as shown in Figure 2.2(b). The blade antennas can be designed from slot that is radiating like a monopole or from a tuned monopole that is enclosed in a blade shape as shown in Figure 2.2(c). Such antennas are used in DME and placed on the lower front fuselage and these blade antennas are also used in the Telemetry, Secondary Surveillance Radar (SSR) and In-flight telephony aircraft applications [9]. Reflector antennas are designed by feeding a reflector from a horn placed at the focus of the reflector and in Cassegrain system two reflectors are used as shown in Figure 2.2(d) and are used in weather radars and Satellite Communication (SatCom) systems. These antennas for weather radars operate in the C and X frequency band of and mounted in the nose of the large aircraft. The antennas for SatCom operate UHF and SHF frequency bands and are placed on top of the aircraft fuselage.

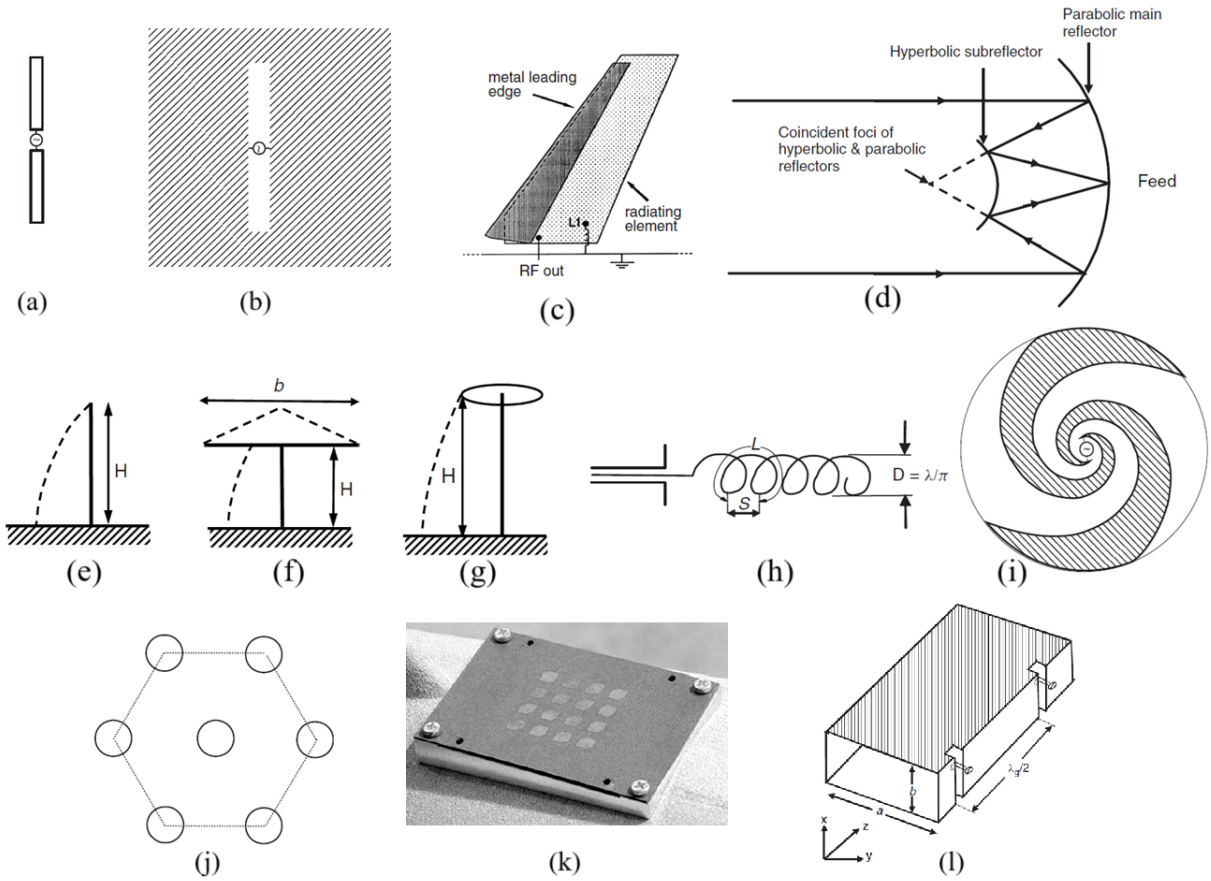

Figure 2.2 Aircraft antenna types [9], (a) Dipole antenna, (b) Slot antenna, (c) Blade antenna, (d) Reflector antenna, (e) Monopole antenna, (f) Loaded monopole antenna T-shaped, (g) Disc loaded monopole antenna, (h) Helical antenna, (i) Spiral antenna, (j) Array antenna, (k) Patch antenna, and (l) Slotted waveguide array antenna.

Many aircraft systems use the monopole antenna such as DME, Distress systems, UHF, VHF, Radio Broadcast FM and ILS localizer systems. Monopole antennas consist of single wire radiating element and is place on the ground plane as shown in Figure 2.2(e). Loaded monopole are designed for increasing the electrical length of the antenna by using top placed T section or a circular disc as shown in Figure 2.2(f) and Figure 2.2(g). The advantage of top loaded antennas is their lower height compared to the straight dipole for a given frequency and also increases the antenna gain. Monopole and dipole embedded single antenna design can switch between the omnidirectional and directional radiation patterns by using reconfigurable switching PIN diodes placed at feeding lines for the two embedded antennas. This makes it possible to cover the upper hemisphere that is suitable for aircraft applications [45].

Dual polarized aircraft antenna system can be realized by monopole antenna fed by slot

coupling that will produce vertical polarization [46]. In this antenna, the embedded thin top mounted metallic strip cavity along with the monopole antenna produces horizontal polarization. The feeding mechanism of this dual polarized antenna system comprises capacitively coupled slot that is fed by the microstrip line [46].

Glass embedded aircraft antennas can be realized by using two radiating elements printed on the glass window of cockpit, where the radiating elements can be excited by couple feeding from feeding lines. These antennas are designed for the FM frequency band radio aircraft applications [47]. SatCom systems use circularly polarized helical antennas that are designed by turning wire in helical form with certain diameter and spacing as shown in Figure 2.2(h). Electronic Support Measure (ESM) systems use planar spiral antennas that have broadband frequency range and comprises two arms of spirals as shown in the Figure 2.2(i), producing radiations along the axis perpendicular to the radiating elements.

Aircraft uses patch antenna array elements as shown in Figure 2.2(j), for narrowing the beam and for steering the beam controlled by GPS, for canceling unwanted signals [9]. Patch antenna are low profile antennas and are designed on the printed circuit boards as shown in Figure 2.2(k), that have high gain and directional radiation patterns and are used in the modern GPS and radio altimeter aircraft systems. Patch aircraft antenna system can be designed for multiple frequency bands by switching between different smaller radiating segments within the whole patch antenna system [48]. Weather radars use slotted waveguide antennas as shown in the Figure 2.2(l), that are designed by introducing the slots in the waveguide and are used for high power requirements.

2.4 Radio Altimeter Antennas

Radar Altimeter (RadAlt) standalone system is used for measurement of the distance beneath the aircraft and above the terrain. It requires high-gain antenna arrays with directional radiation patterns pointing to the ground and operated in the frequency band of 4200-4400 MHz. Substrate-integrated waveguide based antenna system can be designed with cavity embedded inside a cavity concept and various slots with varied lengths can be coupled to produce three resonances for the applications of Radio altimeter, ISM and WLAN applications where the inner cavity can be fed by direct probe as shown in Figure 2.3(a) [10]. Radio altimeter antenna is designed for isolation levels of 50 dB with a separation between the transmitting and receiving antennas of 500 mm, as illustrated in Figure 2.2(c).

Radio altimeter antennas mounted on the bottom of the aircraft fuselage are shown in Figure 2.2(e). A commercial radio altimeter antenna covered with radome along with the vswr

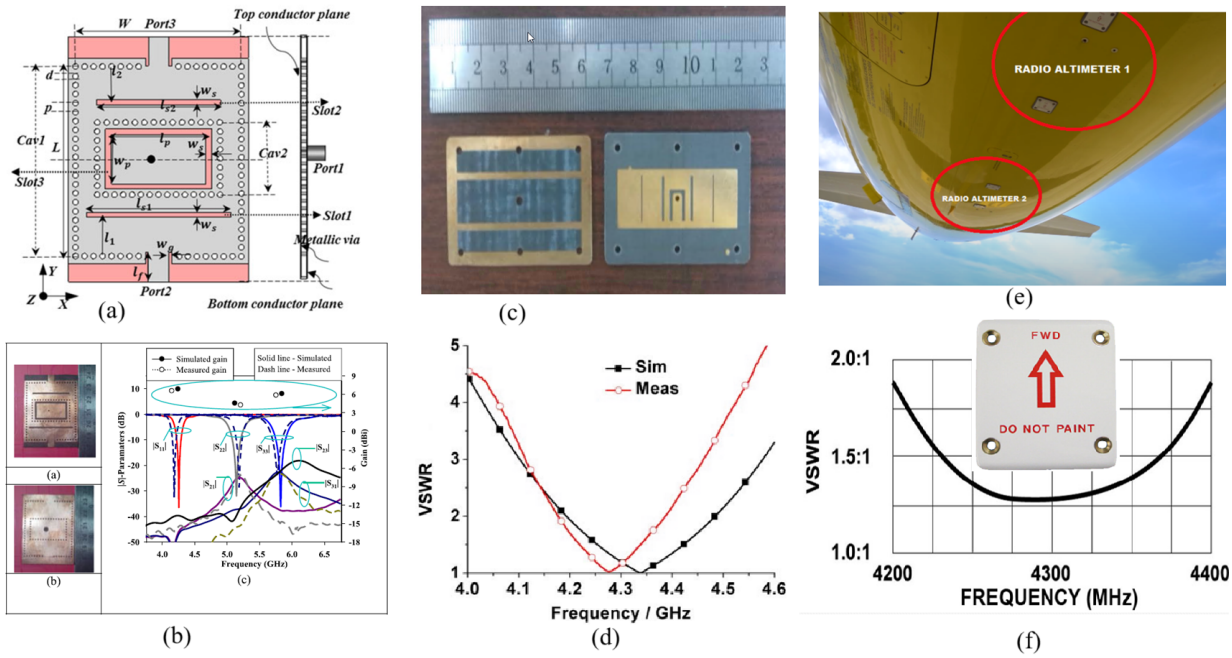

Figure 2.3 Radio altimeter antennas, (a) Triplexer antenna for RadAlt, WLAN and ISM bands [10], (b) Triplexer antenna frequency response [10], (c) Two layered Radio Altimeter antenna [11], (d) Frequency response [11], (e) RadAlt antenna mounted under aircraft [12], and (f) Commercial RadAlt antenna and frequency response [13]

graph is shown in Figure 2.2(f). Radio Altimeter radar uses narrow beam directional antenna systems for measurement of the surface heights and sea winds for the computations of safe height for the aircraft such as while landing on the sea and rescue and search operations [49]. These radars comprise nadir direction high gain antennas for the measurements of surface, wind direction and speed of the sea waves. Radar Altimeter antenna system can be designed by using patch antenna radiation elements in an array configuration for achieving gain requirements of at least 9 dB, and each patch antenna element can be fed by inset feeding of the microstrip lines from the feeding network [50]. The bandwidth enhancement of the antenna system for ensuring the MOPS can be realized by using stacked patch elements with different patch antenna dimensions [51].

2.5 Distance Measuring Equipment Antennas

Distance Measuring Equipment antennas are mounted on the lower fuselage of the aircrafts and monopole antennas, often referred to as blade antennas, are used with vertical polarization. The DME system continuously communicates with the ground station and measures the direct distance of the aircraft from the ground station that is called the slant range of

the aircraft. Unlike blade antennas, low-profile antennas are designed by using a top circular patch in which L-shaped probe is used for feeding the patch at the center as shown in Figure 2.4(a) [14]. The circular patch antenna configuration is designed with shorting pins for bandwidth enhancement and is internally fed by a probe for low profile omnidirectional radiation characteristics, as shown in Figure 2.4(c) [15]. Similar antenna configurations can be designed by directly feeding the top circular loaded patch with the internal pin of the

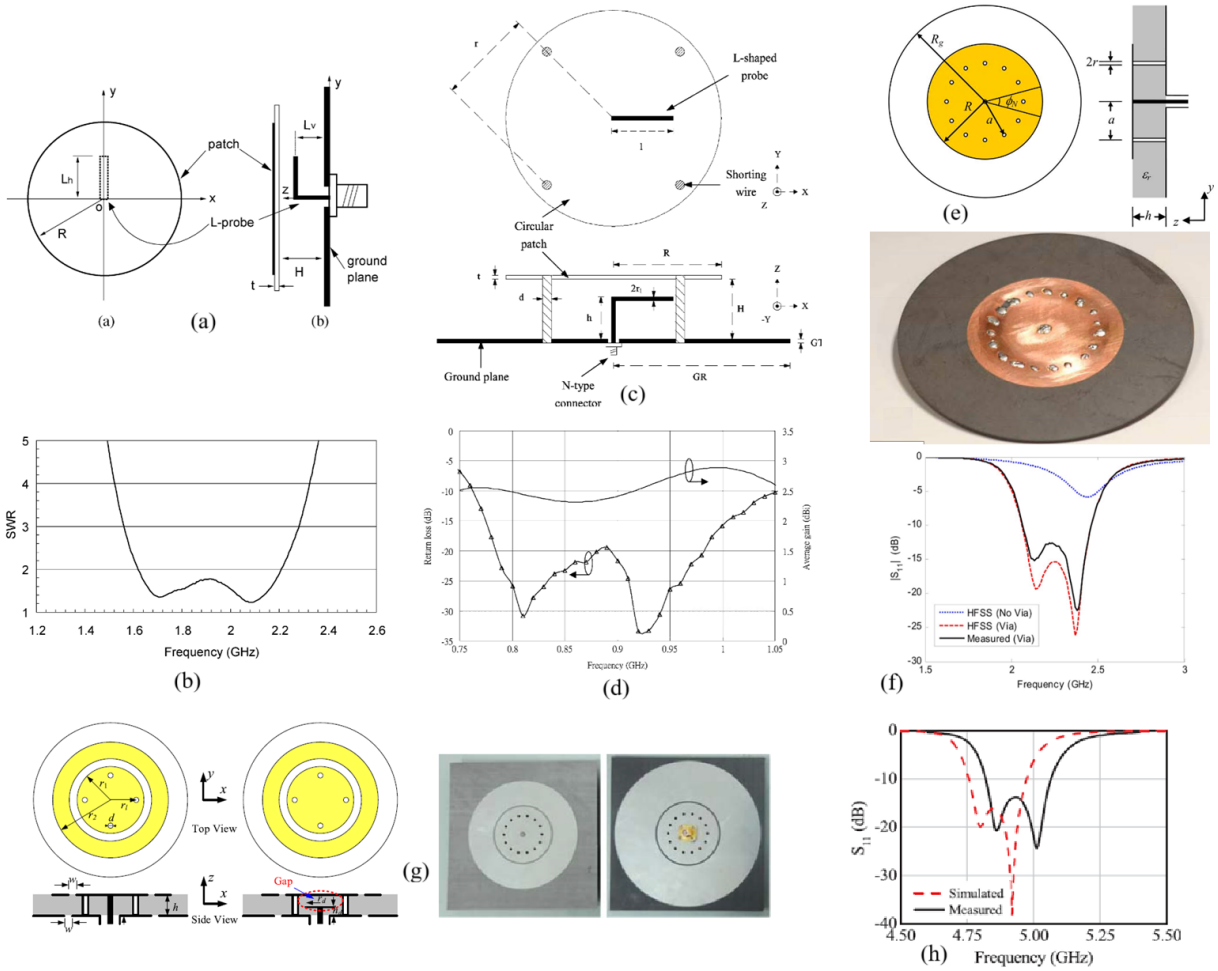

Figure 2.4 Low profile omnidirectional antennas, (a) Wideband L probe fed patch antenna [14], (b) L probe patch antenna frequency response [14], (c) Monopole wire patch antenna [15], (d) Monopole wire patch antenna frequency response [15], (e) Low profile monopole patch antenna [16], (f) Monopole patch antenna frequency response [16], (g) Loop array monopole antenna [17], and (h) Loop array monopole antenna frequency response [17].

feeding connector instead of separate probe for omnidirectional radiation pattern and shorting the top circular patch for bandwidth enhancement, as shown in Figure 2.4(e) [16].

The gain of the omnidirectional low-profile antennas can be enhanced by cutting a circular slot in the top circular patch, as shown in Figure 2.4(g). The slot forms an effective magnetic-loop antenna that is fed internally in its cavity by a coupling disc. The combined radiation of the patch edge and the circular slot provides vertical polarization with omni-directional radiation patterns that are stable in the frequency band of operations as shown in Figure 2.4(g) [17].

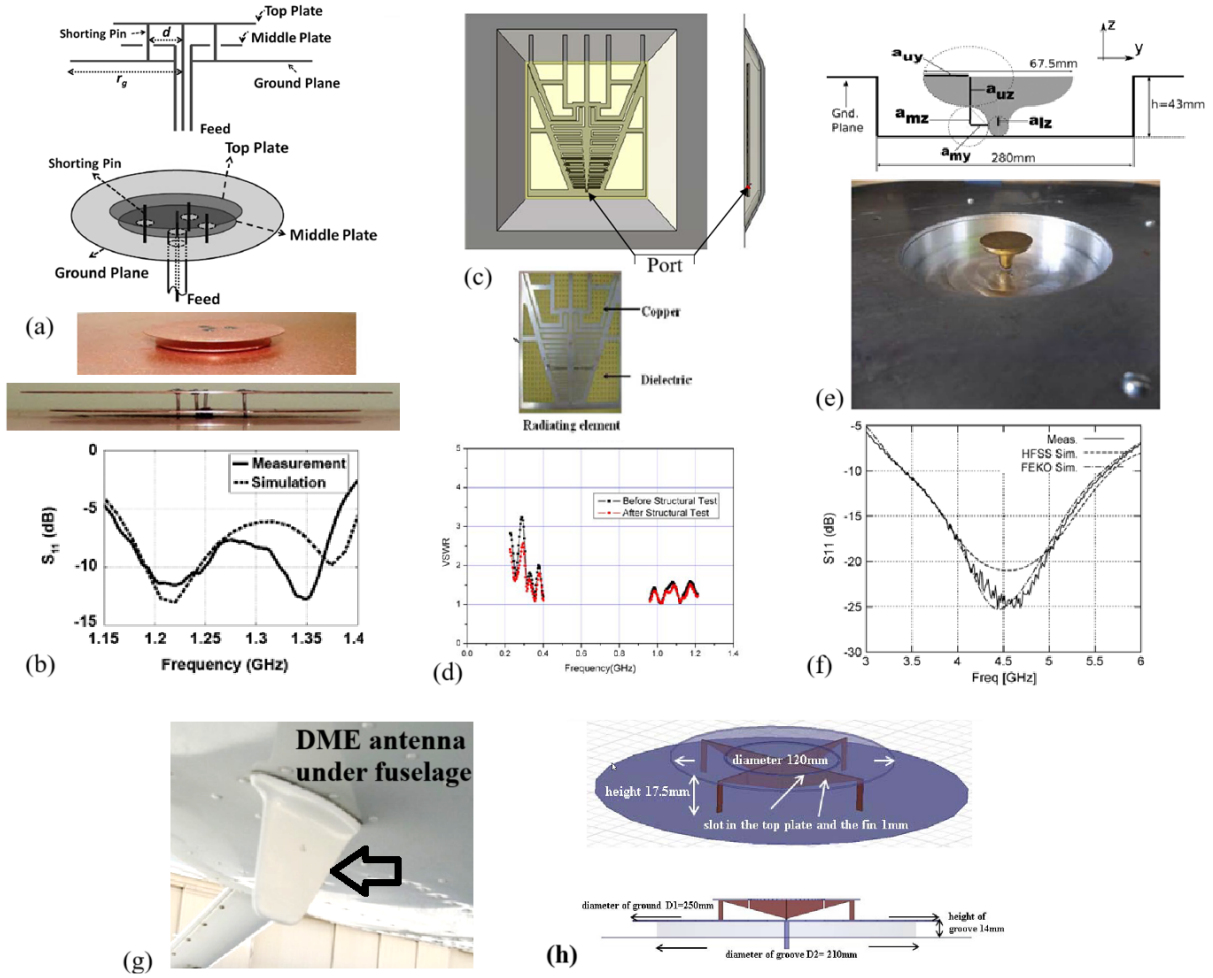

Figure 2.5 Distance measuring equipment antennas, (a) Low profile wideband monopole antenna [18], (b) Low profile wideband antenna frequency response [18], (c) Printed DME antenna [19], (d) Printed DME antenna frequency response [19], (e) Cavity backed nonprotruding antenna [20], (f) Cavity backed antenna frequency response [20], (g) DME antenna mounted under aircraft [21], and (h) Low profile DME antenna [22].

A low-profile DME antenna can be designed with two layered plate concept [18]. One top plate with shorting pins is used for loading the monopole antenna and the middle metallic plate is used for feeding the inner cavity of the antenna as shown in Figure 2.5(a). Printed

antenna with various slots can be used for designing multiband aircraft antenna for the communications in the lower frequency range for UHF and upper frequency range for DME L-Band applications [19]. The conformal characteristics for this antenna can be realized by using various layers of mesh sheets aligned with layers of dielectric material as shown in Figure 2.5(c). Metallic hat profiled in a metallic ground plane cavity is used to achieve wideband DME antenna characteristics with vertical polarization and omni-directional radiation pattern [20]. In this antenna, three segments of elliptical shape can be optimized for achieving DME frequency band requirements as shown in Figure 2.5(e). The prototype is designed with a scaling factor of 0.25 and the frequency response is operating in the higher frequency band centered at 4.25 GHz, instead of the DME frequency band as shown in the Figure 2.5(e). A commercial DME blade antenna mounted on the lower fuselage of the aircraft is shown in Figure 2.5(g), and it can have a height of 83.312 mm (3.28 in) [52].

Design of the broadband DME antenna system is done by using the top loaded low-profile monopole antenna configuration in [53]. Vertical shorting pins are used for increasing the band of operation and omni-directional radiation pattern is realized with vertical polarization by using the monopole configuration. Increased directivity is realized by introducing a groove cutting at the lower end metallic ground planes for the magnetic loop antenna configuration that is suitable for low drag omni-directional aircraft antenna for DME applications [22]. Magneto-dielectric materials can be used to reduce the height of the vertically placed monopole configured radiating antennas for aircraft application by using pair of magneto-dielectric circular disc shaped materials at the top and bottom end of the vertical monopole that is suitable for the Distance Measurement Equipment (DME) aircraft applications [54].

2.6 Traffic Collision Avoidance System Antennas

The traffic collision and avoidance system (TCAS) is used for detecting nearby aircrafts for avoiding any collisions. It measures the speed and range of the nearby aircrafts for tracking them and displaying close by aircrafts that can be a threat of collision. The TCAS antennas are mounted on the upper as well as lower fuselage of the aircraft. The upper TCAS antenna is directional antenna whereas the lower TCAS antenna is omnidirectional antenna. Directional endfire TCAS antenna is designed with four element array and top loading is done in each element to reduce the height, as shown in Figure 2.6(a). Eight 45-degree beam steering directions are achieved by exciting some of the antenna elements while leaving the othe elements passive and acting as reflectors, using a switching network. The antenna covers 360 degrees as shown in Figure 2.6(b) [23]. A low profile TCAS antenna is designed for both

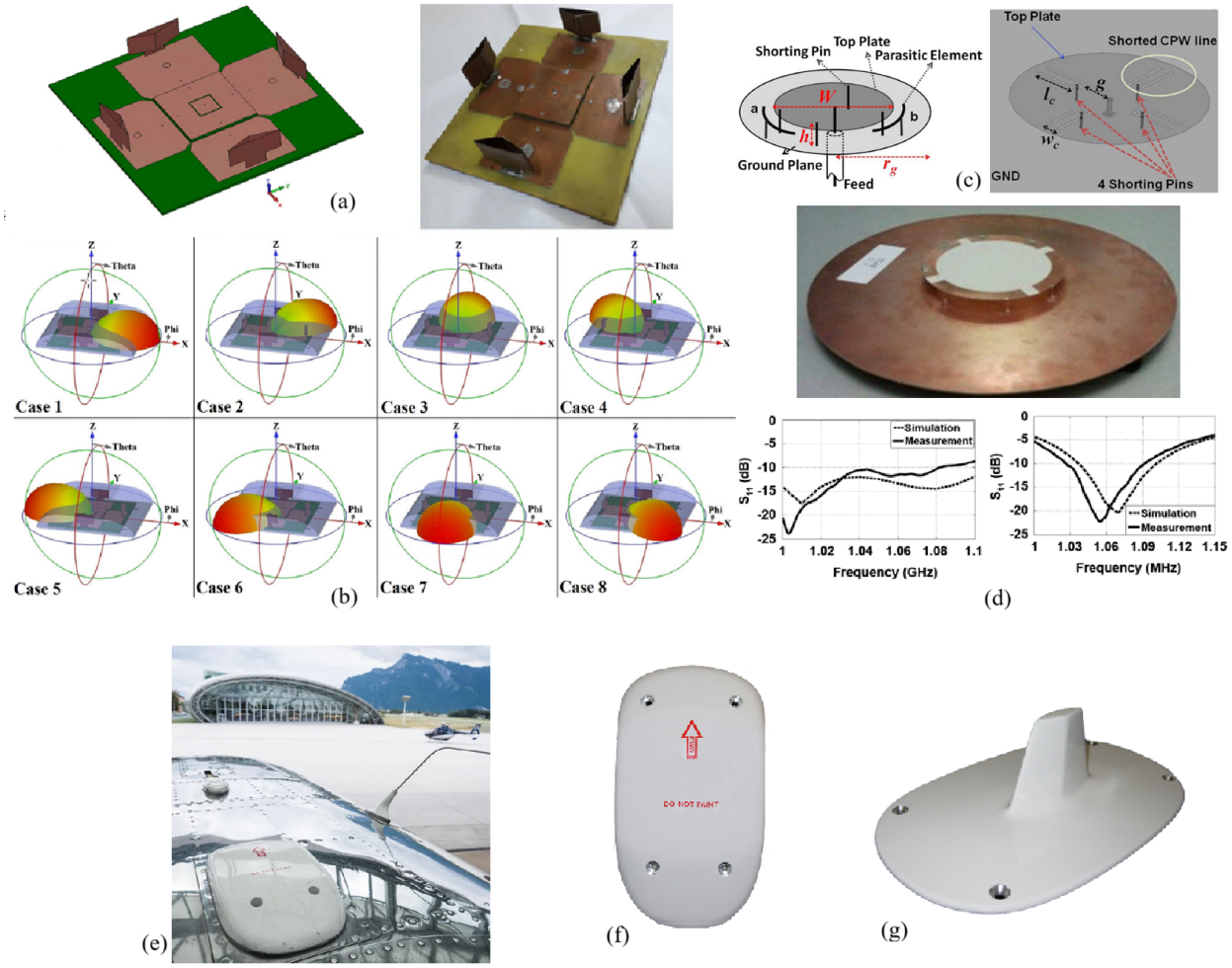

Figure 2.6 Traffic Collision and Avoidance System antennas, (a) Multiport directional TCAS antenna [23], (b) Multiport antenna radiation patterns in various directions [23], (c) TCAS antenna with beam switching design [24], (d) Beam switching TCAS antenna frequency response [24], (e) TCAS antenna mounted on aircraft [25], (f) TCAS commercial low profile antenna [26], and (g) TCAS commercial blade antenna [27].

the directional as well as omnidirectional radiations by using top loaded monopole configuration and four parasitic elements as shown in Figure 2.6(c) [24]. The four parasitic elements can be activated individually for steering the beam in a given direction and the frequency response of the antenna covers the band from 1.03 GHz to 1.09 GHz as shown in the frequency responses of the directional and omnidirectional modes in Figure 2.6(d). TCAS antenna mounted on the upper fuselage is shown in Figure 2.6(e), and the commercial directional and omnidirectional TCAS antennas are shown in Figure 2.6(f) and Figure 2.6(g) respectively.

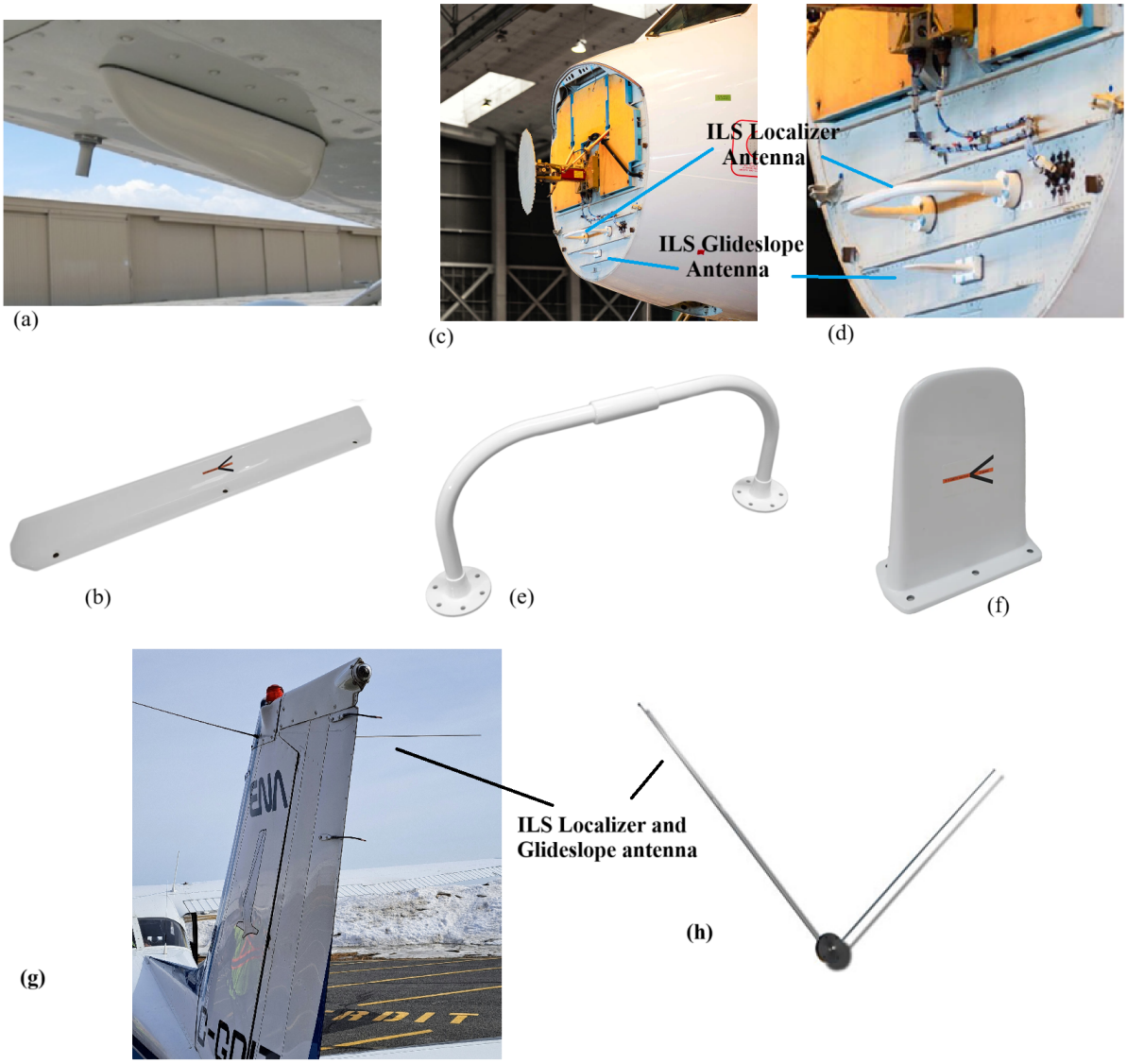

Figure 2.7 Instrument Landing System antennas, (a) ILS Marker beacon antenna mounted at the lower fuselage of aircraft [21], (b) Commercial Marker antenna [28], (c) ILS Glideslope and Localizer antennas installed at the nose of large aircraft [29], (d) ILS Glideslope and Localizer antennas zoomed image [29], (e) Commercial ILS localizer antenna [30], (f) Commercial ILS Glideslope antenna [31], (g) ILS Localizer and Glideslope antenna on tail of smaller aircraft, and (h) Commercial ILS localizer and glideslope antenna [32].

The omnidirectional TCAS antennas are designed using blade antennas and can have a height of 62.23 mm (2.45 in) [27].

2.7 Instrument Landing System Antennas

Instrument Landing Systems (ILS) guides the aircraft in the landing and comprises three systems of Localizer, Marker and Glideslope. The ILS marker system informs the aircraft of its distance from the runaway and the marker antenna is placed at the lower fuselage of the aircraft along the line of flight. The placement of the marker antenna on the aircraft is shown in Figure 2.7(a) and is designed with electrically small antenna with capacitive loading. The commercial marker antenna is shown in Figure 2.7(b) and the antenna operates on the ILS marker frequency band of 74.75 MHz to 75.25 MHz with horizontal polarization. The ILS glideslope system guides the aircraft vertically and ILS localizer systems guides the aircraft laterally for landing along the glidepath. The ILS glideslope and localizer antennas are mounted on the nose of the aircraft as shown in the Figures 2.7(c) and (d). The ILS localizer antenna is designed for the frequency band of 108 MHz to 112 MHz and a commercial antenna is shown in Figure 2.7(e). Both the ILS glideslope and localizer antennas are horizontally polarized antennas, and the ILS glideslope antenna is designed for frequency band of 329 MHz to 335 MHz and a commercial antenna is shown in Figure 2.7(f). The ILS localizer and glideslope 'V' antenna is mounted on the tail of smaller aircrafts as shown in Figure 2.7(g) and Figure 2.7(h).

2.8 Electromagnetic Bandgap Structures for Antenna Applications

All the novel antenna concepts presented in Chapter 3, 4 and 5 of this thesis make use of electromagnetic bandgap (EBG) structures to make the antenna more compact. In this section we describe a few of the most well-known EBG designs used as artificial magnetic conductors.

High impedance surfaces are designed with protruding mushroom surfaces as shown in Figure 2.8(a), that reduce the current flow along the surface for a specific frequency range and acts as magnetic conductors [33]. The images of horizontal currents are in phase with the original currents for magnetic conductors and provides many advantages in antenna designing and placing the radiating elements near the ground plane. Compact high impedance surface can be designed by using pads and connecting lines in the unit cell structure of the EBG as shown in Figure 2.8(b) [34]. The EBG structure can be designed more compact by using interdigital segments as shown in Figure 2.8(c) [35]. The EBG layer can be used for mutual coupling reduction between antenna elements by placing layer of EBG as superstrate on top of the antenna elements as shown in Figure 2.8(d) [36]. Multiband EBG can be designed by embedding slots within the EBG patch as shown in Figure 2.8(e) [37].

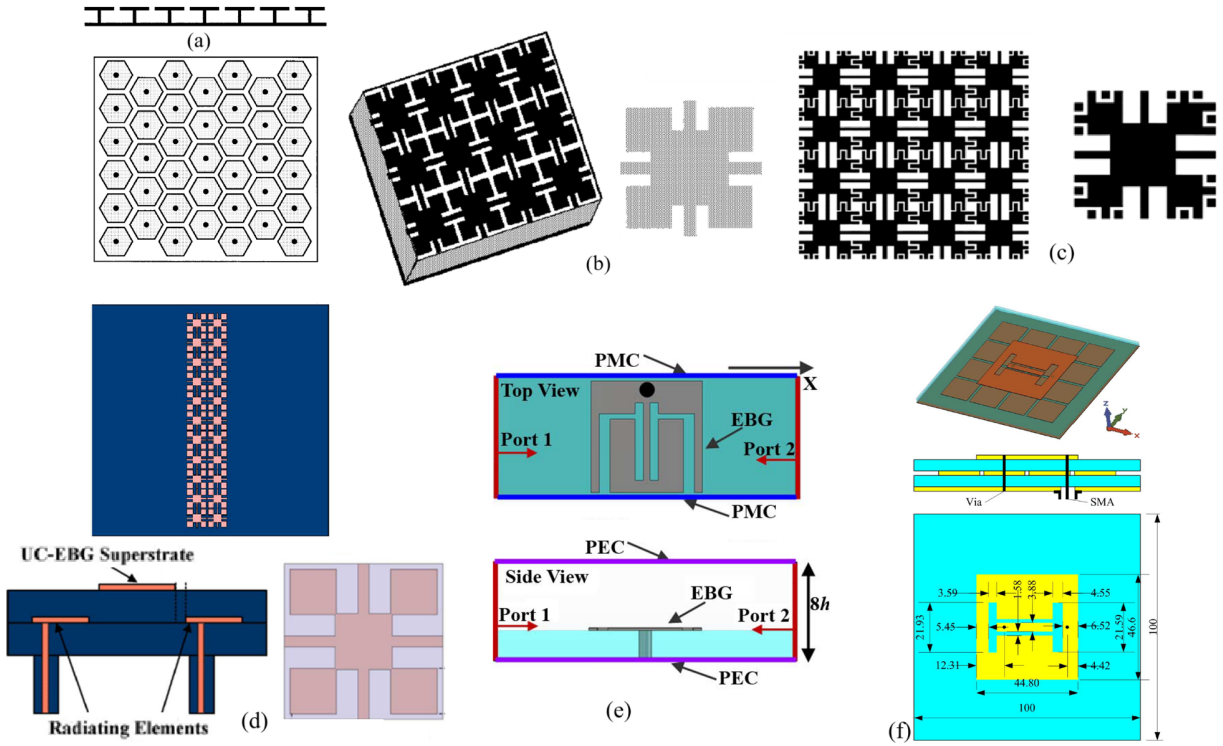

Figure 2.8 Electromagnetic bandgap structures, (a) Side and top views of the top patches connected with ground plane with metallic vertical vias [33], (b) Uniplanar compact bandgap periodic metal sheet and unit cell structure [34], (c) Interdigital periodic metallic layer and unit cell structure, [35], (d) EBG superstrate layer on antenna elements, [36], (e) Slotted EBG, [37], and (f) EBG layer below slotted dipole. [38].

Artificial magnetic conductors (AMC) forming high impedance surfaces can be used for designing low-profile dual band antennas by using printed slotted radiating patch and placing AMC layer in between the patch and ground plane, as shown in Figure 2.8(f) [38]. Various tiled structures with conformal characteristics can be integrated with spiral and thin radiating antenna elements along with the layers of absorbing materials and high impedance surfaces for the limitation of the radiation in specific frequency bands are developed for light weight antenna systems that can be integrated with various aircraft applications [55].

The vertical monopole placed on the finite ground plane radiates in free space as shown in Figure 2.9(a) and the surface waves produced in the ground plane also radiates from the corners and edges that cause interference with the antenna radiations as shown in Figure 2.9(c). The high impedance surface placed at the metal ground plane as shown in Figure 2.9(b), blocks the current flow and surface wave propagation along the metallic ground plane in a specific frequency band and radiation pattern of the wire antenna becomes smooth as shown

in Figure 2.9(d).

Similar applications of surface wave mitigation by using high impedance surfaces can be applied on patch antennas placed on ground plane as shown Figure 2.9(e) and (f). The smooth directional radiation pattern of the patch antenna with the use of high impedance surface is shown in Figure 2.9(g). Another application of the high impedance surface is in the horizontally placed wire antenna close to the metal ground plane as shown in Figure 2.9(h) and (i). The high impedance surface enables the in-phase current and the radiation pattern of the closely placed wire antenna can be reinforced as shown in Figure 2.9(j).

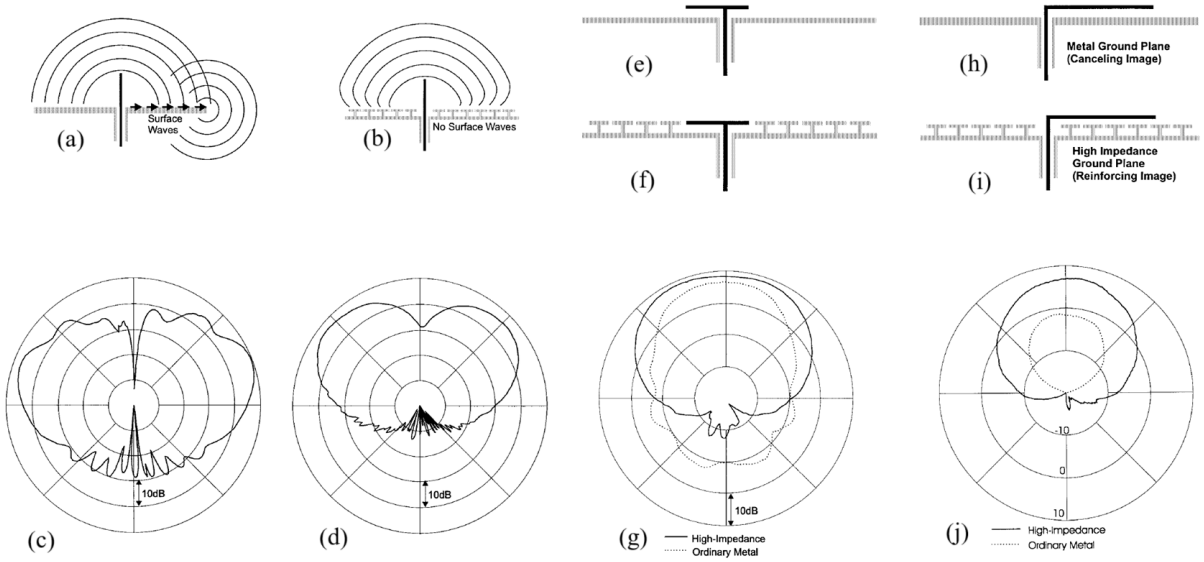

Figure 2.9 Electromagnetic bandgap antenna applications [33], (a) Vertical monopole antenna on ground plane generating surface waves, (b) Suppressed surface waves using EBG, (c) Radiation pattern vertical monopole antenna on ground plane with nulls and lobes, (d) Smoothed radiation pattern vertical monopole using EBG, (e) Patch antenna on metal ground plane, (f) Patch antenna on EBG, (g) Patch antenna radiation pattern with and without EBG, (h) Horizontal antenna on ground plane, (i) Horizontal antenna on EBG, (j) Radiation pattern of horizontal antenna with and without EBG.

2.9 Conclusion

This chapter presents an overview and literature study of the avionics systems, standards and various types of antennas used in these systems. ILS, DME, TCAS and RadAlt are important aircraft systems that are used for the navigation, collision avoidance and landing of the aircraft. Most of the aircraft systems use wired antennas such as monopoles. These

antennas are protruding and mounted outside the aircraft airframe, and it increase drag, fuel consumption and cost. The radiation pattern of the antennas also distorts as they are mounted on the aircraft airframe.

In the next chapters we present low profile RadAlt, DME, ADS-B, TCAS and ILS antennas by using patch antennas, low profile monopole cavity and electromagnetic bandgap structures. We also present a solution for combining antennas for multiple avionics systems of DME, TCAS, ADS-B and RadAlt, that can be integrated with software defined avionic radio.

CHAPTER 3 ARTICLE 1: HIGH ISOLATION AND BAND ENHANCED RADIO ALTIMETER ANTENNA FOR AVIONICS APPLICATIONS

Omar Masood Khan and Jean-Jacques Laurin

Published in IEEE Open Journal of Antennas and Propagation,
doi:10.1109/OJAP.2024.3425225

Publication date: July 08, 2024

3.1 Abstract

Concept of ringed stacked patch antenna with low side lobe level and enhanced bandwidth is introduced for radio altimeter avionics applications. One dimensional electromagnetic band gap is designed using metallic vias with circular rings along the radiating patches on multilayered substrate for providing high isolation in H-plane and reducing lateral surface currents. A stacked patch antenna configuration is used for enhancing the bandwidth of the antenna. Simulation and analysis are performed for the optimization of the frequency response and sidelobe levels of the proposed antenna. Gain of more than 12 dB with sidelobe levels less than -42 dB were measured for a fabricated prototype. Signal to interference ratio of 85 dB is achieved between two adjacent antennas, which is 5dB better than commercial antennas due to increased gain and reduced sidelobe levels. The antenna is designed for enhanced frequency bandwidth from 4.06 GHz to 4.53 GHz. Computed drag coefficient of the antenna mounted on the fuselage of Cessna 210 aircraft show that the drag is essentially negligible.

3.2 Introduction

Radio altimeter systems require high isolation levels between the transmitting and receiving antennas that are mounted on aircrafts. The distance of placement between the radio altimeter antennas may pose challenges due to limited space available on the aircrafts. Various designs have been presented previously for reducing the mutual coupling between the adjacent antennas and increasing the isolation levels [56–61]. Array of four columns of electromagnetic band gap structures (EBG) can be placed in between the adjacent patch antennas for reduction in the mutual coupling, where the electromagnetic band gap structures are implemented in mushroom like configuration [62].

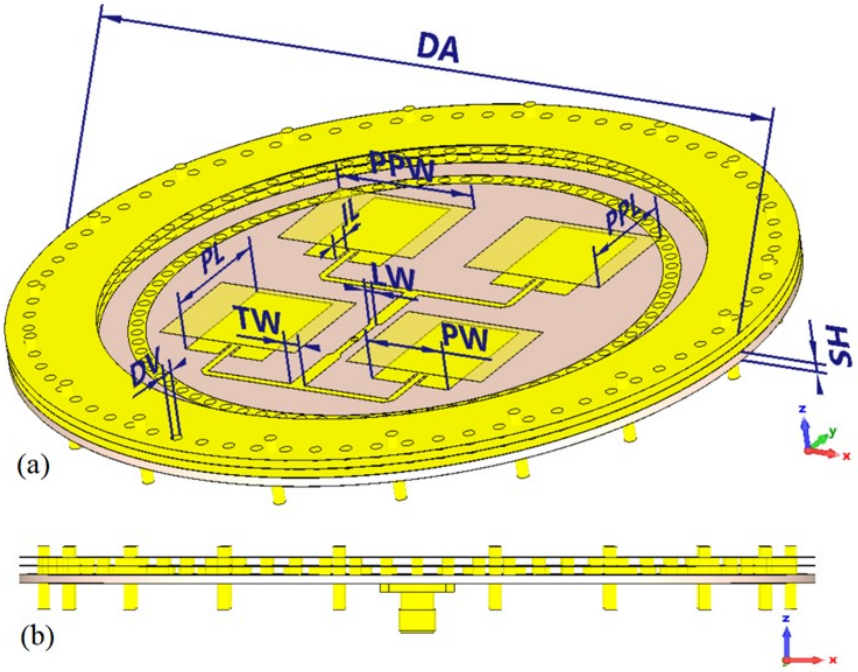

Figure 3.1 Proposed ringed stacked radio altimeter antenna (a) Perspective view with dimensions, DA=135.10 mm, DV=2 mm, PL=22.62 mm, PW=15.3 mm, PPL=19.69 mm, PPW=27.21 mm, LW=1.41 mm, TW=2.83 mm, IL=3.50 mm, SH=1.575 mm, (b) Side view.

In another configuration the EBG structures can be placed as superstrate layers above the two patch antennas [36]. This configuration has an advantage of reducing the mutual coupling of the adjacent patch antennas as well as reducing the overall size of the patch antenna array configuration along with the EBG superstrate layer. The mutual coupling reduction can also be performed by designing planar electromagnetic bandgap structures on high permittivity substrates for decreasing the size of its unit cell and designing patch antenna array on lower permittivity substrates for its directivity and bandwidth characteristics [63]. The EBG structures can be combined with split ring resonators for increasing the radiation efficiency of the antenna and reducing the mutual coupling between the antenna elements [64]. The EBG structures used for the mutual coupling reduction between radiation elements can be designed from various unit cell structures such as star, cross, square and circle configurations [65]. The stacked patch configurations can provide wide band response [51] and increased isolation between the radio altimeter patch antennas can also be realized by using via elements around the patch antennas [66].

In this paper, a concept of multilayered metallic vias with circular rings is presented with stacked patch antenna array for improving the isolation between the adjacent placed antennas

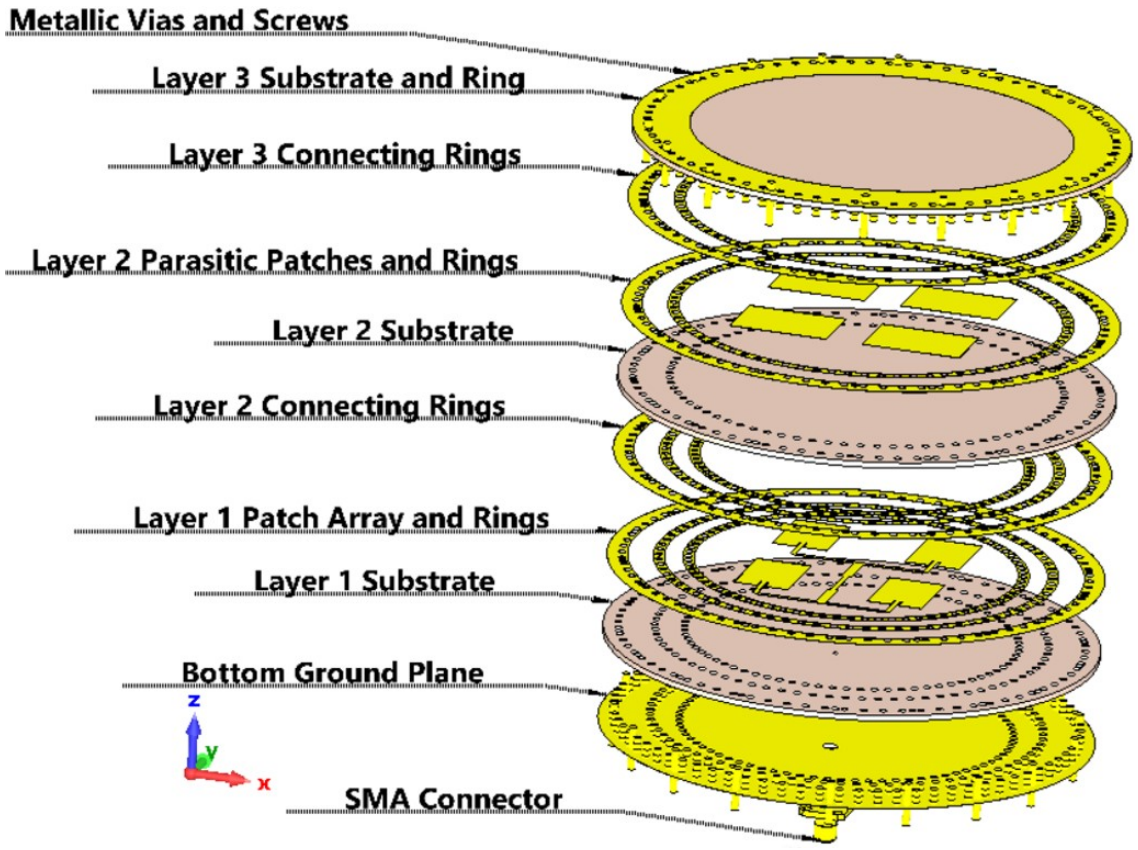

Figure 3.2 Detailed view of proposed ringed stacked radio altimeter antenna.

and increasing the bandwidth of the radio altimeter patch antennas. Compact metallic via circular rings that are coupled in the multilayered antenna array for increasing the isolation levels are introduced. The antenna design and simulation results are presented and the proposed antenna is fabricated for validation of results.

The proposed antenna is designed for better isolation, lower sidelobes, increased bandwidth and higher gain combination that leads to improved signal to interference ratio and less requirements for the transmit power compared to existing radio altimeter antenna concepts [11, 13, 67, 68] as summarized in Table 3.1.

3.3 Antennna Design

The low-profile antenna configuration is presented in Figure 3.1. It is designed with multilayered configuration for enhancing the bandwidth. Metallic via elements with parasitic metallic rings are placed circularly along the radiating elements for achieving low sidelobe levels as shown in Figure 3.1. The elements are placed in the three substrate layers for achieving high

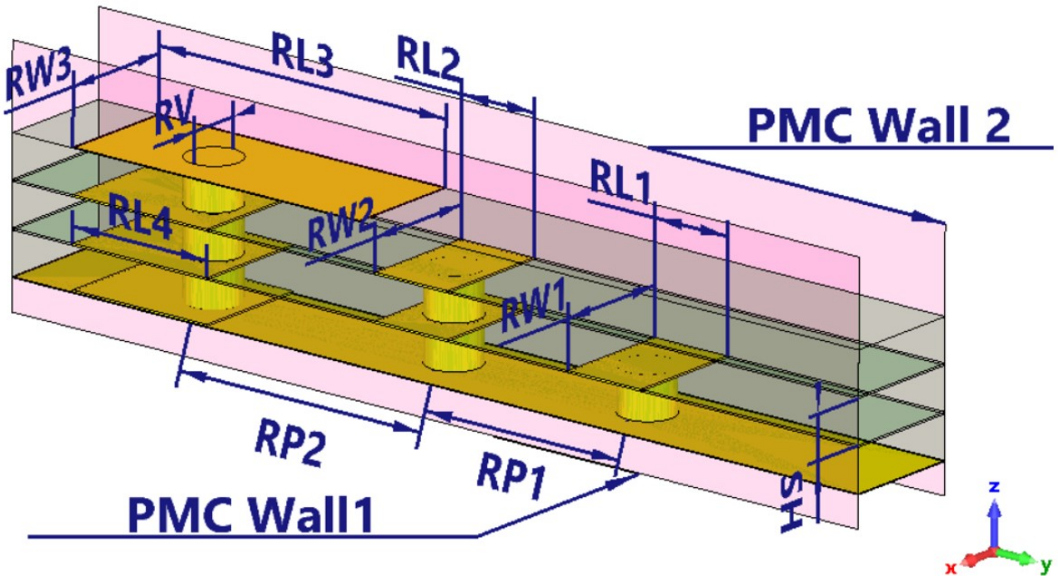

Figure 3.3 Proposed 1D layered ringed EBG unit cell diagram and labels, RL3=11.85 mm, RW3=4.42 mm, Rl2=3.0 mm, RW2=4.42 mm, RL1=3.0 mm, RW1=4.42 mm, RL4=5.5 mm, RV=2.0 mm, SH=1.575 mm, RP2= 9.95 mm, RP1=8.0 mm.

isolation levels. The detailed layers configurations are presented in Figure 3.2 exploded view. The lower bottom layer comprises a 2 by 2 patch array with a microstrip feeding network for directional radiation pattern which, is suitable for radio altimeter applications. The middle layer consists of parasitic patch elements and are designed for enhancing the bandwidth of the antenna. The third top substrate layer is a superstrate layer. All three substrates consist of Rogers 5880 laminate with dielectric constant of 2.2 and thickness of 1.575 mm, with copper cladding of 17 microns. Layers are glued together with 3M^{TM} Adhesive Transfer Tape 9461P with a thickness of 0.03 mm, relative permittivity of 2.92, loss tangent of 0.025 (manufacturer's data is only available at 1 KHz). Pressure is applied with a hydraulic press, so all possible air gaps are eliminated.

The metallic vias are placed in circular configuration along the radiation elements in the three substrate layers as shown in Figure 3.2. In addition to providing the high isolation and low sidelobes, the role of the rings is to make sure there is an electrical contact between the extremities of the vias on the three layers. This is also the reason there are two identical layers of the rings printed on the two faces of touching substrates. The metallic vias are connected with circular ring plates. The overlapping of the circular metallic rings on the top and middle layers is optimized for minimizing the sidelobe level.

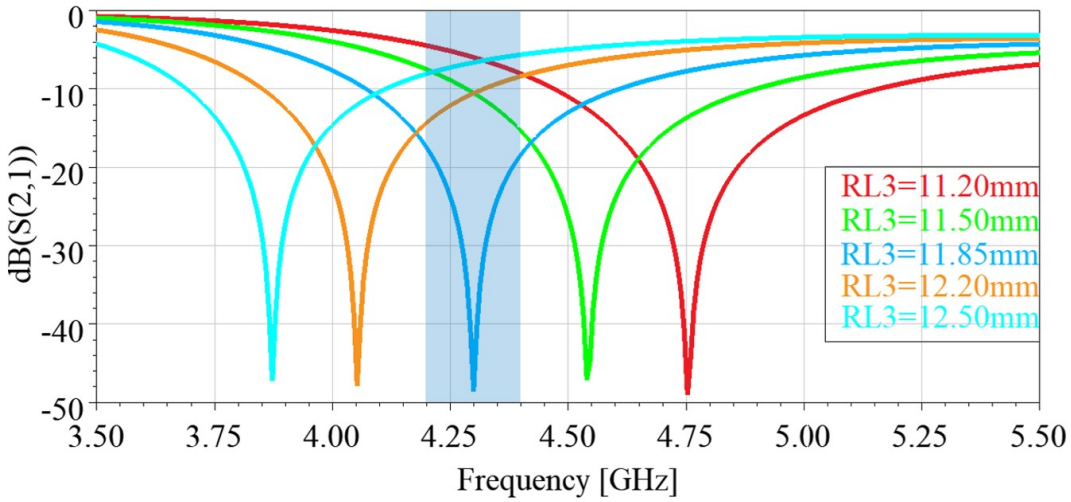

Figure 3.4 Simulated 1D ringed EBG unit cell analysis for ring length.

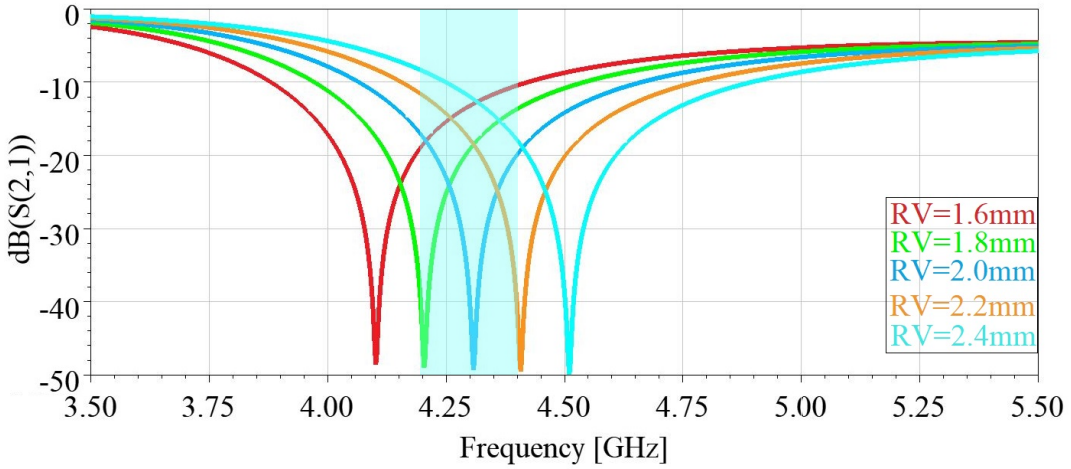

Figure 3.5 Simulated 1D ringed EBG unit cell analysis for via.

3.4 Layered 1D EBG Unit Cell Design and Analysis

In order to evaluate the efficiency of the EBG, it is first simulated by assuming an infinite 1D array of unit cells. The one dimensional EBG structure is presented in Figure 3.3. To simplify the analysis, we consider an infinite linear array of cells along the x direction, with period RW3. This is an approximation of the circular cell arrangement used in the antenna, but it is useful for simulating and optimizing the isolation performance with only one unit cell, using waveports and periodic boundary conditions.

Waveports are implemented along the y direction and PMC walls are implemented in planes

x=0 and x=RW3. A PEC wall is added at z=10.4 mm to limit the size of the volume simulated Ansys-HFSS. The metallic vias along with the rings in the three layers are designed for currents suppression in broadband frequency. Vias are inspired from EBG structures in which rows of top-loaded vertical post forming a mushroom are used to create a high surface impedance, preventing propagation along the ground plane. Variants of this are presented in Refs. [56] to [60].

In our work, a three-layer version of this was necessary to achieve the highly demanding isolation and sidelobe level of radio-altimeter antennas. The 10-dB return loss band of interest for the radio-altimeter application is from 4.2 to 4.4 GHz. The S21 transmission parameter between the two ports as a function of frequency is shown in Figure 3.4 and Figure 3.5. A strong attenuation band created by the EBG can be observed at the band of interest. Parameter RL3 (length of the upper layer ring) is used to control the center frequency with -10 dB S21 band from 4.05 GHz to 4.65 GHz. The propagation suppression at several frequencies when RL3 is set to 11.85 mm is demonstrated in Figure 3.4.

With the increase in the via diameter the inductance of the structure decreases and the frequency increases as shown in Figure 3.5. The optimal value of the via diameter is 2 mm with resonant frequency centered at 4.3 GHz for the radio altimeter band as shown in Figure 3.5. The resonant frequency at 4.3 GHz can be achieved with other combination of values for RV and RL3 and the current values are optimized for achieving the lowest side lobe levels of less than 40 dB for the antenna. The wave propagation is from right to left and as seen from the Figure 3.6(d) to Figure 3.6(f), the complex E-fields are highly attenuated at the output port in the radio altimeter band of operation.

3.5 Simulation and Analysis

Based on the results of Figure 3.4, Figure 3.5 and Figure 3.6, the EBG unit cell has been used in the antenna as shown in Figure 3.2. The design and optimization were performed in CST Microwave Studio frequency domain solver. The simulated and measured frequency response of the proposed antenna is shown in Figure 3.7. The measured 10-dB return loss band is from 4.04 GHz to 4.52 GHz and is in close agreement with the simulated frequency response, which includes the radio altimeter frequency band of 4.2 GHz to 4.4 GHz. The proposed antenna was designed for achieving the lateral isolation required between the transmitting and receiving radio altimeter antennas installed on the aircraft with standard requirement of more than -85 dB isolation with the antenna spacing of 508 mm apart [13]. The simulated S21 frequency response of the two antennas aligned in the H plane is shown in Figure 3.8.

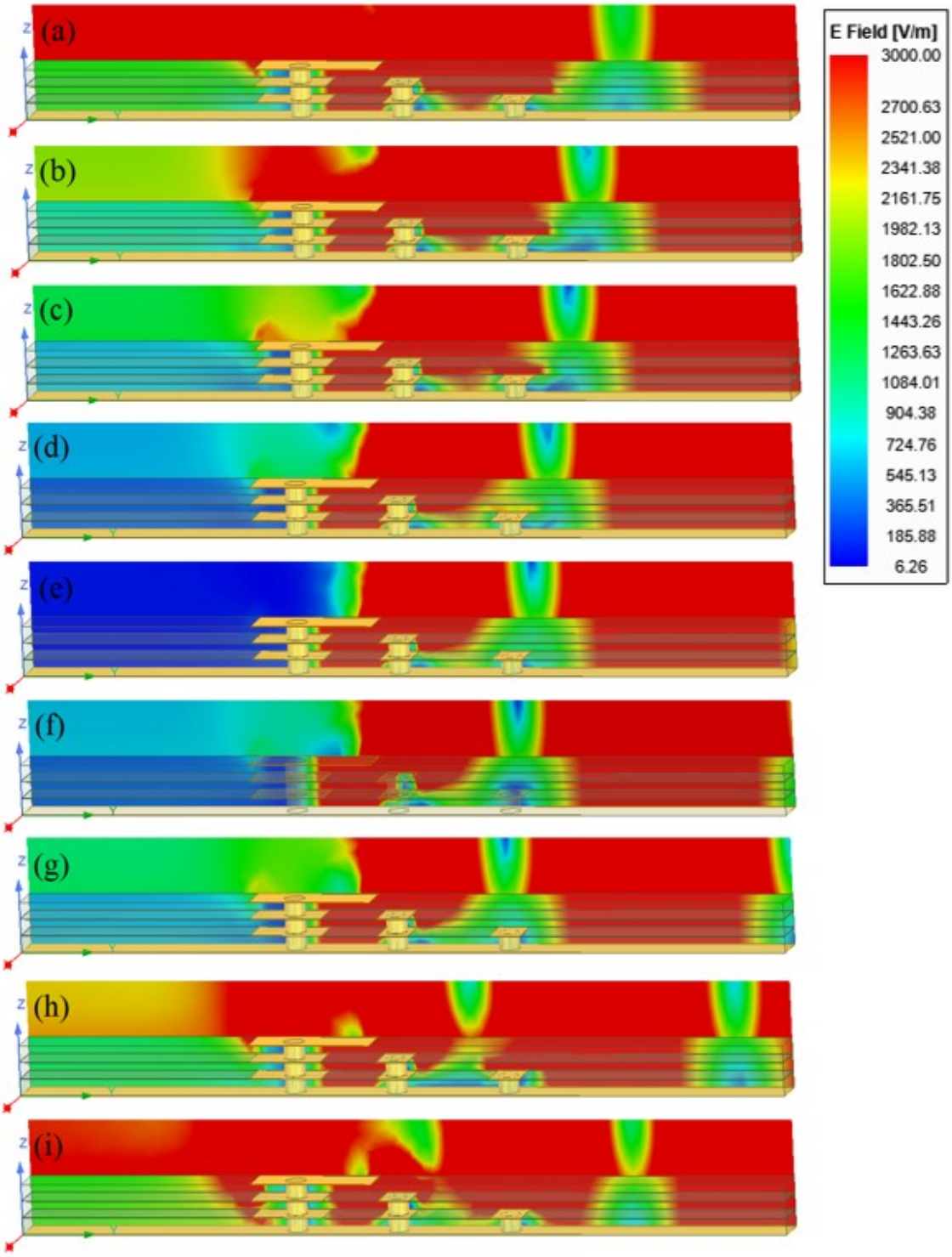

Figure 3.6 Simulated complex E-fields of proposed unit cell of one dimensional three layered ringed and via EBG (a) 3.8 GHz, (b) 4.0 GHz, (c) 4.1 GHz, (d) 4.2 GHz, (e) 4.3 GHz, (f) 4.4 GHz, (g) 4.5 GHz, (h) 4.9 GHz, (i) 6.0 GHz.

The two proposed antennas are placed on a large ground plane of 940 mm x 400 mm with the center-to-center spacing of 600 mm as shown in Figure 3.8. The measured isolation levels for the two proposed antennas are -111.98 dB at 4.28 GHz. The results show that the maximum isolation levels increases by 23.01 dB in comparison with a pair consisting of the two commercial antennas, and by 18.25 dB in comparison with a pair of proposed antenna and commercial antenna, by using the two proposed antennas. On average in the 4.2-4.4 GHz band the isolation is 81.40 dB, 82.75 dB and 84.65 dB respectively for these three cases.

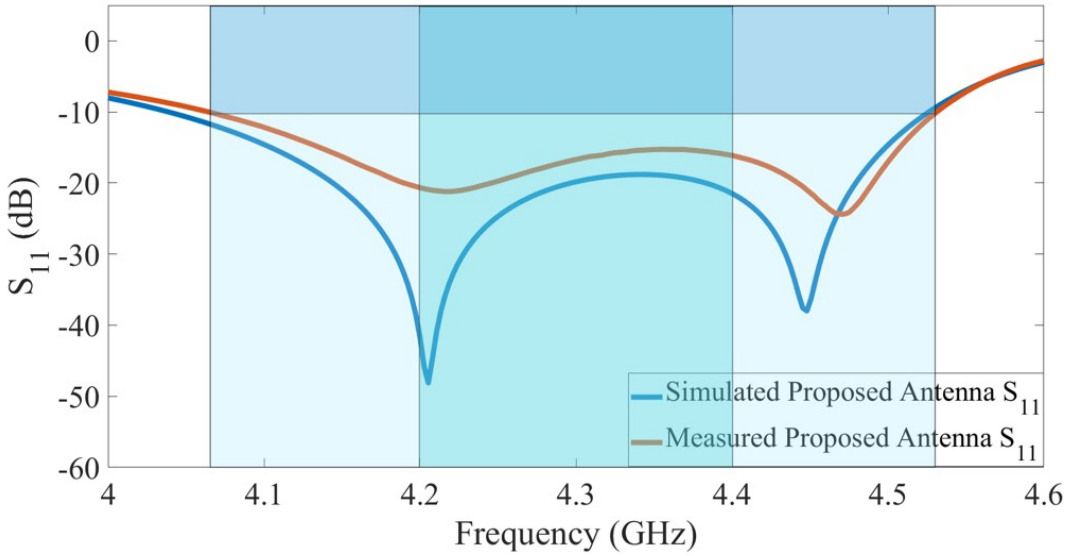

Figure 3.7 Simulated and measured return loss response of proposed antenna.

Table 3.1 Performance comparison of proposed antenna with similar published papers and commercial products. "-" indicates non available data.

	Frequency	Bandwidth	Gain	Sidelobe level	Isolation 20 inch
This work	4.04-4.52 GHz	480 MHz	12 dBi	-42.5 dB	112 dB
[13]	4.2-4.4 GHz	200 MHz	9.5 dBi	-40 dB	88 dB
[67]	4.2-4.4 GHz	200 MHz	10 dBi	-40 dB	75 dB
[11]	4.18-4.39 GHz	210 MHz	8 dBi	-	more than 50 dB
[68]	Center 4.18 GHz	-	3.75 dBi	-	-

The increased H-plane isolation obtained by adding the rings and vias can also be observed in the surface currents on the ground plane region surrounding the antenna. The surface currents on all the metallic parts of the proposed antenna at the frequency of 4.3 GHz is shown in Figure 3.9. As can be seen, the proposed configuration that includes vias and rings slightly reduces the lateral surface currents on the ground plane along the H-plane.

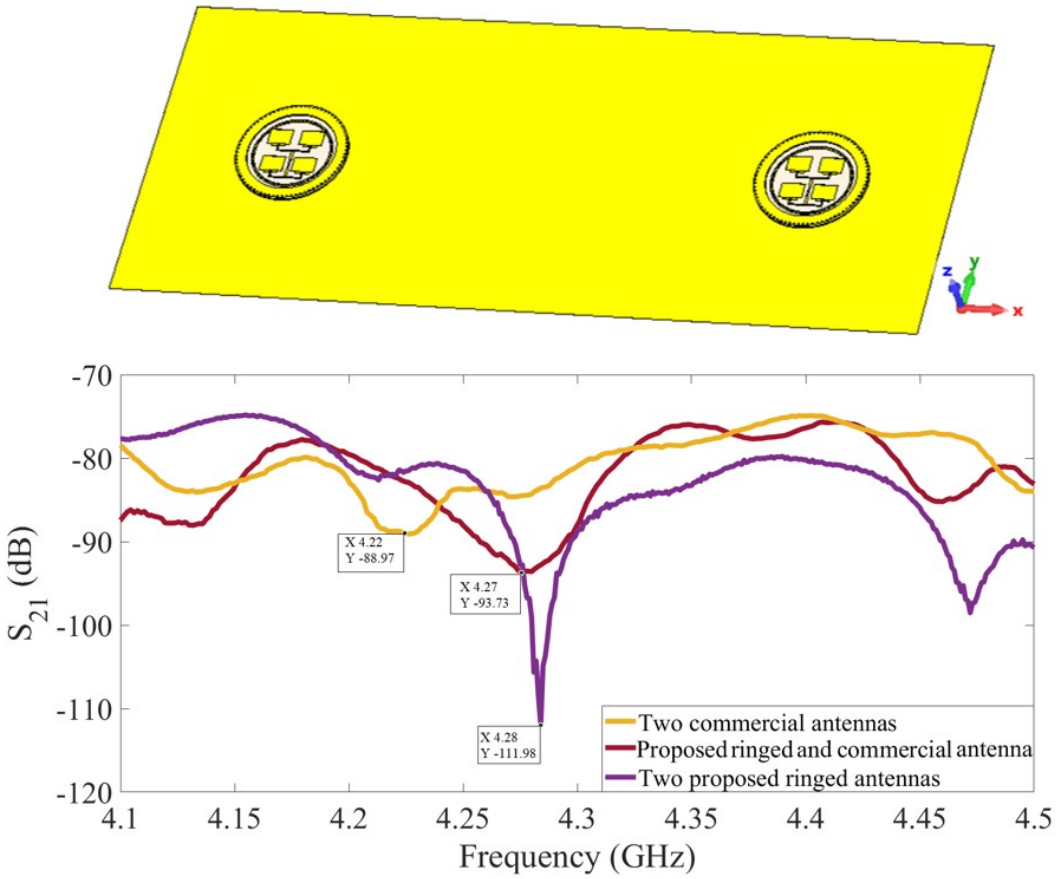

Figure 3.8 Measured isolation of proposed antenna.

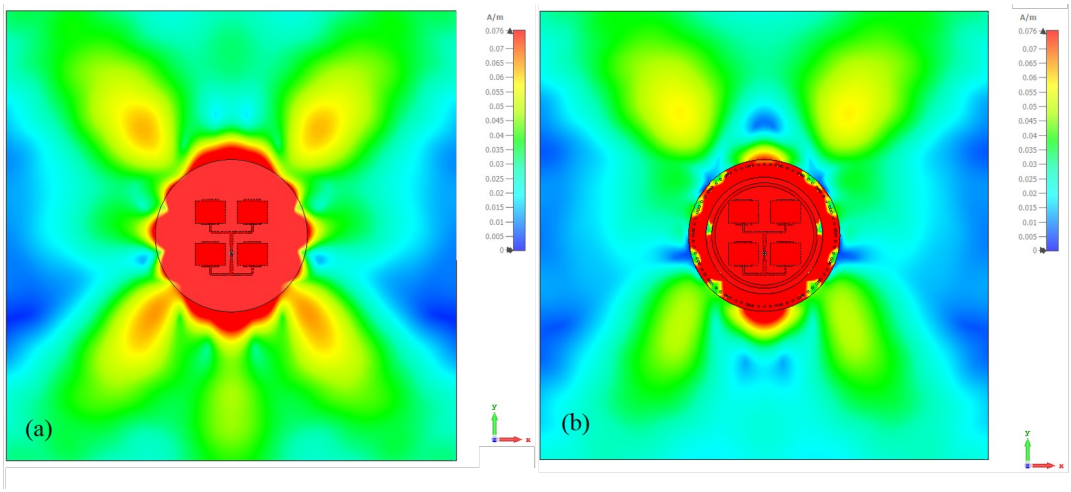

Figure 3.9 Simulated surface currents of proposed antenna at 4.3 GHz, (a) without metallic vias and circular rings, (b) with metallic vias and circular rings.

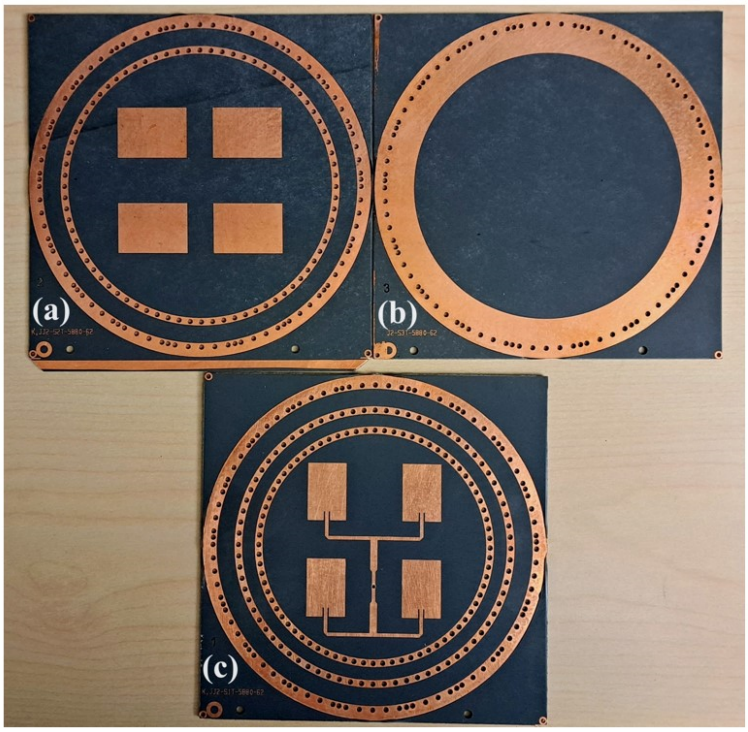

Figure 3.10 Proposed ringed radio altimeter antenna fabricated layers (a) Middle, (b) Top and (c) Bottom.

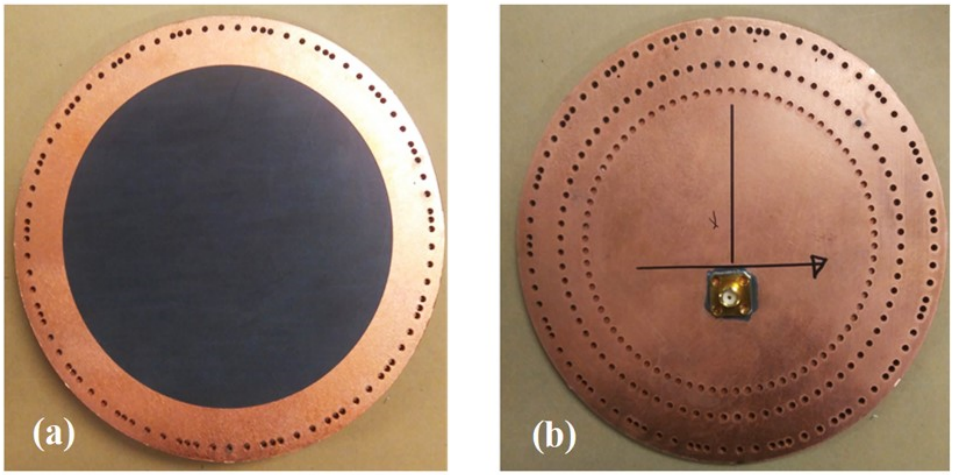

Figure 3.11 Proposed stacked antenna fabricated views (a) Top and (b) Bottom.

The three fabricated layers are shown in Figure 3.10 and the final stacked assembly top and bottom views are presented in Figure 3.11. The frequency response of the proposed antenna was measured in VNA and radiation patterns for the proposed antenna mounted on the

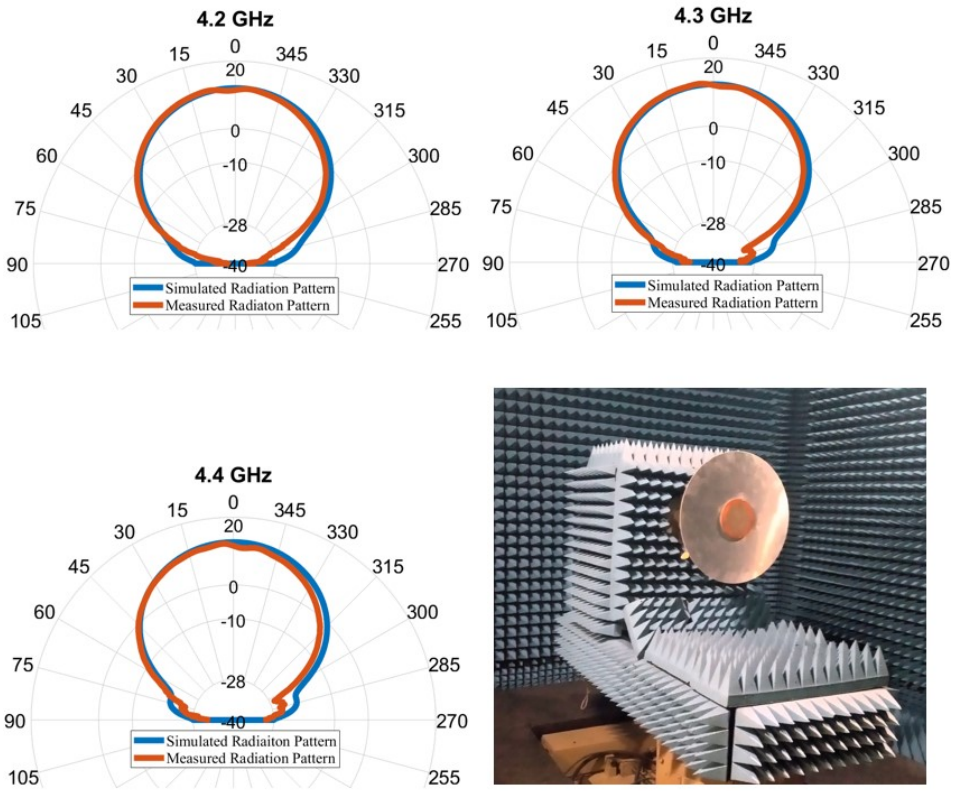

Figure 3.12 Measured and simulated 2D H-plane radiation patterns of proposed antenna and measurement setup.

ground plane having diameter of 400 mm was measured in an anechoic chamber.

The measured radiation patterns with 40 cm ground plane and simulated radiation patterns with infinite ground plane of the proposed antenna in the H plane are shown in Figure 3.12. At 4.3 GHz the measured co-polarized gain at boresight is more than 12 dB and, the gain is -42.52 dB at 90 degrees in the H-plane. Measured co- and cross-polarized radiation patterns in H-plane are plotted in Figure 3.13. The cross-polarization discrimination is 27 dB in the main beam direction.

In the radio altimeter terminology, the relative level of radiation at 90 degrees with respect to the boresight direction of radiation is called sidelobe level, although there is not always a sidelobe at 90 degrees. The term “sidelobe” is used in literature and commercial datasheets to refer to this relative radiation level. The measured and simulated gain and sidelobe levels of the proposed antenna with ground plane over the frequency band of 4.2 GHz to 4.4 GHz are summarized in Table 3.2.

The simulated three-dimensional radiation pattern of the proposed antenna is presented in

Figure 3.14, with the main beam gain of 12.3 dB and side lobe level is suppressed with level of -41.31 dB at 4.3 GHz as a result of the designed circular 1D EBG rings.

The effect on the drag coefficient of the aircraft was computed using the OpenVSP design software [69]. The proposed transmitting and receiving antennas are placed under the fuselage of the Cessna 210 aircraft as demonstrated in Figure 3.15. The drag coefficient computation is performed with the flow conditions that includes the aircraft velocity of 220 km per hour and altitude of 915 m. The corresponding drag coefficient of the fuselage is computed to be 0.00388 with and without the proposed antennas. The low profile design characteristics of the proposed ringed stacked radio altimeter antenna demonstrates no effects on the drag coefficient of the aircraft fuselage.

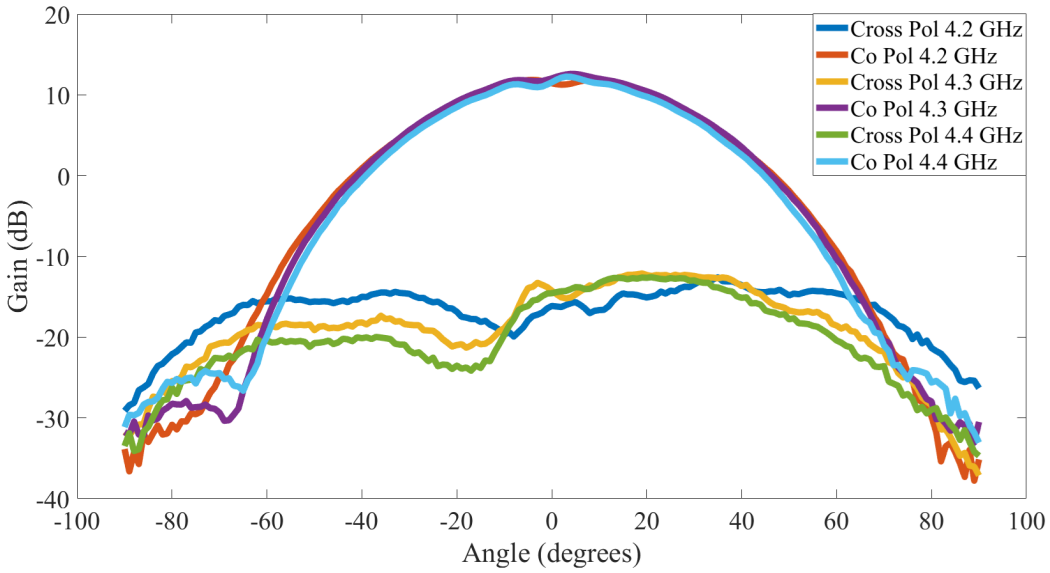

Figure 3.13 Measured co and cross polarization H-Plane radiation patterns

Table 3.2 Measured and simulated gain and sidelobe levels of the proposed antenna

Antenna Pattern	Measurement	4.2 GHz	4.3 GHz	4.4 GHz
Measured Radiation Patterns	Gain 0 degree	11.43 dB	12.03 dB	11.56 dB
	Gain 90 degree	-35.15 dB	-30.49 dB	-33.07 dB
	Sidelobe level	-46.58 dB	-42.52 dB	-44.63 dB
Simulated Radiation Patterns	Gain 0 degree	12.02 dB	12.3 dB	12.65 dB
	Gain 90 degree	-28.09 dB	-29.01 dB	-28.02 dB
	Sidelobe level	-40.11 dB	-41.31 dB	-40.67 dB

The total drag coefficient of the aircraft without the two radio altimeter antennas is 0.01526. The drag coefficient of the two antennas is 0.00004, contributing 0.24 percentage to the total

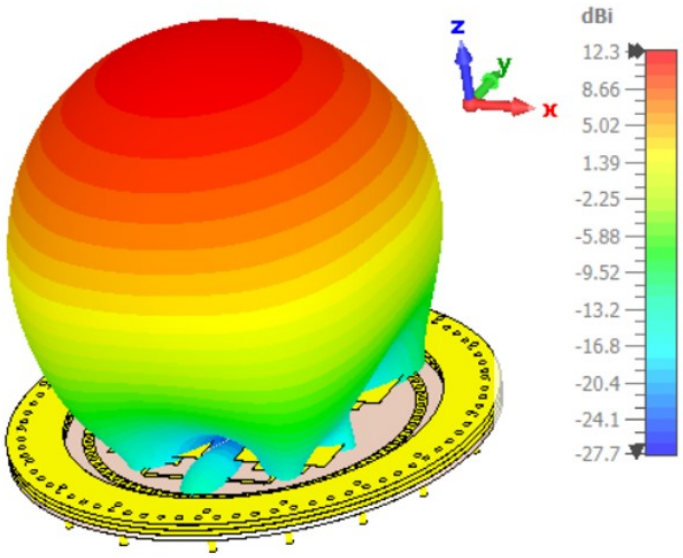

Figure 3.14 CST simulated 3D radiation pattern of proposed antenna at 4.3 GHz.

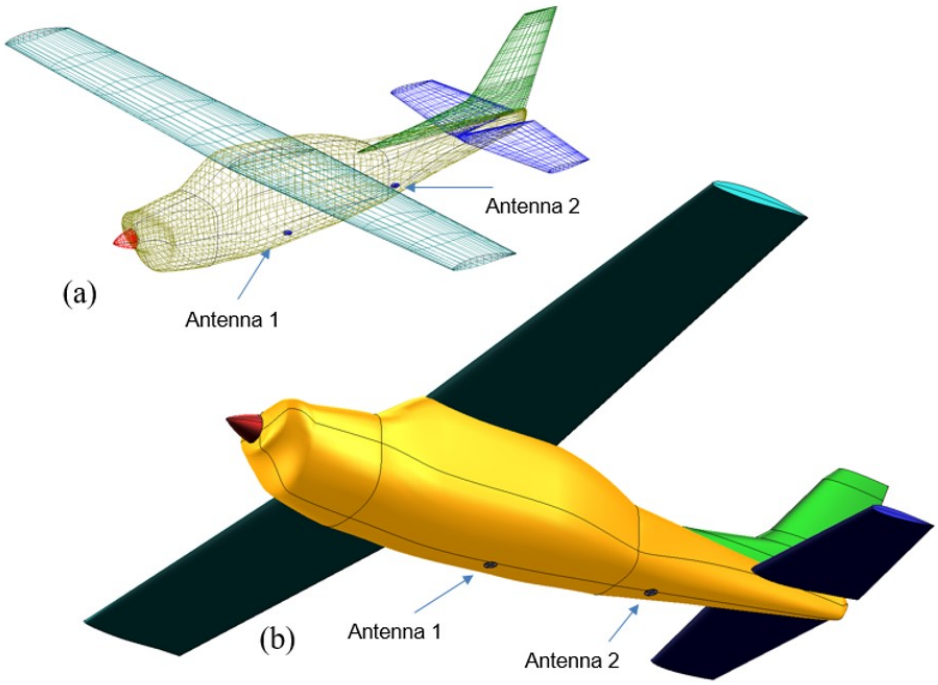

Figure 3.15 Setup used for drag coefficient computation in OpenVSP software of antennas placed under Cessna 210 fuselage, (a) Top View, (b) bottom view.

drag coefficient of the aircraft that is now 0.01529. At the center frequency 4.3 GHz the proposed antenna has a measured gain of 12 dB which is approximately 2.5 dB more than

typical commercially available radio altimeter antennas, while the ratio of areas occupied by each antenna is only 1.8 dB. This corresponds to a 0.7 dB improvement in aperture efficiency. Assuming a radio altimeter system with identical antennas for Tx and Rx, the signal to interference ratio (S/I) at the receiver is proportional to $(G(0^o)/G(90^o))^2$.

For the proposed antenna, $G(0^o)/G(90^o)$ is 42.5 dB, i.e. 2.5 dB above the level typically specified in commercial antenna datasheets. In that case, using our proposed antenna would increase (S/I) by 5 dB, meaning that for the same S/I, the transmit power can be reduced significantly, reducing energy consumption of Tx power amplifiers accordingly.

3.6 Conclusion

The ringed stacked radio altimeter patch antenna is presented in this paper. Low sidelobe level of less than -40 dB are obtained in the H-plane for the achieving isolation levels of more than 85 dB. The surface current plots are presented for demonstrating the reduction in the lateral surface currents on large ground plane along the H-plane of the antenna. Simulation showed that the proposed antenna mounted on a small aircraft has negligible effect on drag. Better performance is achieved of the proposed antenna in comparison to commercially available antennas in terms of bandwidth with the frequency response from 4.06 GHz to 4.53 GHz is achieved as compared to the frequency band of 4.2 GHz to 4.4 GHz. Isolation of between the two proposed antennas is -111.98 dB is achieved at 4.28 GHz. The proposed antenna is designed with high gain of 12 dB and sidelobe levels of -42.5 dB are achieved with increased signal to interference ratio of more than 5 dB as compared to available commercial radio altimeter antennas.

CHAPTER 4 ARTICLE 2: MULTIBAND DISTANCE MEASURING EQUIPMENT, TRAFFIC COLLISION AVOIDANCE SYSTEM AND RADIO ALTIMETER ANTENNA FOR AVIONICS APPLICATIONS

Omar Masood Khan and Jean-Jacques Laurin

Submitted in IEEE Open Journal of Antennas and Propagation

Submission date: April 29, 2025

4.1 Abstract

A multiband antenna is presented for aircraft communication of traffic collision avoidance system (TCAS), distance measuring equipment (DME) and radio altimeter (RadAlt). This single antenna concept provides benefits of reducing the number of mounted antennas on the aircraft. Dual and single feed multilayered antennas are designed for omnidirectional and directional radiation characteristics. A circular metallic covered low profile cavity is designed for omnidirectional radiations that comprises a novel power splitter for feeding the patch array placed on upper substrate of the circular cavity for achieving directional radiation pattern characteristics. An electromagnetic bandgap (EBG) layer is designed and placed within the circular cavity for suppressing higher order resonances interfering with the frequency band of RadAlt at 4.3 GHz. The proposed antenna was fabricated and tested in an anechoic chamber for the verification of radiation characteristics.

4.2 Introduction

Aircraft antenna systems present critical design challenges due to the interoperability of the aircraft communication systems and placement of the antennas on the airframe with limited space. Antennas for avionics systems are placed on the different locations of the fuselage of the aircraft based on the navigation, landing and takeoff requirements of the aircraft. Traffic collision avoidance system (TCAS) antenna is placed on both upper and lower fuselage as TCAS is an essential aircraft system and is used for avoidance of any aircraft collisions by communicating and analyzing relative position, direction of approach and speed of the close by aircrafts on trajectories that can cause collision.

Distance Measuring Equipment (DME) antenna and radio altimeter (RadAlt) antenna are also placed on the lower side of the fuselage, as the DME measures the distance between the

ground station and the aircraft and radio altimeter measures the aircraft altitude from the ground [9]. TCAS antenna is vertical polarized with omnidirectional radiation pattern in the frequency band of 1030 MHz to 1090 MHz [27] and the height of the radiating element can be reduced by using top loading [23]. Low profile TCAS antenna can be designed by using monopole antenna configuration for omnidirectional radiation patterns and connection of the parasitic elements can be switched with the ground plane for steering the beam in the directional radiation pattern mode of the antenna [24].

Standard DME antenna consists of blade antenna configuration for omnidirectional radiation in the frequency band from 960 MHz to 1215 MHz [52] and can be designed with printed slots on a dielectric layer [19]. A DME antenna with low profile configuration can be designed with wideband antenna characteristics by using monopole antenna in a profiled configuration [20]. The bandwidth of the antenna is optimized by shaping the profile of the monopole. The monopole is embedded within cavity hence providing low profile antenna characteristics [20].

Omnidirectional radiation pattern can also be realized with low profile configuration by using circular patch with shorting pins and fed at the center with probe [15] and coupling loops are used for increasing the gain of the antenna [17]. The circular patch with shorted pins concept can provide omnidirectional radiation pattern characteristics with low profile and can be suitable for DME applications [53]. Automatic dependent surveillance broadcast (ADS-B) antennas required omnidirectional radiations for the frequency band of 1089-1091 MHz and is within the bandwidth of DME, which also uses vertical polarization [52].

Radio altimeter antennas are designed for the operation in 4.2 GHz to 4.4 GHz band with directional radiation pattern characteristics [13]. A novel radio altimeter antenna designed in our recent work provides directional radiation pattern characteristics with low side lobe and high isolation levels by embedding a one-dimensional ringed electromagnetic band gap structure (EBG) [70].

In this paper, an antenna concept is presented with multiband characteristics for DME, TCAS, ADS-B and RadAlt avionics applications. The motivation is to design multiband antenna for multiple avionics radios that can be integrated into single hardware platform using software defined avionic radio architectures as proposed in [41]. Our proposed antenna consists of low-profile and multiband configuration that provides better space utilization by placing a smaller number of antennas on the aircraft airframe and reduces the size, cost, power and weight. Two antenna configurations are designed, respectively with one-port and two-port feeding mechanisms.

The DME, TCAS and ADS-B omnidirectional radiation characteristics are achieved by designing a low-profile circular metallic layer with shorted vias that provide bandwidth en-

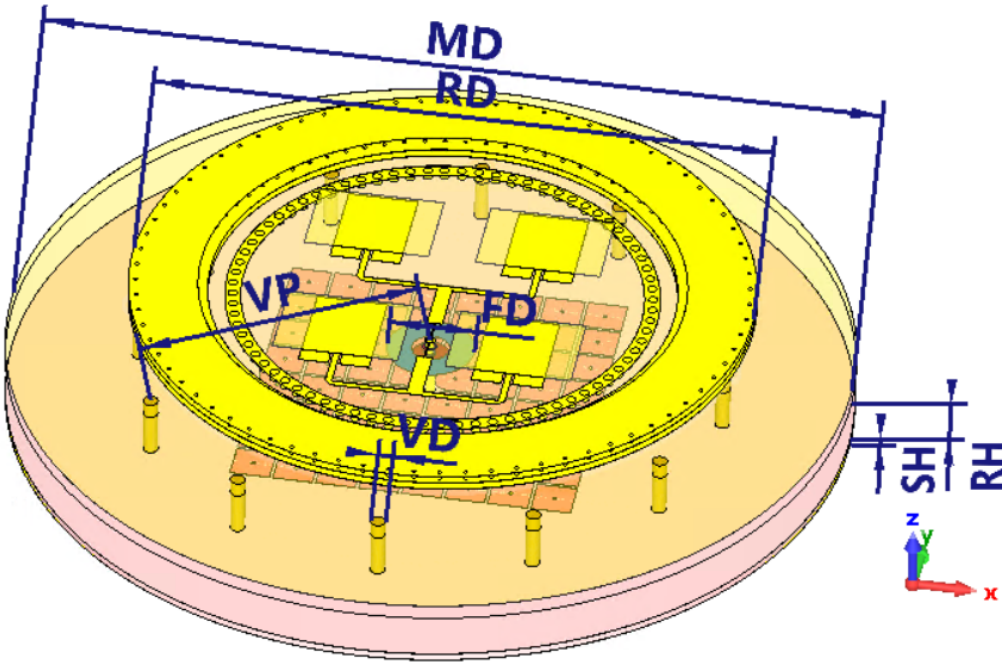

Figure 4.1 Proposed single port distance measuring equipment and radio altimeter antenna perspective view with dimensions, MD = 182.4 mm, RD = 135.1 mm, FD = 19 mm, VP = 63.5 mm, VD = 3.175 mm, SH = 1.575 mm and RH = 9.52 mm.

hancement. The cavity is excited by a vertical probe connected to an inner feeding circular patch in the cavity. The proposed antenna comprises two differently designed EBG layers embedded in the upper and lower layers of the antenna. As detailed in [70], directional radiation pattern for the RadAlt application is achieved by designing stacked patch antenna array and first ringed EBG for sidelobe level reduction. The dual-port feeding provides separate feeding for both the metallic L-band circular cavity and the C-band patch array, whereas single feeding is achieved with a three-dimensional power splitter that carries both the L-band (DME, TCAS, ADS-B) and C-band (Rad-Alt) signals. This splitter is built into the L-band circular cavity. In order to prevent propagation of guided C-band signals within the cavity, a second EBG layer is designed within the metallic circular cavity. The two proposed antenna concepts are fabricated and tested for validation of the simulated results.

4.3 Antenna Design

The proposed multiband antenna is designed with a multi-layer configuration with a lower section comprising the metallic shorted circular cavity for omnidirectional radiation pattern and upper layers consist of the patch array for directional radiation pattern, as shown in

dimensions labeled diagram of Figure 4.1. Two antenna configurations are presented with single and dual feeding mechanisms as shown in Figure 4.2. The dual feeding approach consists in feeding the metallic cavity with circular feeding patch M3 within the metallic cavity that is separated from the ground plane M1 with rexolite layer S2 of height 9.52 mm and dielectric constant of 2.53, as shown in Figure 4.2(a), and substrate layer S3 made of Rogers 5880. The feeding patch M3 is printed on the top surface of S2. All the Rogers 5880 substrate layers used in the designing of the single and dual feed antennas have same specifications with dielectric constant of 2.2, loss tangent 0.0009 and height of 1.575 mm.

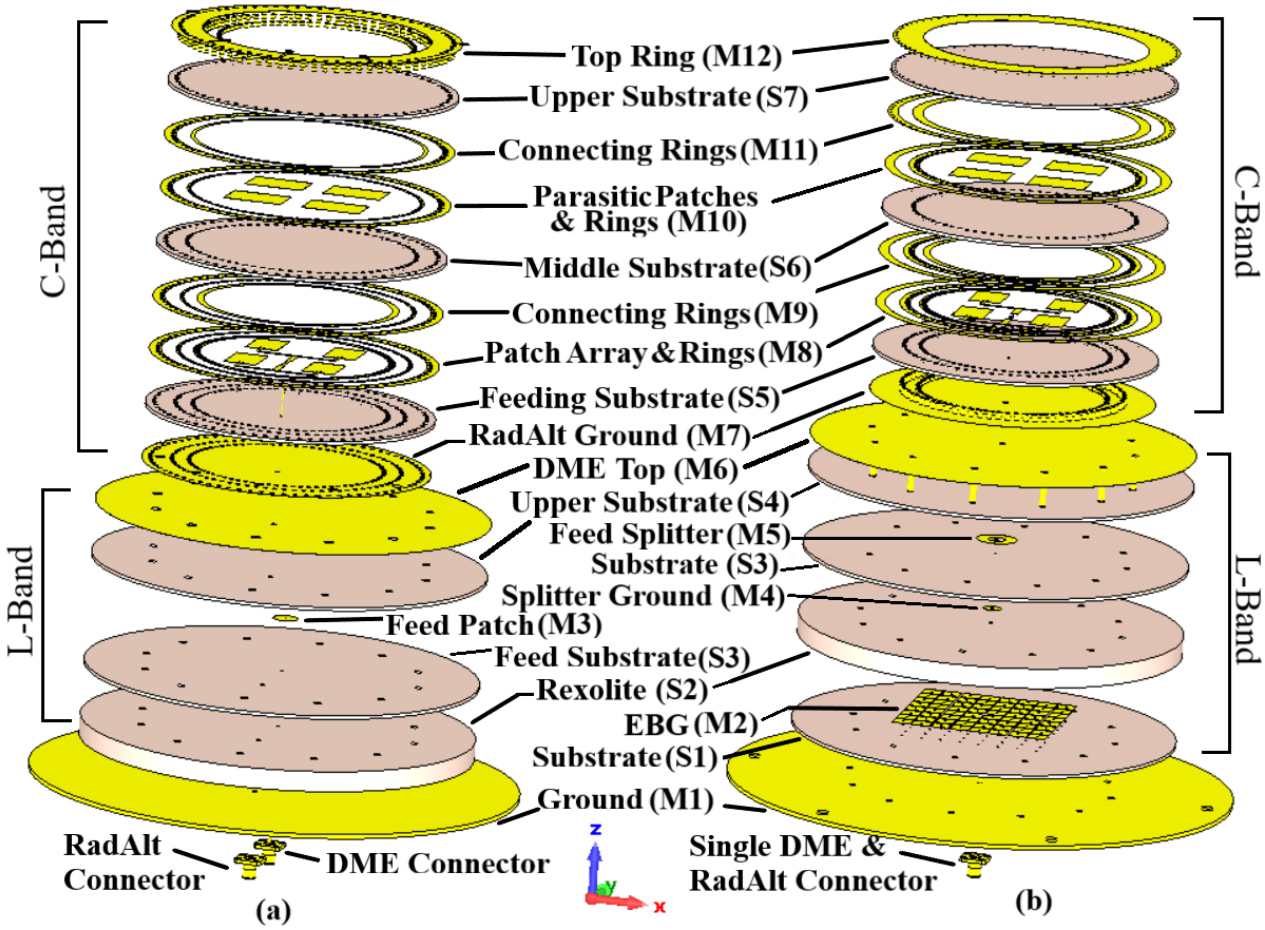

Figure 4.2 Detailed view of proposed hybrid distance measuring equipment and radio altimeter antenna (a) Dual Port, (b) Single Port.

The patch array layers are placed above the metallic circular top M6 of the cavity for both single and dual feed antennas as shown in Figure 4.2(a) and Figure 4.2(b). The metal layers M7 to M12 on substrates S5 to S7, that constitute the upper section of the antenna with directional pattern characteristics for RadAlt applications, are shown in Figure 4.2(a) and Figure 4.2(b). These metal layers are similar in both the 1-port and 2-port proposed

antennas. The directional radiation pattern is achieved by designing 2 x 2 patch array on metallic layer M8 on top of substrate S5 and grounded metallic layer M7 below the substrate S5. Four parasitic patches on metal layer M10 above the substrate layer S6 are stacked on top of patch array layer M8 providing bandwidth enhancement and achieving the desired RadAlt frequency band from 4.2 GHz to 4.4 GHz [70]. The sidelobe levels of less than -40 dB for better isolation between the transmitting and received RadAlt antennas are realized by designing the layered circular ringed EBG on the metal layers from M7 to M12 [70]. The connecting rings on the metal layers M9 and M11 enables the connection of the vias between the substrates S5 to S7 (details can be seen in [70]).

The metal layers M1 and M6 constitutes the lower and upper metal layers of the cavity that produces the omnidirectional radiation pattern for DME, TCAS and ADS-B applications and are similar layers in both 2-port and 1-port antennas as shown in Figure 4.2(a) and Figure 4.2(b) respectively. There are 12 vias passing through the cavity, which are connected between layers M1 and M6. These vias are forming a circular partial ring producing a second resonance and is superimposed along with the first resonance of the cavity for bandwidth enhancement. An EBG layer M2 is placed below the rexolite layer in the single feed antenna as shown in Figure 4.2(b) for suppressing RadAlt signal propagation within the cavity. There is no need for EBG in the dual-port designing since the RadAlt signal is fed with a shielded cable passing through the DME cavity. Hence, this cavity is not fed with C-band signals.

The power splitter for single feeding mechanism on metallic layer M5 is fabricated on the upper copper layer of Rogers substrate S3 layer and the splitter ground metal layer M4 is fabricated on lower copper layer of substrate S3 that is placed above the rexolite layer S2 as presented in Figure 4.2(b). The circular cavity with metallic top patch M6 produces the first resonance. The second resonance superimposition on the first resonance from the circular vias is achieved by optimizing the radial distance from the cavity center of the 12 circularly placed vias within the cavity. The optimal bandwidth of the DME, TCAS and ADS-B band from 0.960 GHz to 1.215 GHz is realized by optimizing the diameter of the feeding patch at layer M3 and outer diameter of the splitter fabricated on layer M5 within the cavity.

4.4 Feeding Structures

The feeding designs of the one-port and two-port multiband antennas are presented in Figure 4.3 and Figure 4.4 respectively. For L-band feeding, the dual-port design comprises a circular patch on metal layer M3 and it is connected and excited directly by the feeding port as shown in Figures 4.3(a) and 4.3(b). The inner pin of the connector passing through the rexolite layer S2 and substrate S3 is soldered on top of the metal circular patch M3 as shown in

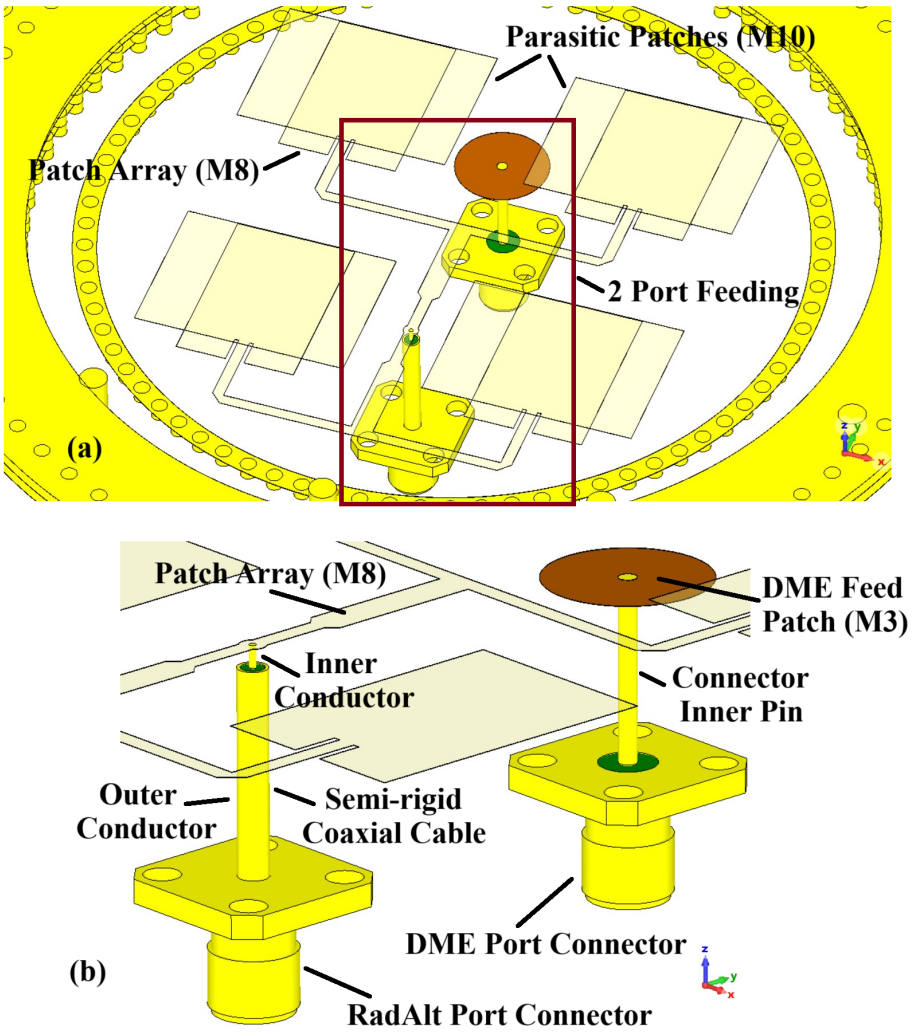

Figure 4.3 Proposed 2-port antenna feeding design, (a) Feed placement, (b) Detail zoomed view.

Figure 4.3(b). The feeding circular patch diameter is optimized for impedance matching and exciting the metallic circular cavity and for creating a first resonance in the DME frequency band. The patch array on the metallic layer M8 is fed by metallic semi-rigid cable with outer shielded metallic diameter of 2.2 mm and inner pin diameter of 0.51 mm and is passing through layers M1, S2, S3, S4 and M6 of the cavity as shown in Figure 4.3(b). The outer shield of the cable is soldered to the bottom layer M7 of the RadAlt patch array at its higher end, and with the bottom ground M1 layer of the antenna at its lower end. This RadAlt patch array feeding cable therefore acts as metallic via within the DME cavity that is offset from the center of the cavity.

In the single-port antenna, both L-band and C-band signals are fed with the same coaxial

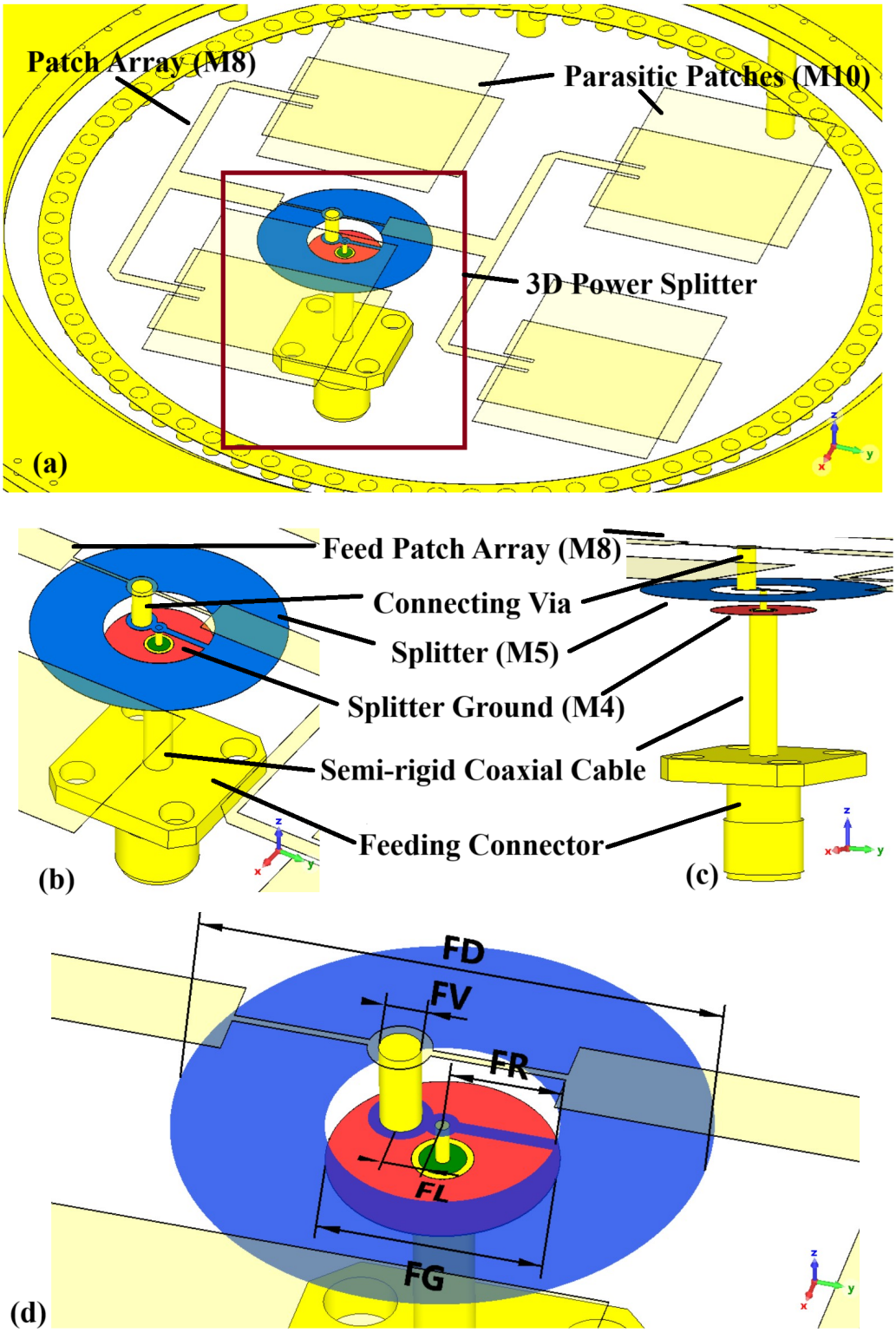

Figure 4.4 Proposed 1-port antenna 3D power splitter design, (a) Power splitter placement, (b) Zoomed view labeled, (c) Side view labeled, (d) Dimensions, FD = 19 mm, FR = 4.1 mm, FL = 1.5 mm, FV = 1.5 mm and FG = 8.2 mm.

port located in the center of the ground plane M1. In this case, a three-dimensional power splitter is designed at metallic layer M5, to remove the extra metallic offset feeding segment as shown in Figure 4.4(a). The power splitter is fed with the inner conductor of a vertical coaxial line, in the center at metal layer M5, from the single feed. At level M5, this inner conductor is soldered to a microstrip line that splits in two paths. One of the paths is used for exciting the circular ring that is feeding the DME cavity, and the other path is used for feeding the upper RadAlt patch array on level M8 by using a vertical metal via. The metal via is passing thought layers S4, M6, M7 and S5 and is connecting the metallic layers M5 and M8, as shown in Figures 4.4(b) and 4.4(c). The lower layer of the splitter consists of metallic ground ring that designed at layer M4 and is soldered at the outer conductor of the semi-rigid feed cable that is passing through the layers M1, S1, M2 and S2 as shown in Figures 4.4(b) and 4.4(c). Since the printed feeding line on level M5 is unshielded, it will generate both L-band and C-band fields in the cavity formed by M1 and M6, which is designed only for L-band radiation. An extra measure is necessary to prevent C-band signals from propagating in that cavity and be entirely directed towards the upper C-band patch array. This is realized by inserting and EBG layer, as discussed in the next section.

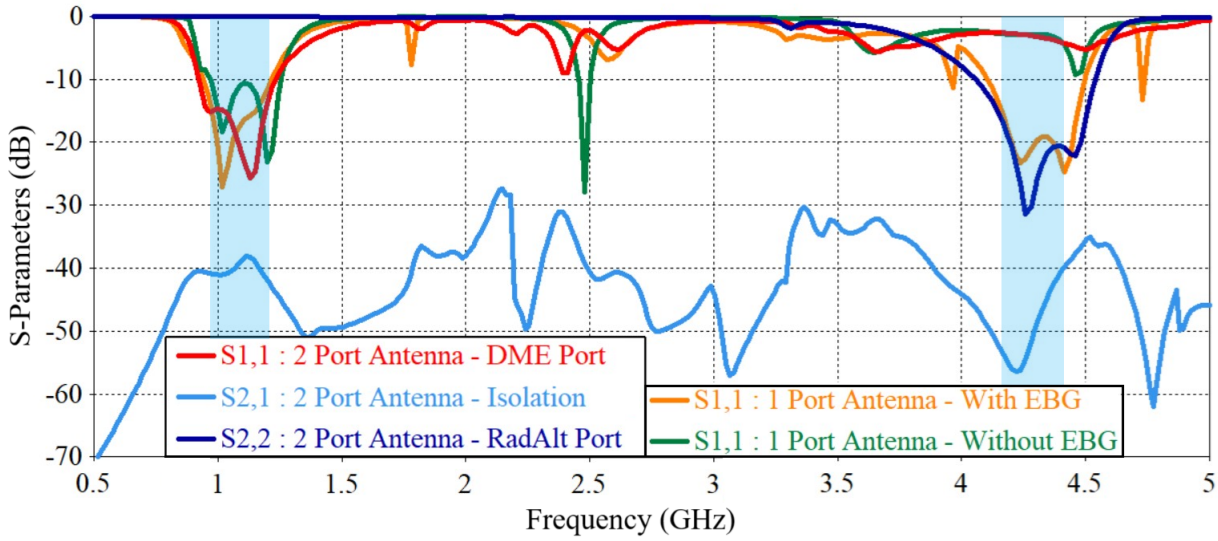

Figure 4.5 Simulated frequency response of 2-port antenna and 1-port antenna with and without EBG. The required 10-dB return loss bands are shaded in blue.

4.5 EBG Unit Cell and Layer Design and Analysis

Simulations were performed in CST Microwave Studio frequency domain solver for the designing and verification of the multiband proposed antennas. The S11 response versus frequency

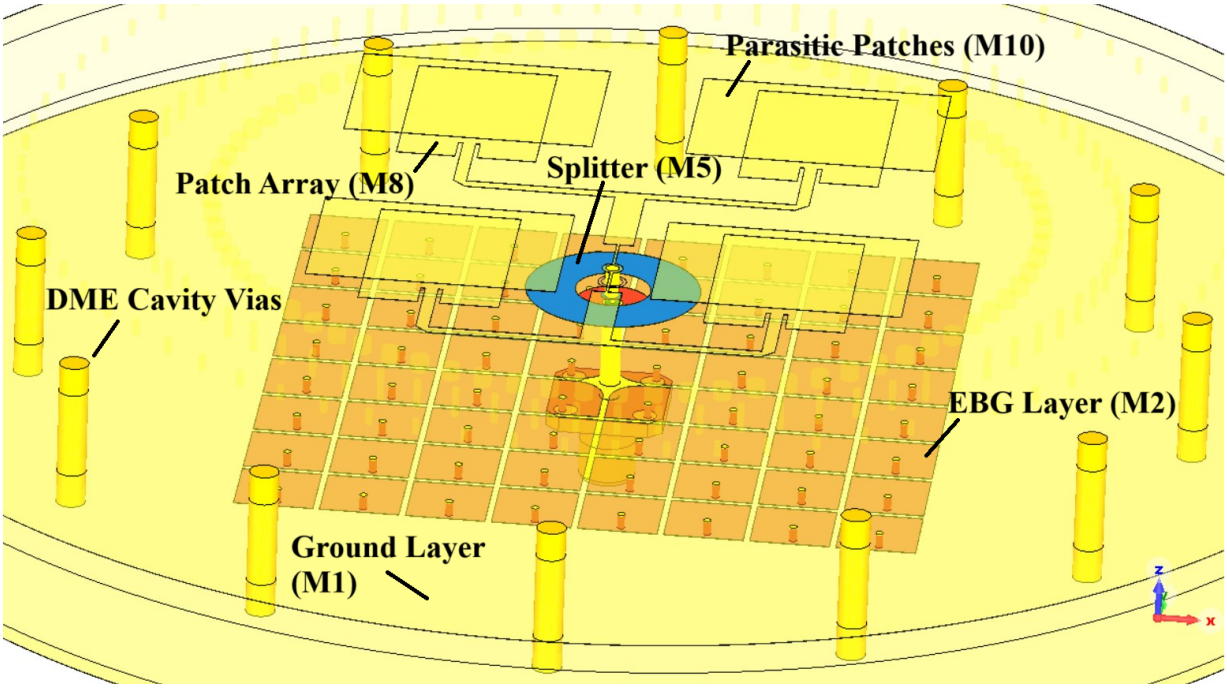

Figure 4.6 EBG layer design and placement within cavity.

at the DME port (port 1) of the dual-port proposed antenna is shown in Figure 4.5 in red color curve. The 10-dB return loss band is achieved from 0.922 GHz to 1.234 GHz that is 57 MHz greater than the required DME 10-dB return loss band of 0.960 GHz to 1.215 GHz. The dual-port RadAlt (port-2) 10-dB return loss band is achieved from 4.055 GHz to 4.53 GHz and is 275 MHz wider than the required RadAlt 10-dB return loss band from 4.2 GHz to 4.4 GHz. The frequency response of the proposed single-port antenna is shown in Figure 4.5 (green curve). The DME frequency response requirement is achieved whereas the 10-dB RadAlt return loss band is not achieved with S11 in the range of -3dB in the required band. This degradation of the RadAlt frequency response and bandwidth is due to the propagation of C-band signals in the DME cavity. Then, an electromagnetic bandgap metallic layer M2 is designed and placed within the DME circular cavity for suppressing the propagation of the RadAlt signals. The designed EBG metallic layer M2 is placed below the feeding splitter layer M5 and rexolite layer S2 within the cavity above the ground plane layer M1 as shown in Figure 4.6. The shorted patch (so-called mushroom EBG) with gap between the patches is used for the design [33]. The EBG unit cell was designed and analyzed in Ansys-HFSS as shown in Figure 4.7. The excitation ports 1 and 2 (red shaded), are implemented along the x direction at x = 0 and x = AS respectively and PMC walls (blue shaded), are implemented along y direction at y = 0 and y = AS, as shown in Figure 4.7(a). PEC wall is implemented

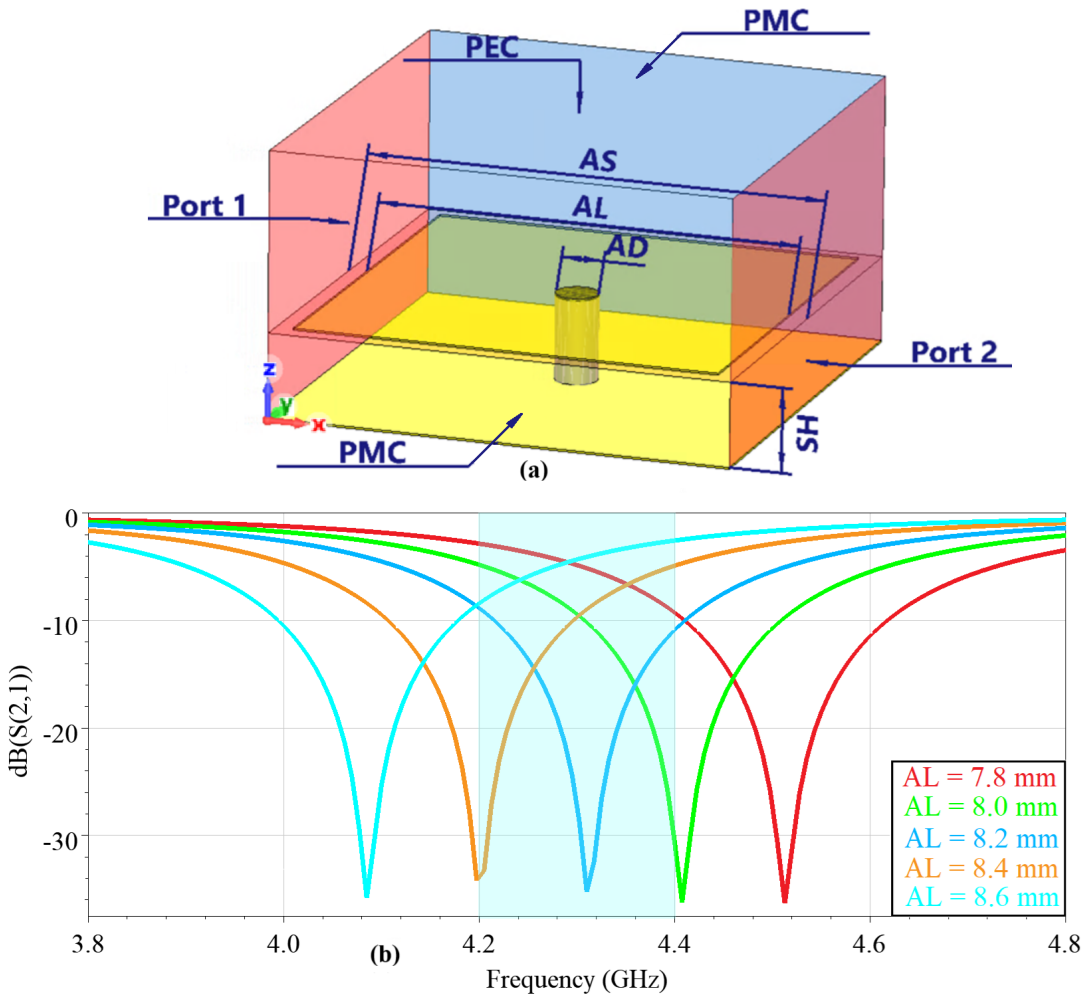

Figure 4.7 Designed EBG unit cell, (a) Labeled diagram, (b) Analysis for patch length AL.

at z = (RH+SH+SH), and this distance includes the height of the rexolite layer and substrate layers within the DME cavity placed above the EBG layer. The via diameter AD is 0.8 mm and Rogers 5880 substrate is used with height of 1.575 mm.

The EBG patch length AL is optimized for the suppression of the propagation at the RadAlt frequency response band of 4.2 GHz to 4.4 GHz as shown in Figure 4.7(b). The frequency band of the RadAlt in the single feed antenna is revived by placing the EBG array M2 layer at the bottom of cavity, having 8 x 8 number of cells. The frequency response is shown in Figure 4.5, orange curve, with 10-dB return loss of the DME band is from 0.942 GHz to 1.217 GHz and the revived RadAlt 10-dB return loss band is from 4.10 GHz to 4.49 GHz. The absence of the EBG in the single feeding configuration not only degrades the frequency response of the RadAlt band but also distorts the radiation pattern of the RadAlt, as shown

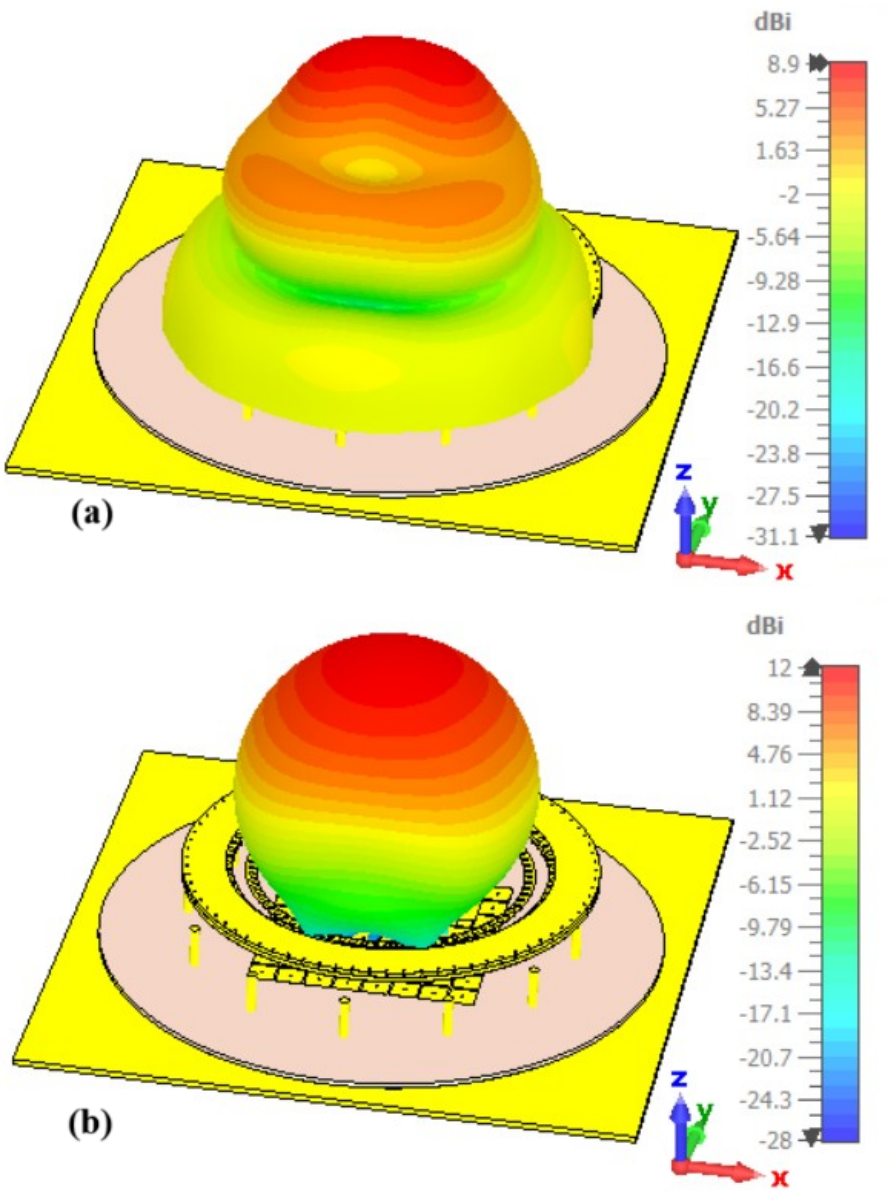

Figure 4.8 Simulated 3D gain of proposed single port antenna at 4.3 GHz, (a) Without EBG, (b) With EBG.

in Figure 4.8(a). The sidelobe levels are also increased as shown in the Figure 4.8(a). That will cause lower isolation levels between the transmitting and receiving RadAlt antennas placed under the fuselage of the aircraft. By designing and placing the EBG within the DME cavity the radiation pattern of the RadAlt is revived with directional radiation characteristics and low sidelobe levels as shown in Figure 4.8(b). The benefits of adding EBG layer in the cavity for suppressing RadAlt band signals are also visible in the surface current plots of the 1-port antenna, as shown in Figure 4.9.

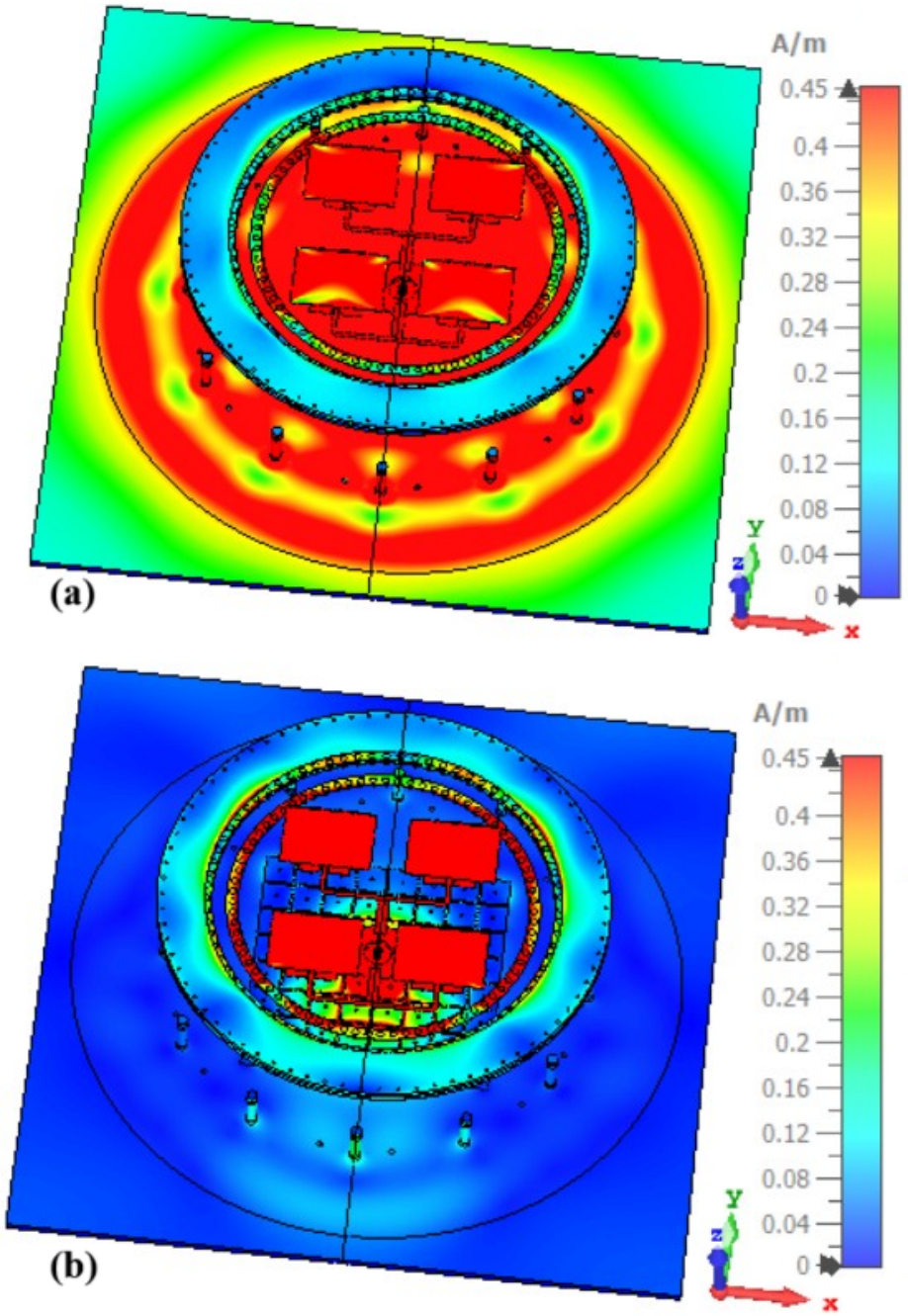

Figure 4.9 Simulated maximum surface currents of the proposed single port antenna at 4.3 GHz, (a) Without EBG, (b) With EBG.

The RadAlt signals at 4.3 GHz produces a circular current distribution within the DME cavity, as shown in Figure 4.9(a). With the design and placement of the EBG within the cavity, the circular waves are suppressed as shown in Figure 4.9(b).

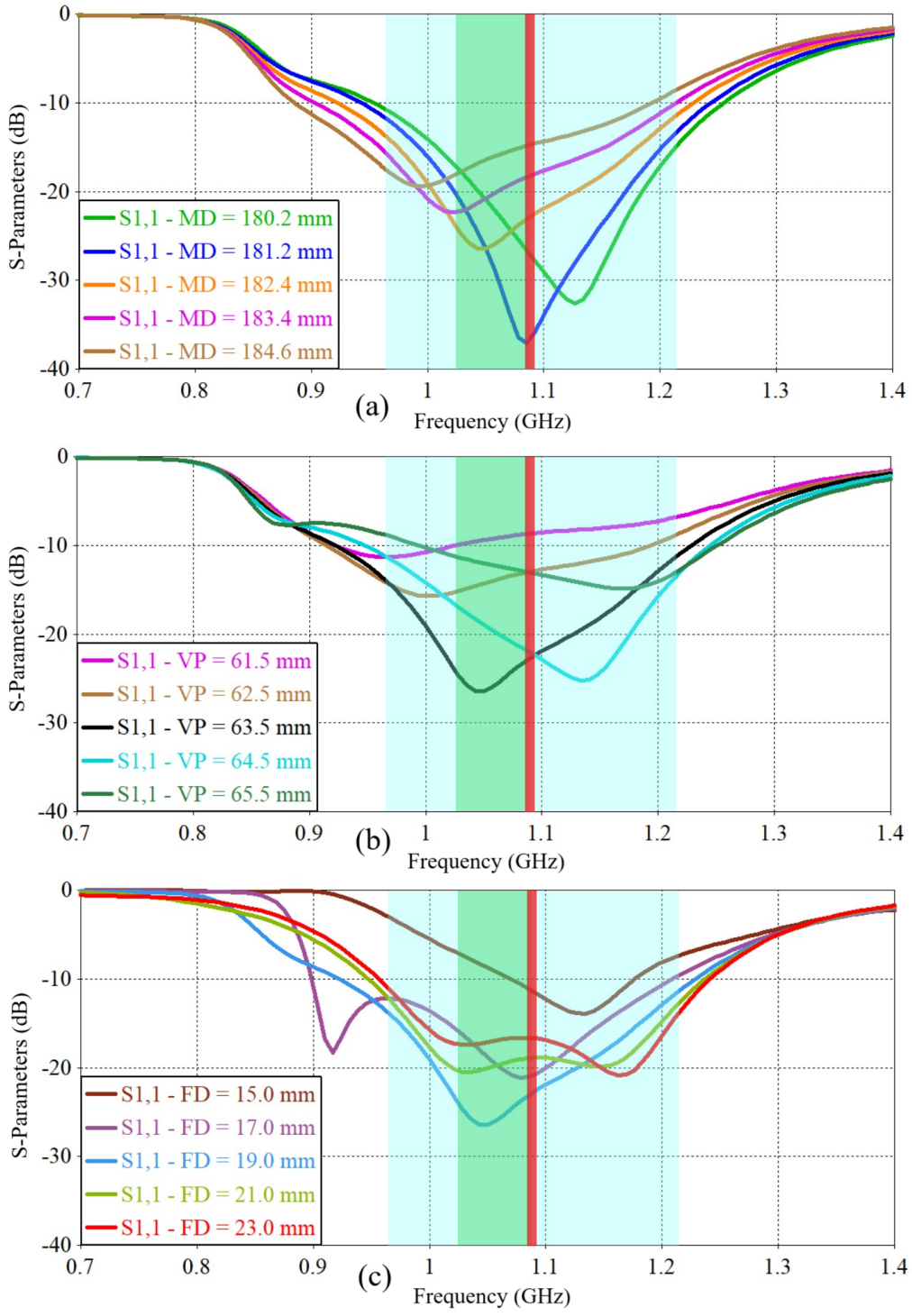

Figure 4.10 Simulated frequency response analysis for optimizing DME (blue shaded band), TCAS (green shaded band) and ADS-B (red shaded band) frequency bands in one-port antenna, (a) Diameter of top cavity patch MD on layer M6, (b) Cavity via placement radius from center VP, and (c) Diameter of the splitter outer ring FD on metallic layer M5.

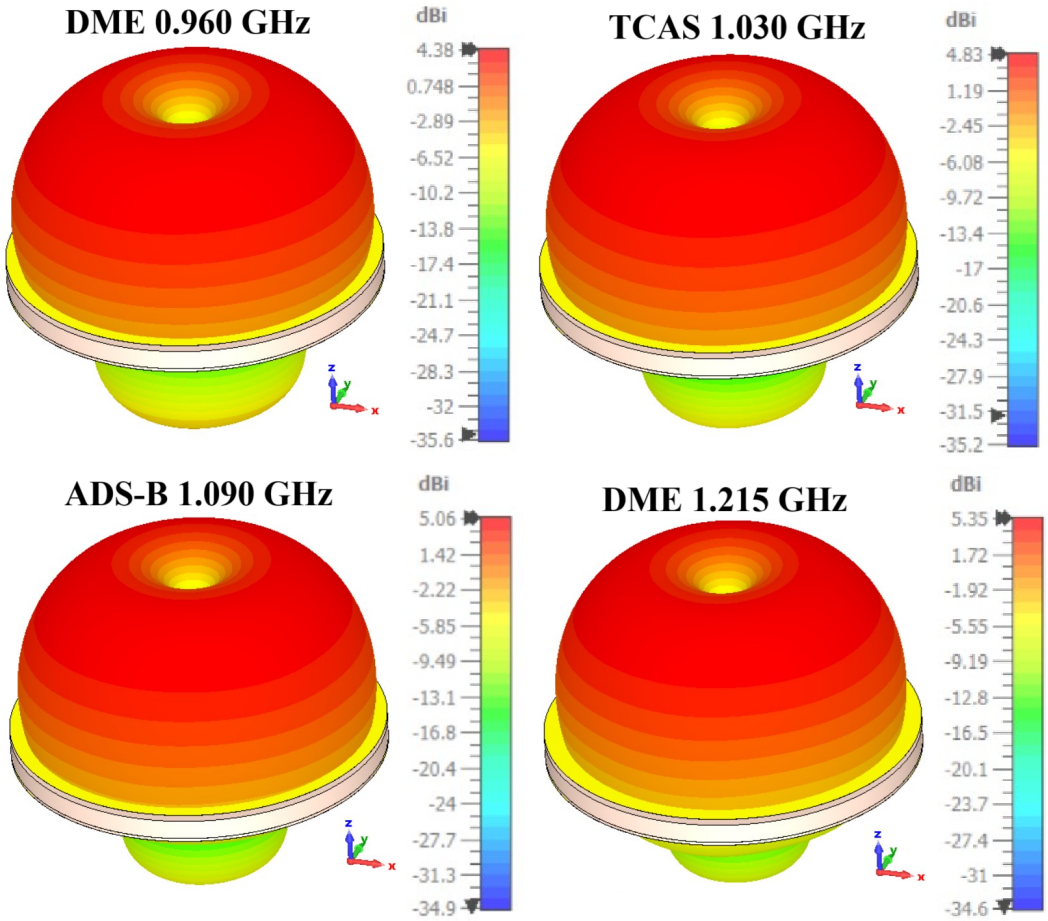

Figure 4.11 Simulated single port antenna omnidirectional 3D gain patterns for the DME, TCAS and ADS-B applications

4.6 Simulation and Measurements

Frequency responses, radiation patterns and surface currents are simulated, analyzed and measured for the proposed antennas. The frequency response parametric analysis for the optimization of the cavity parameters for achieving DME, TCAS and ADS-B desired frequency response of one-port antenna is shown in Figure 4.10. A deep resonance in the 1 GHz to 1.1 GHz range is produced in the cavity and its frequency shifts down as the patch diameter MD is increasing from 180.2 mm to 184.6 mm as shown in Figure 4.10(a). The second control parameter is VP, the radius of the circular fence of metallic vias vertically passing from metal layer M1 to M6.

The resonance shifts to higher frequency with the increase of VP, as shown in Figure 4.10(b). There is however a good stability of the response at the lower end of the band, near 900 MHz and below. Therefore, one could vary MD to set the lower end of the band and then vary

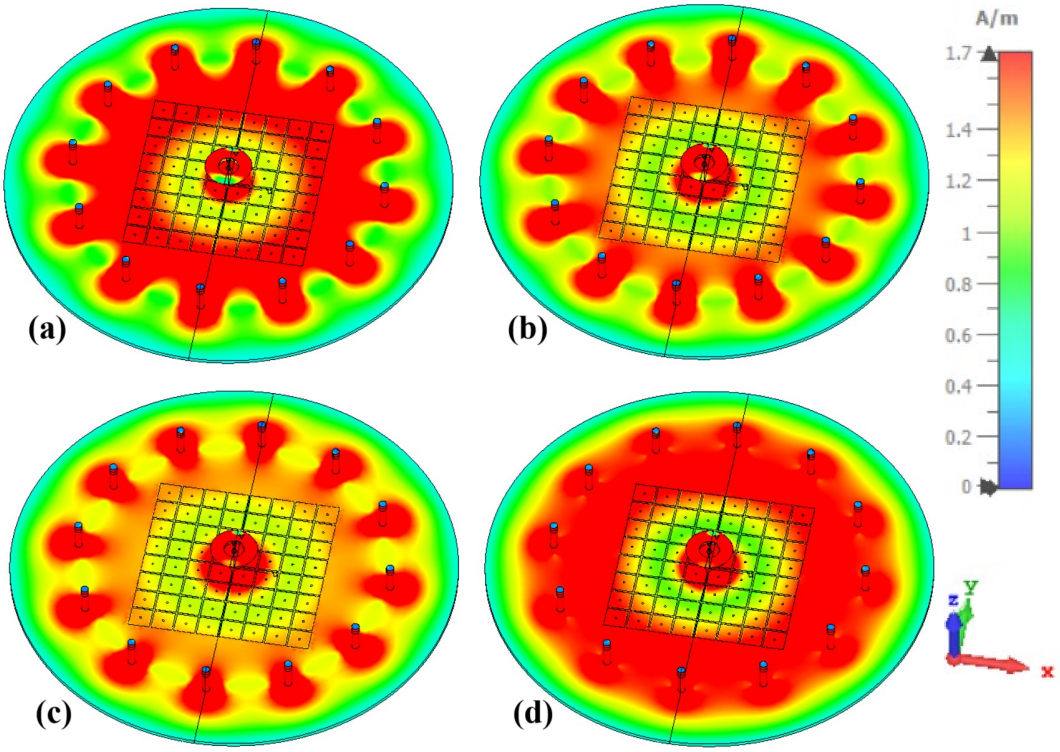

Figure 4.12 Proposed 1-port antenna maximum surface currents at (a) 0.96 GHz , (b) 1.030 GHz, (c) 1.090 GHz, (d) 1.215 GHz.

VP to adjust the higher end of the band. Finally, the splitter outer ring diameter FD can be varied to optimize the impedance matching and attaining the desired frequency bandwidth of the DME, TCAS and ADS-B bands as shown in Figure 4.10(c). Similar analysis can be performed for the optimization of the 2-port antenna cavity parameters.

Antenna radiation patterns were first simulated with the antenna sitting on a 40-cm diameter ground plane, as shown in Figure 4.11. For the 1-port antenna, TCAS gain of 4.83 dB at 1.03 GHz, ADS-B gain of 5.06 dB at 1.09 GHz and DME gain of 5.35 dB at 1.215 GHz were achieved. The surface currents of the DME circular cavity are simulated as shown in Figure 4.12 for 1-port antenna. Two modes of operation can be observed. At the three lower frequencies, ground currents have a 12-fold rotation symmetry and are diverted towards the vertical vias, whereas the presence of the vias cause only slight disturbance on the circular symmetry of the currents at the higher frequency as shown in Figure 4.12(d). This results in the increase in the overall bandwidth of the DME cavity. The EBG placed within the circular cavity demonstrate no effects on the surface currents at the frequency band of 0.96 GHz to 1.215 GHz as the EBG is designed for the currents suppression at 4.3 GHz.

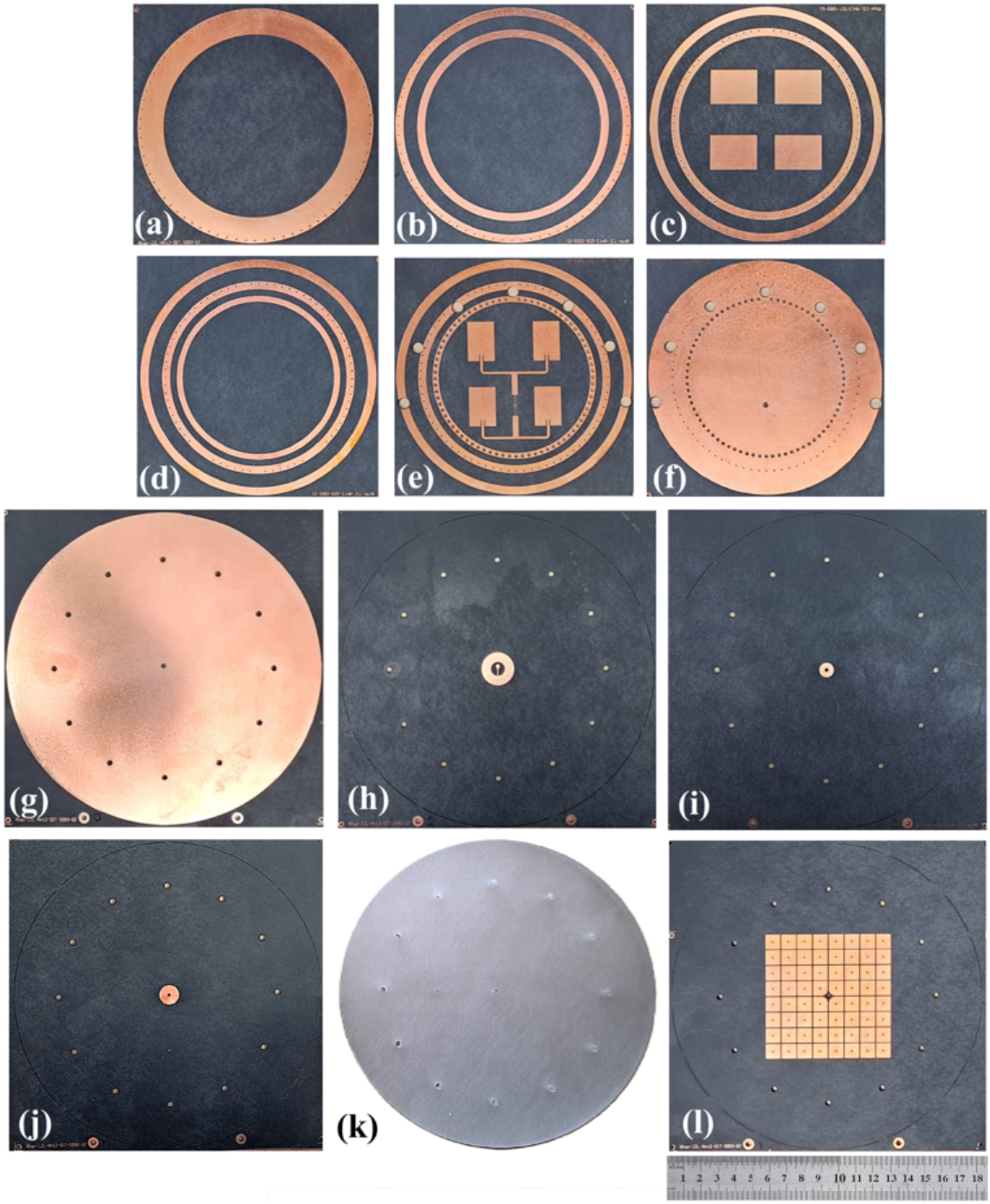

Figure 4.13 Proposed antenna fabricated layers, (a) Top ring M12 above substrate S7, (b) Connecting rings M11 below substrate S7, (c) Parasitic patches M10 above substrate S6, (d) Connecting rings M9 below substrate S6, (e) Patch array M8 above substrate S5, (f) RadAlt ground M7 below substrate S5, (g) Cavity top M6 above substrate S4, (h) Splitter M5 for 1-port antenna above substrate S3, (i) Splitter ground for 1-port antenna below substrate S3, (j) Feed patch for 2-port antenna above substrate S3, (k) Rexolite layer S2, and (l) EBG layer above substrate S1.

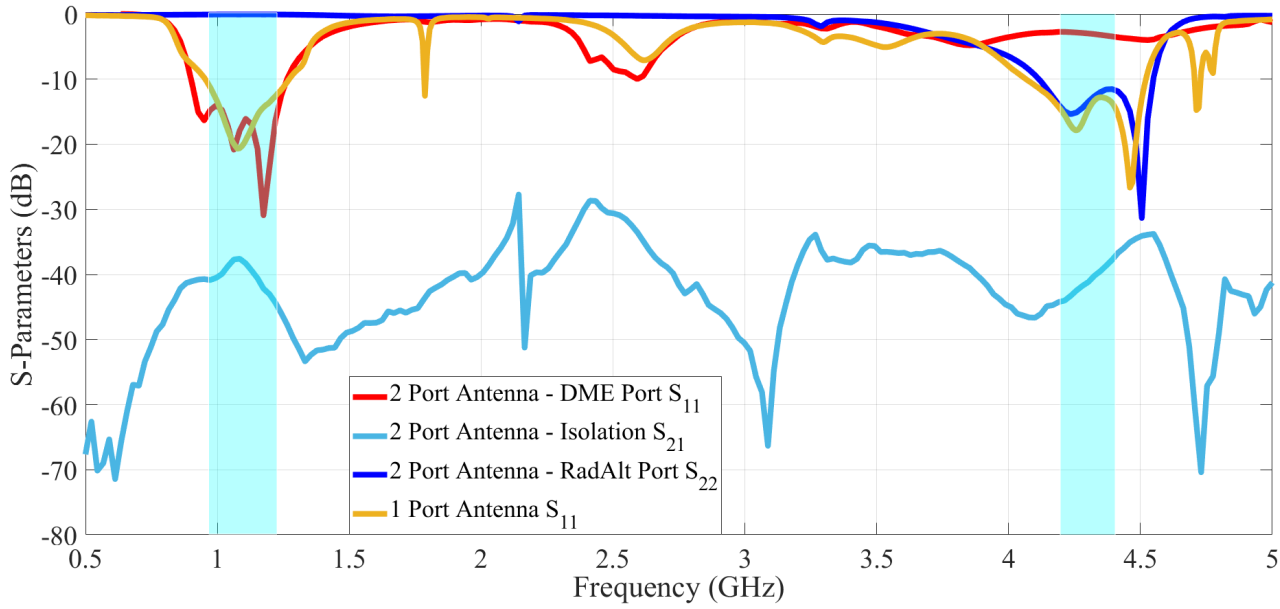

Figure 4.14 Measured frequency responses of the 1-port and 2-port proposed antennas. Required 10-dB return losses are shaded in blue.

The fabricated layers of the proposed 1-port and 2-port antennas are presented in Figure 4.13. The upper metallic layers from M7 to M12 for RadAlt applications are shown in Figure 4.13(a) to Figure 4.13(f) and are similar layers in both the 2-port and 1-port proposed antennas. The top metal layer M6 of the cavity in Figure 4.13(g) is connected with lower metal layer M7 as shown in Figure 4.13(f) and both layers are grounded with the lowest metal ground layer M1 of the 1-port and 2 port antennas through 12 vias. The measured frequency responses of the 2-port and 1-port proposed antennas are shown in Figure 4.14. The frequency responses of the DME are achieved with 10-dB return loss from 0.960 GHz to 1.215 GHz, TCAS 10-dB return loss from 1.03 GHz to 1.09 GHz, ADS-B response at 1.09 GHz and RadAlt response with 10-dB bandwidth from 4.2 GHz to 4.4 GHz. The measured frequency responses achieve the minimum operation performance specifications for both 1-port and 2-port proposed antennas as shown in the blue shaded bands in Figure 4.14. For the 2-port antenna, the isolation between the two ports in the band of interest is nearly 40 dB, similar to the simulated results shown in Figure 4.5. The radiation patterns of the proposed 1-port and 2-port antennas were measured in an anechoic chamber and are shown in Figure 4.15. The gain of the RadAlt is 12 dB with sidelobe levels of less than -40 dB throughout the band from 4.2 GHz to 4.4 GHz for both 2-port and 1-port antennas. The gain of the DME is measured 4.83 dB at 0.96 GHz and 5.89 dB at 1.215 GHz for the 1-port antenna. The non-symmetry of the L-band radiation pattern results of the 2-port antenna is due to

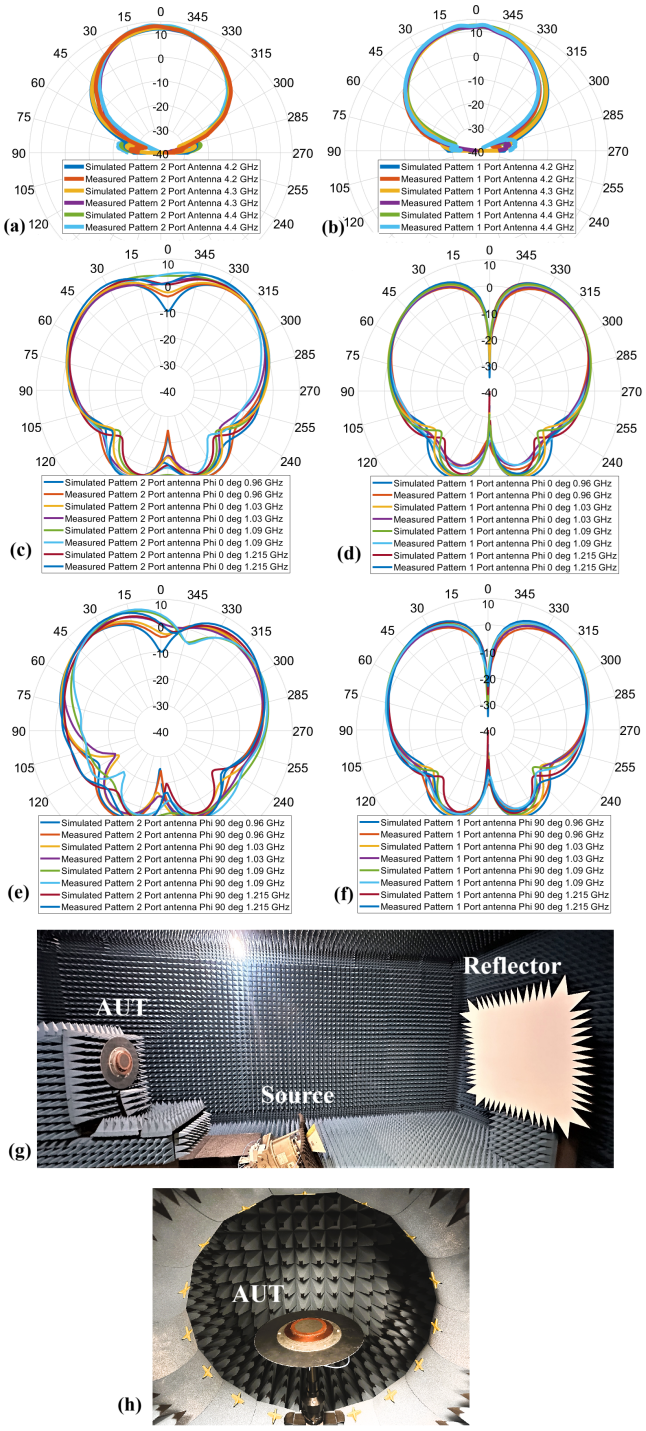

Figure 4.15 Measured and simulated 2D radiation patterns of proposed antennas; RadAlt Band (a) 2-port antenna, (b) 1-port antenna; DME, TCAS and ADS-B bands (c) 2-port antenna phi 0 degrees, (d) 1-port antenna phi 0 degrees, (e) 2-port antenna phi 90 degrees, (f) 1-port antenna phi 90 degrees, (g) Measurement setup in compact range chamber for RadAlt band, and (h) Measurement setup in Satimo starlab near-field system for DME, TCAS and ADS-B bands.

the offset configuration of the RadAlt feed with respect to the center of the cavity.

4.7 Conclusion

Two multiband low-profile antennas are designed and fabricated for avionics application. The objective is merging of the multiple avionics systems using software defined avionics radios and the realized antennas are steps towards this objective. The lower frequency band is achieved from 0.942 GHz to 1.217 GHz with omnidirectional radiation patterns for the DME, TCAS and ADS-B applications. A three-dimensional power splitter is designed for single-feed antenna for both lower cavity and RadAlt patch array. Currents suppression within the cavity at 4.3 GHz is achieved by implementing an EBG within the cavity for the revival of the RadAlt frequency and radiation characteristics. The higher frequency band of 4.1 GHz to 4.5 GHz is achieved with directional radiation pattern and gain of 12 dB and sidelobe levels of less than -40 dB.

CHAPTER 5 LOW PROFILE INSTRUMENT LANDING SYSTEM BOWTIE ANTENNA

5.1 Introduction

Instrument Landing Systems (ILS) comprises three systems of Glideslope, Localizer and Marker and they are used for guiding the aircraft in the landing. The ILS marker system informs the aircraft of its distance from the runaway and the marker antenna operates on the ILS marker frequency band of 74.75 MHz to 75.25 MHz with horizontal polarization. The ILS glideslope system guides the aircraft vertically and ILS localizer systems guides the aircraft laterally for landing along the glidepath. The ILS glideslope and localizer antennas are mounted on the nose of the aircraft and both the ILS glideslope and localizer antennas are horizontally polarized antennas. The ILS localizer antenna is designed for the frequency band of 108 MHz to 112 MHz with VSWR of 6:1 [7] and gain of 0 dB to 2 dB [71]. The ILS glideslope antenna is designed for frequency band of 329 MHz to 335 MHz with VSWR of 6:1 [8] and gain of 0 dB to 2 dB [71].

Aircrafts are currently using loop antennas for the glideslope instrument landing systems [71]. These glideslope loop antennas have certain heights and can be as high as 175 mm [72].

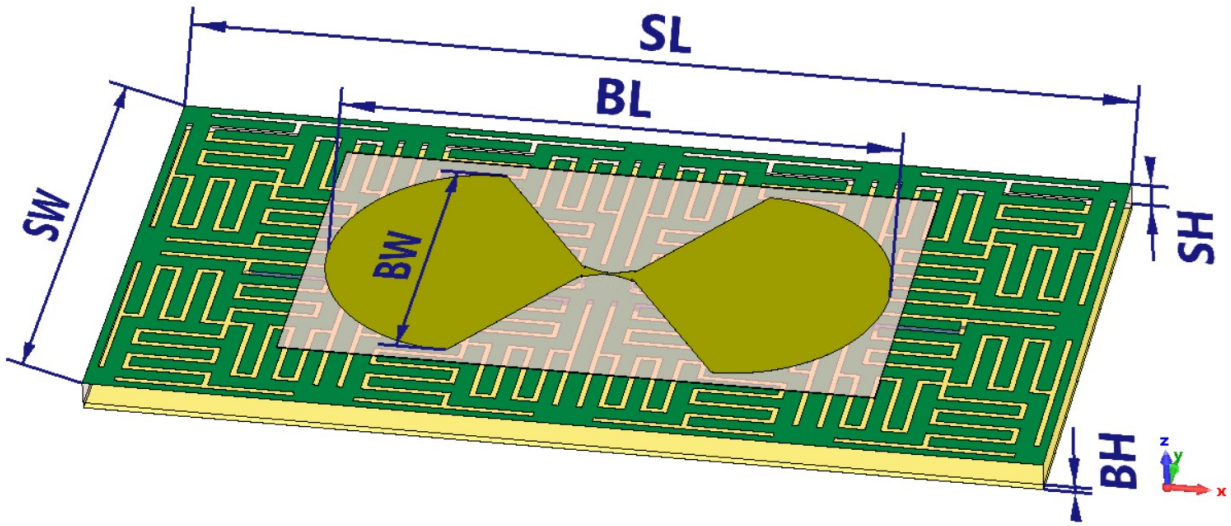

Figure 5.1 Proposed low profile IDC EBG bowtie antenna with dimensions, BL = 302.00 mm, BW = 160.00 mm, SL = 512.96 mm, SW = 256.48 mm, BH = 3.15 mm and SH = 12.60 mm.

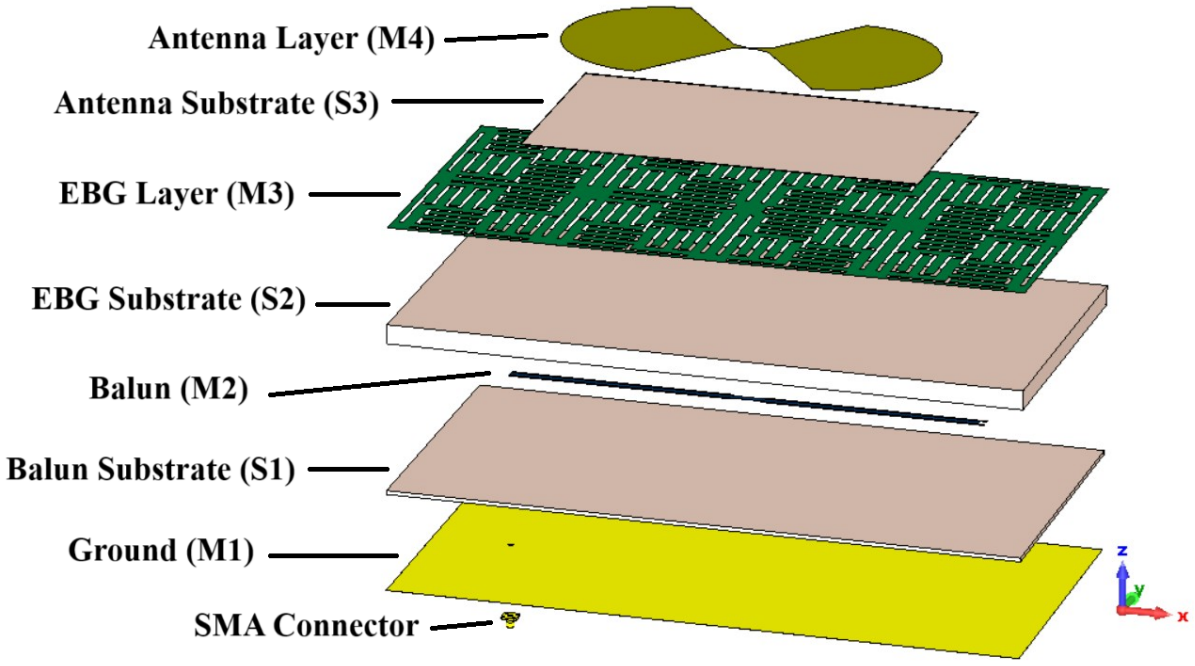

Figure 5.2 Proposed IDC EBG bowtie antenna layers details.

Our research objective is to design glideslope ILS antenna that is low profile and can be conformally placed along the airframe of the aircraft. Horizontal placement of antenna close to the large metal ground plane causes impedance mismatch due to ground reflections and electromagnetic bandgap structures can be used for in-phase currents and revival of radiation characteristics [33]. In this chapter, a printed low profile electromagnetic bandgap (EBG) bowtie antenna is presented for the ILS glideslope applications. The proposed antenna is designed with a printed bowtie radiating structure that is more compact in terms of the overall length of the radiating segments as compared to the printed dipole antenna and improves the bandwidth [73]. The proposed antenna is placed on metal ground plane for low profile configuration. An Interdigital capacitor (IDC) EBG is designed and placed in between the antenna and ground plane for providing the reinforcement in the currents and revival of the radiation characteristics of the proposed antenna placed on the metal ground plane. A printed grounded coplanar waveguide balun is designed for feeding the two arms of the proposed printed bowtie antenna. The proposed antenna is placed on large and conformal surfaces for verification of its radiation characteristics. The proposed antenna is also placed along the surface of the aircraft under the nose and the directional radiation characteristics are simulated and analyzed.

5.2 Bowtie Antenna Design

The proposed antenna for aircraft ILS glideslope applications is shown in Figure 5.1. The detailed layers of the proposed antenna is shown in Figure 5.2. The low profile antenna is designed with bowtie radiating element that is printed on the metal layer M4 placed on top of the substrate layer S3. The radiating element comprises two arms of bowtie configuration

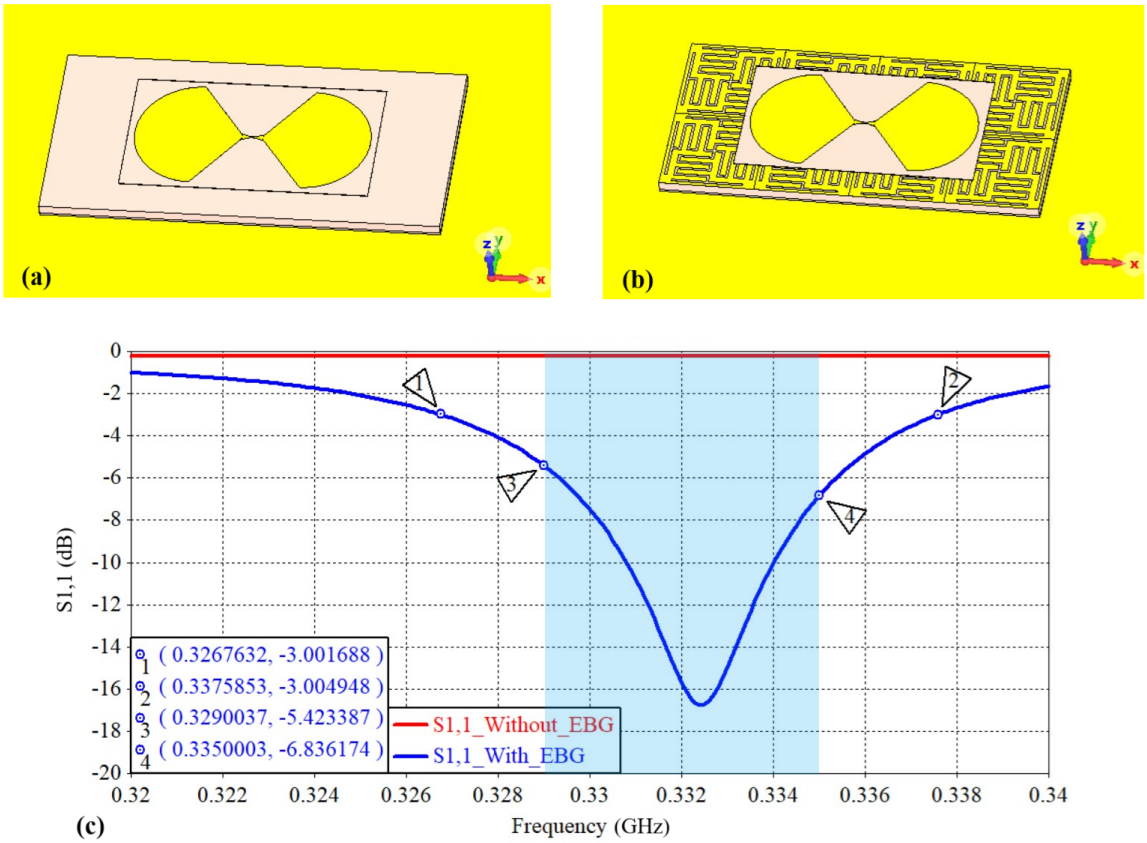

Figure 5.3 Proposed antenna on metal ground (a) Without EBG, (b) With IDC EBG, and (c) Simulated frequency response of proposed antenna, with and without IDC EBG

as shown in Figure 5.2. The designed antenna is placed on the metal EBG layer M3 and there is a air separation of 5.6 mm between the layers S3 and M3. The EBG is designed using an Interdigital Capacitor structure for compact size and 8 cells are used with 4 x 2 configuration. The printed copper EBG layer M3 is designed and placed on top of the substrate layer S2 with height of 12.6 mm and dielectric constant of 2.2. The feeding balun line is designed on metal layer M2 and placed on top of the substrate layer S1 with height of 3.15 mm. The balun line is used for feeding the two arms of the bowtie antenna. The balun substrate S1 is placed on top of the metal ground plane M1 as shown in Figure 5.2. All the substrate

layers are designed on Rogers 5880 substrate with dielectric constant of 2.2 and loss tangent of 0.0009.

The initial design step is the placement of the printed bowtie layer M4 on metal ground plane M1. Substrate layer with thickness of 15.75 mm in placed in between the two metal layers M1 and M4 as shown in Figure 5.3(a). This placement of the bowtie antenna on ground plane causes an impedance mismatch due to ground reflections. The frequency response of the bowtie antenna placed on the 2.3 x 2.3 meters metal ground plane is shown in Figure 5.3(c) red curve. The frequency response of the proposed antenna is revived by designing IDC

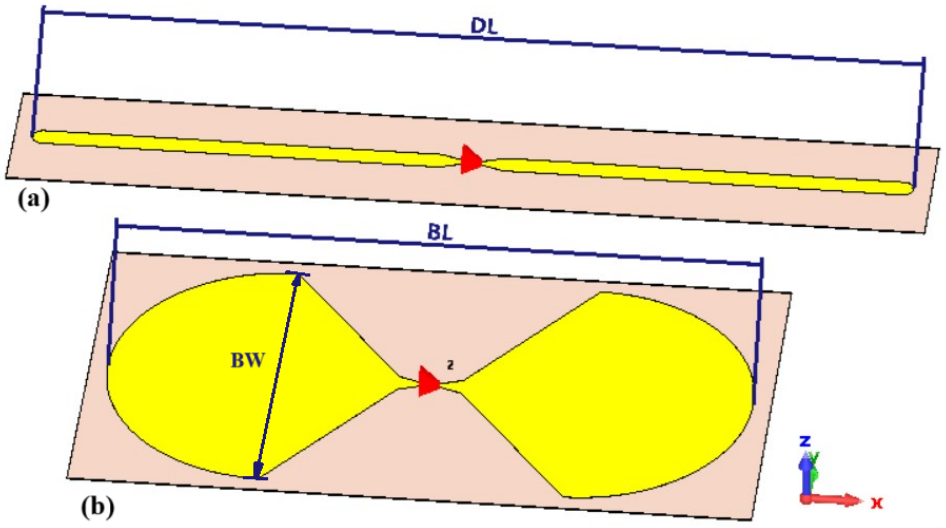

Figure 5.4 Proposed antenna design (a) Dipole antenna, (b) Bowtie antenna.

EBG layer and placing the antenna on top of the EBG layer instead of directly placing the antenna on the metal ground plane as shown in Figure 5.3 (b). The frequency response of the proposed antenna with EBG is shown in Figure 5.3(c) blue curve. The antenna is optimized for frequency response from 0.329 GHz with return loss of 5.42 dB to 0.335 GHz with 6.83 dB and meets the VSWR requirement of 6:1 ratio for the Instrument Landing System Glideslope application according to the Minimum Operational Performance Standards (MOPS) [8]. The operational bandwidth of the proposed antenna is from 0.326 GHz to 0.337 GHz with the VSWR of 6:1. The VSWR level of 6:1 corresponds to a return loss of 2.92 dB.

The designs of both printed bowtie and dipole antennas are presented here for demonstrating the length reduction benefit of the bowtie antenna in comparison to dipole antenna. The printed dipole antenna is designed for the ILS glideslope application on substrate with height of 0.508 mm without the EBG and ground plane layers, as shown in Figure 5.4(a). The printed dipole antenna comprises two microstrip arms and is fed at the center with total

length of DL as shown in Figure 5.4(a). The printed dipole antenna is designed for covering the ILS glideslope frequency band from 0.329 GHz to 0.335 GHz and the dipole length DL is optimized for covering the operational band as shown in Figure 5.5. The printed dipole antenna is optimized for operating at the center frequency of 0.340 GHz with the dipole length of 392 mm. The resonant operational frequency of the dipole antenna can be shifted down at 0.3 GHz by increasing the length of the dipole antenna to 440 mm as shown in Figure 5.5.

Both the dipole and bowtie antennas are fed with direct port in the simulations without using balun as shown in the Figure 5.4.

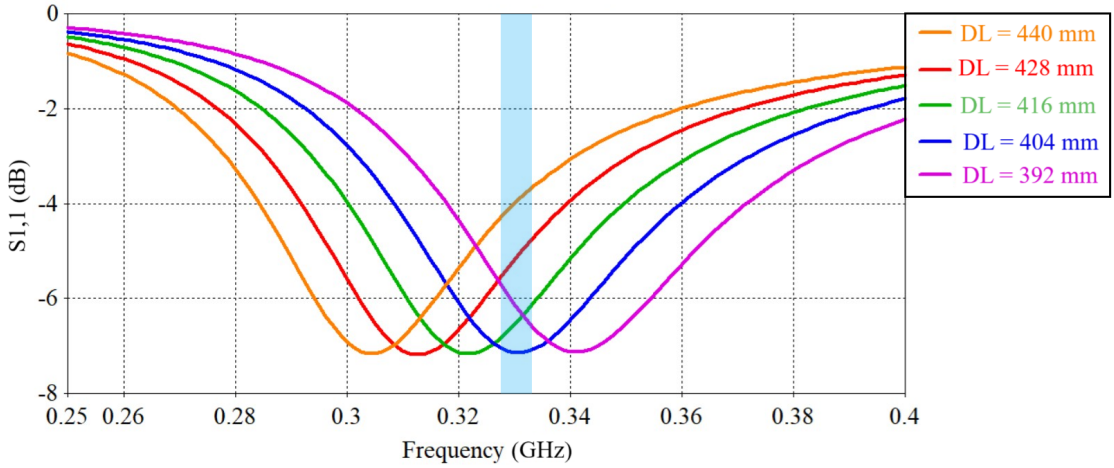

Figure 5.5 Simulated frequency response analysis of dipole antenna length.

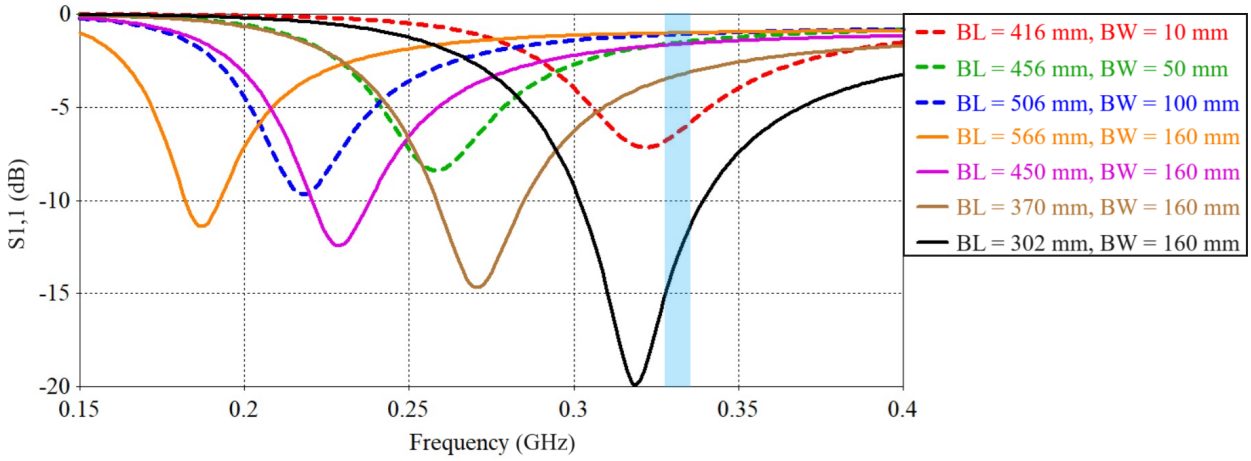

Figure 5.6 Simulated frequency response analysis of proposed bowtie antenna length and width.

The printed bowtie antenna is designed on substrate with height of 0.508 mm without EBG and ground plane layers as shown in Figure 5.4(b). The antenna comprises two arms and is fed in the center. Each radiating arm consists of flared section of bowtie shape with width of BW and the end of each arm is rounded, with total length of the antenna BL, as shown in Figure 5.4(b). The proposed printed bowtie antenna has benefits of reduced length and increased bandwidth as demonstrated in the frequency response analysis in Figure 5.6. In the initial design, the dipole antenna has frequency response centered at 0.321 GHz with length of DL = 416 mm as shown in the frequency response in red curve in Figure 5.6.

This length is taken as the initial parameter for designing bowtie antenna and the initial length of the bowtie is selected as BL = 416 mm and width of the bowtie is selected as the same width as that of dipole with BW = 10 mm, as shown in the frequency response of the red curve in Figure 5.6. With the increase in the width of the bowtie antenna from BW 10 mm to 50 mm, the length of the bowtie antenna also increase from 416 mm to 456 mm for maintaining the shape at the end of the antenna arms.

The frequency response decreases from 0.321 GHz to 0.257 GHz due to the increase in the length of the bowtie antenna from 416 mm to 456 mm and has an advantage of improved return loss from -7.15 dB to -8.39 dB respectively, as shown in the green curve in Figure 5.6. The return loss of the bowtie antenna further improves from -9.65 dB to -11.39 dB as the width of the bowtie antenna is increased from 100 mm to 160 mm as shown in the blue and orange curves respectively in Figure 5.6. As the length of the bowtie is also increased from 506 mm to 566 mm, the frequency response of the proposed antenna is shifted down from 0.217 GHz to 0.186 GHz as shown in the blue and orange curves respectively in Figure 5.6.

In the next step of the design, the length BL of the bowtie antenna is decreased while width BW is kept constant at 160 mm, for shifting back the frequency response of the bowtie antenna from the lower frequency centered at 0.186 GHz (orange curve in Figure 5.6), to the upper required frequency band of the ILS glideslope from 0.329 GHz to 0.335 GHz. The length of the bowtie antenna BL is decreased from 566 mm to 450 mm and the frequency response is shifted from 0.186 GHz with return loss of -11.39 dB to 0.228 GHz with improved return loss of -12.42 dB as shown in the orange and purple curves respectively in Figure 5.6. The length BL of the bowtie antenna is further decreased from 370 mm to 302 mm while keeping the same width BW = 160 mm, and the frequency response is shifted upwards from 0.270 GHz to 0.318 GHz with 10 dB impedance bandwidth from 0.301 GHz to 0.338 GHz as shown from the brown and black curves respectively in Figure 5.6. The optimized frequency response includes the required frequency band of the ILS glideslope from 0.329

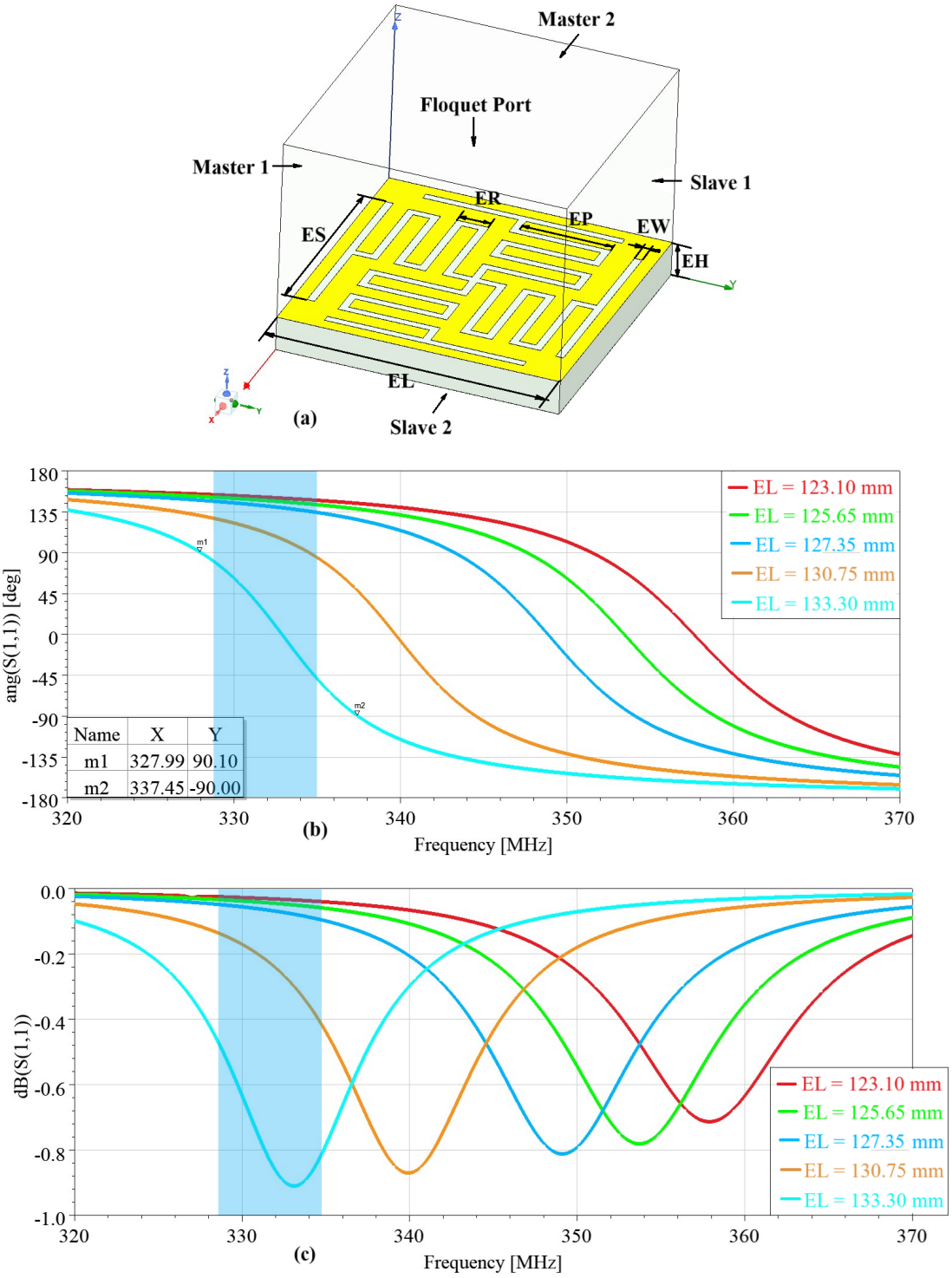

Figure 5.7 Interdigital Capacitor EBG design and analysis (a) Unit cell design and dimensions, EL = 133.30 mm, EW = 3.50 mm, ES = 93.60 mm, ER = 14.8 mm, EH = 15.75 mm and EP = 43.3 mm, (b) Simulated reflection phase analysis, (c) Simulated reflection magnitude analysis.

GHz to 0.335 GHz (blue shaded band), as shown in the black curve in Figure 5.6.

5.3 Unit Cell EBG Design and Analysis

5.3.1 Interdigital EBG

The proposed printed bowtie antenna is placed on metal surface and the frequency response is shown in Figure 5.3 red curve with poor return loss. This frequency response is due to the out of phase image current on the metal ground plane that cancels the in phase currents on the horizontally placed printed bowtie antenna on the metal surface. Changing the phase of the image current requires a magnetic conductor. In practice this can be realized with an artificial magnetic conductor (AMC) implemented with a periodic structure. Many EBGs have been proposed to realize the AMC, such as the well known uniplanar compact EBG [34]. In this work, we use a more compact version of that cell in which meander lines are used to realize longer inductive paths and therefore reduce the AMC operational frequency, for a fixed unit cell size [35]. This meander structure can also be seen as an interdigital capacitor. Interdigital Capacitor structured electromagnetic bandgap is designed and placed between the horizontally placed bowtie antenna and metal ground plane. The IDC EBG surface reinforces the currents as the image currents on the designed EBG are in phase.

The designed IDC EBG is shown in Figure 5.7(a) and the reflection phase diagram is shown in Figure 5.7(b). The IDC structure is designed for EBG as it is a compact structure. The structure comprises top metal layer with interdigital slotted lines that is placed on substrate with height of 15.75 mm and dielectric constant of 2.2, and its bottom layer is metal layer. Ansys-HFSS simulator is used for designing and analyzing the results of the IDC EBG unit cell. Floquet port is used as the excitation port and is applied parallel to xy plane along the z axis direction at z = 100 mm. The excitation port is de-embedded to the surface of the EBG at z = 15.82 mm. Master 1 and Slave 1 walls are implemented along the y direction at y = 0 and y = EL respectively, as shown in Figure 5.7 (a). Master 2 and Slave 2 walls are implemented along the x direction at x = 0 and x = EL respectively, as shown in Figure 5.7 (b).

The length of the IDC EBG EL is optimized for reinforcing the antenna currents and reviving the return loss of the proposed antenna placed on metal ground M1. The EBG length EL is optimized for the ILS frequency band from 0.329 GHz to 0.335 GHz (blue shaded band) as shown in Figure 5.7(b). The magnitude of the EBG surface impedance increases as compared to the impedance of the free space impedance within the reflection phase range from -90 degrees to 90 degrees, and in this phase range the antenna currents can be reinforced [33].

5.3.2 Multilayered 1D EBG: Addendum to Chapter 3

In Chapter 3, an EBG was designed for the currents suppression and sidelobe level reduction of the patch array for radio altimeter applications in the whole frequency band of operation from 4.2 GHz to 4.4 GHz. Chapter 3 was presented in a "journal paper format". Due to limited page count in the journal, the paper did not include justifications for the choice of the various parameters defining the 1D unit cell. These details are included in this section as a complement of information. A novel multilayered structure was proposed for designing the EBG for broadband currents suppression, instead of conventional single layered EBG. The EBG was designed with mushroom structures in three layers and were formed with top loaded vertical posts that creates a layered high impedance boundary surrounding the antenna.

The design evolution phases of the proposed EBG are shown in Figure 5.8. In the first design phase, a single layered high impedance boundary comprising metallic via elements with parasitic metallic ring were circularly placed around the radiating elements as shown in Figure 5.8(a) and in the zoomed view in Figure 5.8(b). The currents suppression and side lobe level reduction of less than -40 dB due to single layer EBG in phase 1 was very narrow band. In the second and third phase of the EBG design, two and three layered EBG was designed as shown in Figure 5.8(c) to 5.8(f), respectively. The two and three layered EBG designs were proposed for achieving lower sidelobe levels for a wideband antenna, that consists of two layered patch arrays. The sidelobe level of less than - 40 dB was achieved on a wider band as compared to single layer EBG, but the sidelobe level criteria was still not achieved for the whole radio frequency band from 4.2 GHz to 4.3 GHz. In the fourth design phase, the EBG is designed with three layers and the rings placement and overlapping coupling area of the second and third layers were optimized for achieving currents suppression and sidelobe level of less than -40 dB from 4.2 GHz to 4.4 GHz. The details of the unit cell analysis and optimization of the proposed EBG, for achieving currents suppression in the radio altimeter frequency band from 4.2 GHz to 4.4 GHz is presented in the section 3.4 of chapter 3.

The detailed unit cell structure of the proposed EBG is shown in Figure 3.3. The lengths of the top patches RL1 and RL2 were selected to be 3 mm and is more than the diameter of vias RV that were selected as 2 mm. The diameter of the vias is selected to be more than the height of the substrate SH that is 1.575 mm. These dimensions of the patch lengths and vias were selected as per the requirements of the fabrication process and via hole platting. The length of the top layered patch RL3 was optimized in HFSS for optimal coupling between the top patches of second and third EBG layers for achieving broadband EGB response and currents suppression. The parametric analysis of the patch length RL3 and vias diameter

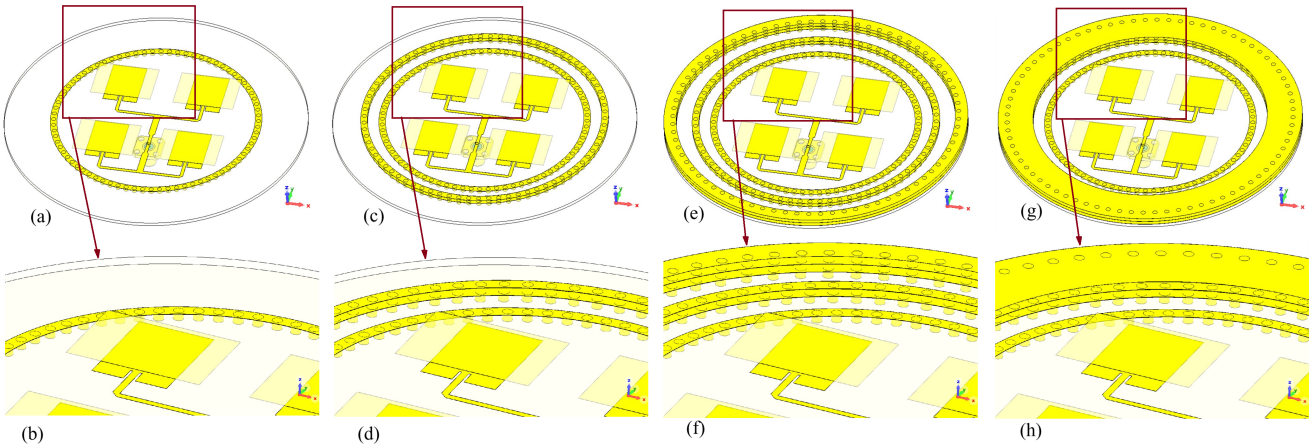

Figure 5.8 Multilayered 1D EBG design phases, (a) Phase 1, one layered EBG, (b) Zoomed view phase 1 design, (c) Phase 2, two layered EBG, (d) Zoomed view phase 2 design, (e) Phase 3, three layered EBG, (f) Zoomed view phase 3 design, (g) Phase 4, three layered EBG with coupling rings, and (h) Zoomed view phase 4 design.

RV for optimizing the frequency response of the proposed EBG is shown in Figures 3.4 and 3.5 respectively.

5.4 Coplanar Waveguide Balun Feed Design

Balun feed is designed for providing impedance matching feeding between the unbalanced coaxial transmission line and balanced bowtie antenna. The schematic [39] of the designed Marchand balun is shown in Figure 5.9(a). The balun comprises one inner segment and two grounded segments of quarter wavelength lengths feeding the two arms of the bowtie antenna. As seen in Figure 5.9(a), the balance port terminals of the Marchand balun are connected to the ground conductor of the transmission lines. To realize this while avoiding extra metal layer and keeping the structure more compact, we have designed the balun with printed grounded coplanar waveguided (CPWG) configuration as shown in Figure 5.9(b) to Figure 5.9(g). In all these figures, we have made the front four EBG cells transparent for clarity reasons. In practice, the whole balun structure is built underneath the EBG layer. Only the vertical vias connecting the balanced terminals of the bowtie antenna arms protrude through circular holes etched in the EBG layer as shown in Figure 5.9(f). The printed CPWG is designed and placed in the metallic layer M2 (blue color) above the ground metal layer M1 (yellow color) as shown in Figure 5.9(b) and Figure 5.9(c). Substrate S1 is placed in between the metal layers M1 and M2 as previously shown in Figure 5.2 layers diagram. The inner line segment of the coplanar waveguide feed is connector with the inner pin of the sma connector

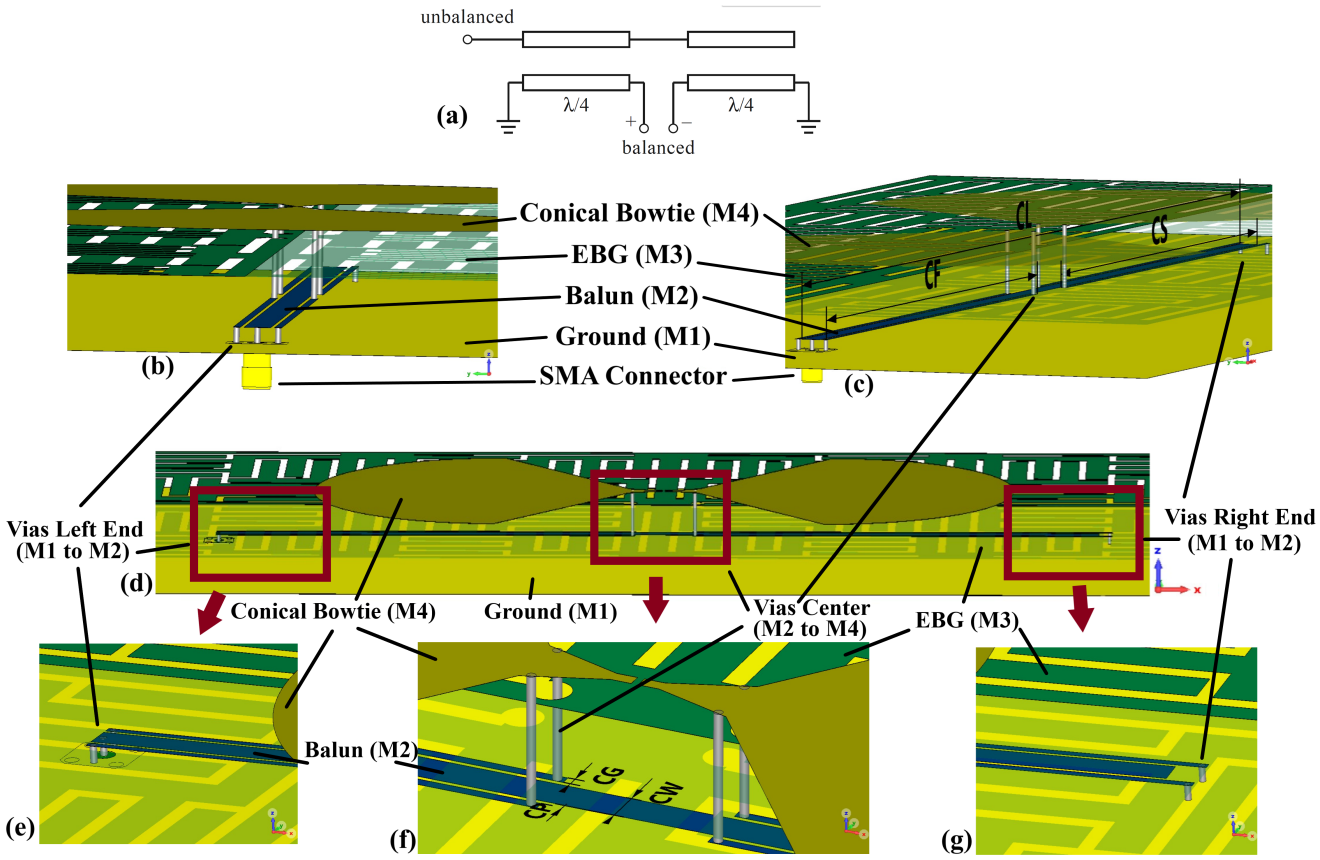

Figure 5.9 Proposed antenna CPWG balun feed design details, (a) Marchand balun schematic [39], (b) Labeled side view, (c) Dimensions view, CF = 181.15 mm, CL = 381.15 mm, CS = 175.27 mm, (d) Front view, (e) Feed balun zoomed left end section details, (f) Feed balun zoomed center section details and dimensions, CP = 0.75 mm, CG = 1.5 mm, CW = 5.5 mm, (g) Feed balun zoomed right end section details.

as shown in side view diagram of the antenna in Figure 5.9 (b). The outer line segments of the coplanar waveguide are grounded by connecting the ends of the outer line segments in layer M2 to ground M1 through vias as shown in Figure 5.9(b). The outer segment lines of the coplanar waveguide are designed with the lengths CF of quarter wavelength and the inner ends of these segments are fed with vias from metal layer M2 to the two arms of the bowtie at the center at metal layer M4 as shown in the Figure 5.9 (b) and Figure 5.9 (c).

The details of the grounded coplanar waveguide balun are shown in the front view of the proposed antenna in Figure 5.9 (d) and the zoomed in images for the details of the three sections of CPWG balun left end, center and right end sections are shown in Figure 5.9(e), Figure 5.9(f) and Figure 5.9(g) respectively. The zoomed image of the left end of the balun in Figure 5.9(e), shows the outer segments of the coplanar waveguide are grounded from M2

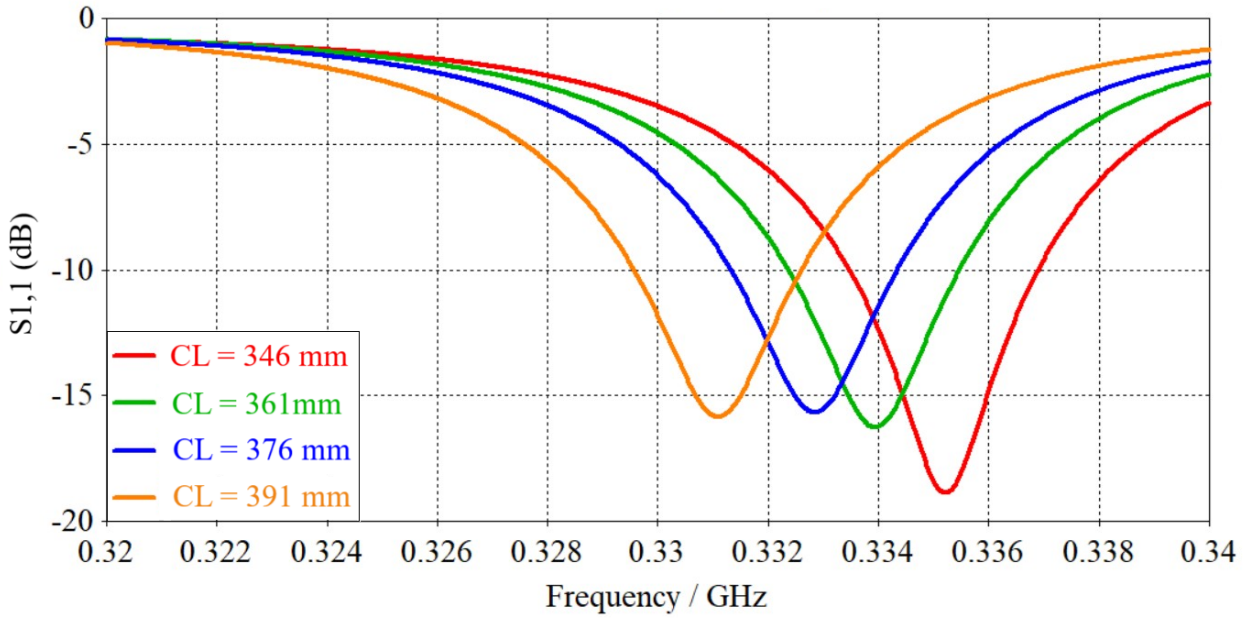

Figure 5.10 Proposed antenna CPWG balun feed length CL analysis.

to M1 and inner segment is connected to the coaxial sma connector balun.

The zoomed center section of the balun in Figure 5.9 (f), shows via connections of the outer four segments of the coplanar waveguide balun from metal layer M2 to the two arms of the bowtie radiators in the metal layer M4. The via connections do not connect with the EBG metal layer M3 as shown in the Figure 5.9(f). The widths of the inner and outer line segments as well as the gap between the inner and outer line segments of the coplanar waveguide balun are optimized for the matching of the proposed antenna. The zoomed right end section in Figure 5.9(g), shows the grounded ends of the outer line segments of the coplanar waveguide balun with vias from balun metal layer M2 to ground metal layer M1 and the inner line segment end is not shorted with the ground. The inner line segment length CL of the balun is optimized for the required ILS glideslope frequency band as shown in Figure 5.10. As the length of the inner line CL is increased from 346 mm to 391 mm, the frequency response of the bowtie antenna shifts downwards with center frequency its from 0.335 GHz (red color curve) to 0.331 GHz (orange color curve) as shown in Figure 5.10.

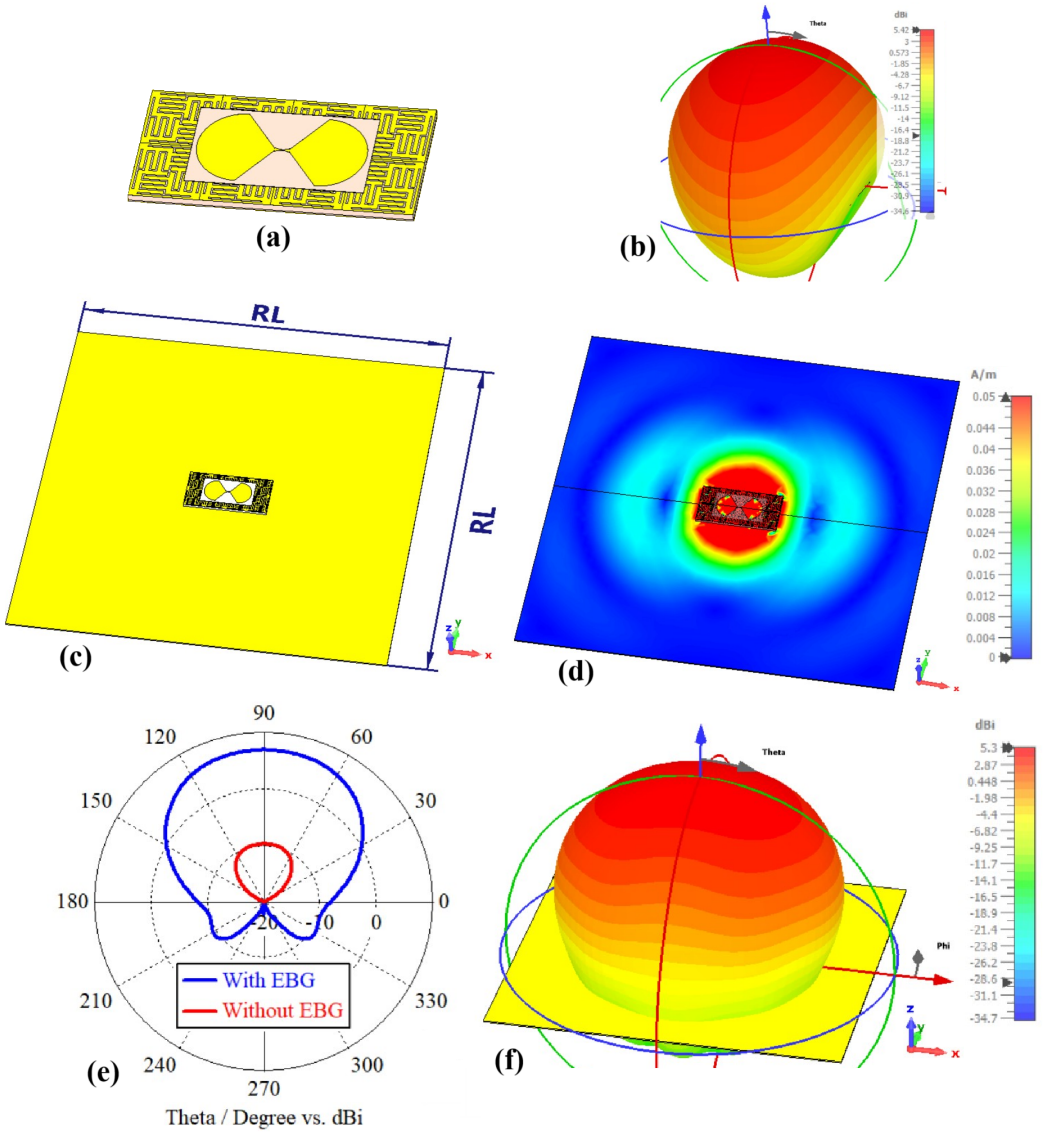

Figure 5.11 Proposed antenna large metallic surface placement and simulated results (a) Proposed antenna, (b) Antenna 3D gain plot without large ground plane at 0.335 GHz, (c) Placement on large metal surface with length and width of RL = 2.3 meters, (d) Surface currents at 0.335 GHz, (e) 2D radiation patterns with and without IDC EBG on large ground plane, and (f) 3D gain plot on large ground plane at 0.335 GHz.

5.5 Antenna Analysis on Large Metal Surface

When installed on the aircraft, the IDC EBG bowtie antenna will operate on a large metal surface as shown in the frequency response graph of Figure 5.3(c). The proposed antenna resonates in the ILS frequency band from 0.329 GHz to 0.335 GHz with IDC EBG for 2.3 x 2.3 meters large ground plane as shown in Figure 5.3(c) blue curve. Large metal ground

of 2.3 x 23. meters is used for radiation pattern analysis as the front aircraft nose section has similar diameter of 2.3 meters, as shown in Figure 5.14(c). The radiation pattern of the proposed antenna is simulated and analyzed on both with and without 2.3 x 2.3 meters large ground plane. The proposed antenna without the large metal ground plane is shown in Figure 5.11(a). The simulated directional radiation pattern of the proposed antenna without the ground plane is shown in Figure 5.11(b) with peak gain of 5.4 dB at 0.335 GHz. In the next step the proposed antenna is placed on large metal ground plane with both length and width of RL = 2.3 meters for verifying the radiation pattern characteristics of the proposed antenna as shown in Figure 5.11(c). The surface currents of the proposed antenna is shown in Figure 5.11(d) and the 2D radiation pattern plot of the proposed antenna on large metal flat ground plane with and without the IDC EBG is shown in Figure 5.11(e). The peak gain of the proposed antenna without the IDC EGB is - 9.79 dB and the gain of the antenna with IDC EBG is 5.3 dB at 0.335 GHz, with directional radiation pattern as shown in Figure 5.11(e). The 3D gain plot of the proposed antenna with IDC EBG on large metal ground plane is shown in Figure 5.11(f) with directional radiation pattern.

5.6 Antenna Analysis on Conformal and Aircraft Metal Surface

Aircraft antenna fuselages are cylindrical, and therefore, it is important to validate the performance of the antenna mounted on the curved ground planes. The proposed IDC EBG bowtie antenna is placed on a conformal large curved metal plane and its radiation characteristics are simulated and analyzed. The placement of the proposed antenna on the conformal surface is shown in Figure 5.12(a), and the side view of the placed antenna on the conformal surface is shown in Figure 5.12(b). The 3D gain plot of the proposed antenna placed on the conformal metal sheet is shown in Figure 5.12(c), and the proposed antenna has directional radiation pattern similar to the 3D gain pattern of the proposed antenna placed on the large metal plane shown in Figure 5.11(f). The simulations for the curved ground plane are done without balun and direct feed excitation port is applied at the center of the two arms of the bowtie antenna for simulation simplifications. The gain is slightly decreased to 2.92 dB at 0.335 GHz as compared to the gain of 3.21 dB at 0.335 GHz for the antenna placed on straight large ground plane of 2.3 x 2.3 meters without balun. The surface current plot of the proposed antenna on curved surface at 0.335 GHz is shown in Figure 5.12(d).

In the next step the proposed antenna is placed on a more curved cylindrical surface as shown in Figure 5.13(a) and Figure 5.13(b) and the simulated surface current and 3D gain plots are shown in Figure 5.13(c) and Figure 5.13(d) respectively. The simulation is done without balun and direct feed port excitation. The 3D gain plot is similar to the directional

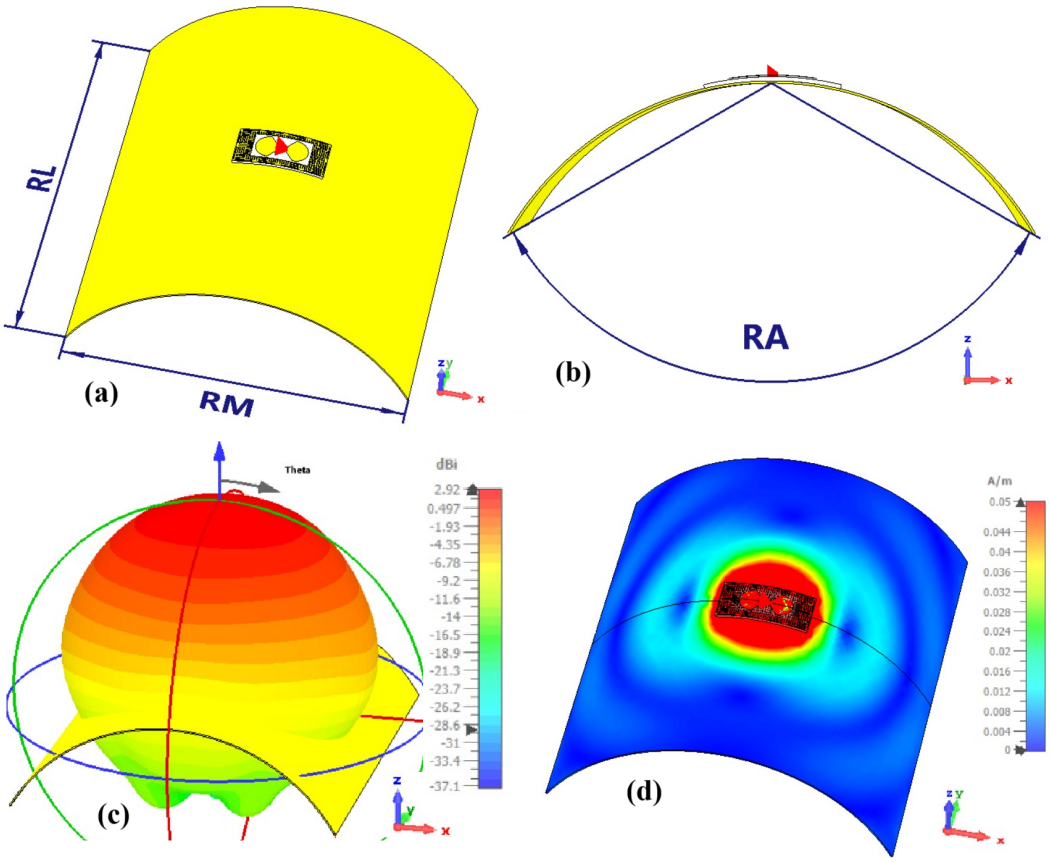

Figure 5.12 Proposed antenna large curved surface placement and simulated results (a) Placement on large curved metal surface with length RL = 2.3 meters and width RM = 1.9 meters, (b) Placement side view with curve angle RA = 120 degrees, (c) 3D gain plot at 0.335 GHz, and (d) Surface currents at 0.335 GHz.

radiation patterns of the proposed antenna placed on the large flat and curved surfaces, as shown in Figure 5.11(f) and Figure 5.12(c) respectively. The gain of the antenna placed on the cylindrical metal ground is slightly decreased to 2.19 dB at 0.335 GHz as compared to the gains of 2.92 dB and 3.21 dB of the antenna placed on the curved and flat ground planes respectively. These gain values of the proposed antenna placed on the flat, curved and cylindrical large metal ground plane is more than the 2 dB gain, that is more than the required 0 dB to 2 dB gain of the glideslope instrument landing system antennas [71].

The proposed antenna radiation characteristics are verified on the large flat and conformal surfaces and in the next step the antenna is conformed and placed on the curved surface of the Bombardier Global 5500 aircraft for the verification of the radiation characteristics. The aircraft used for the verification of the proposed antenna radiation characteritics is shown in Figure 5.14(a) and its 3D model used for the simulation is shown in Figure 5.14(b). The

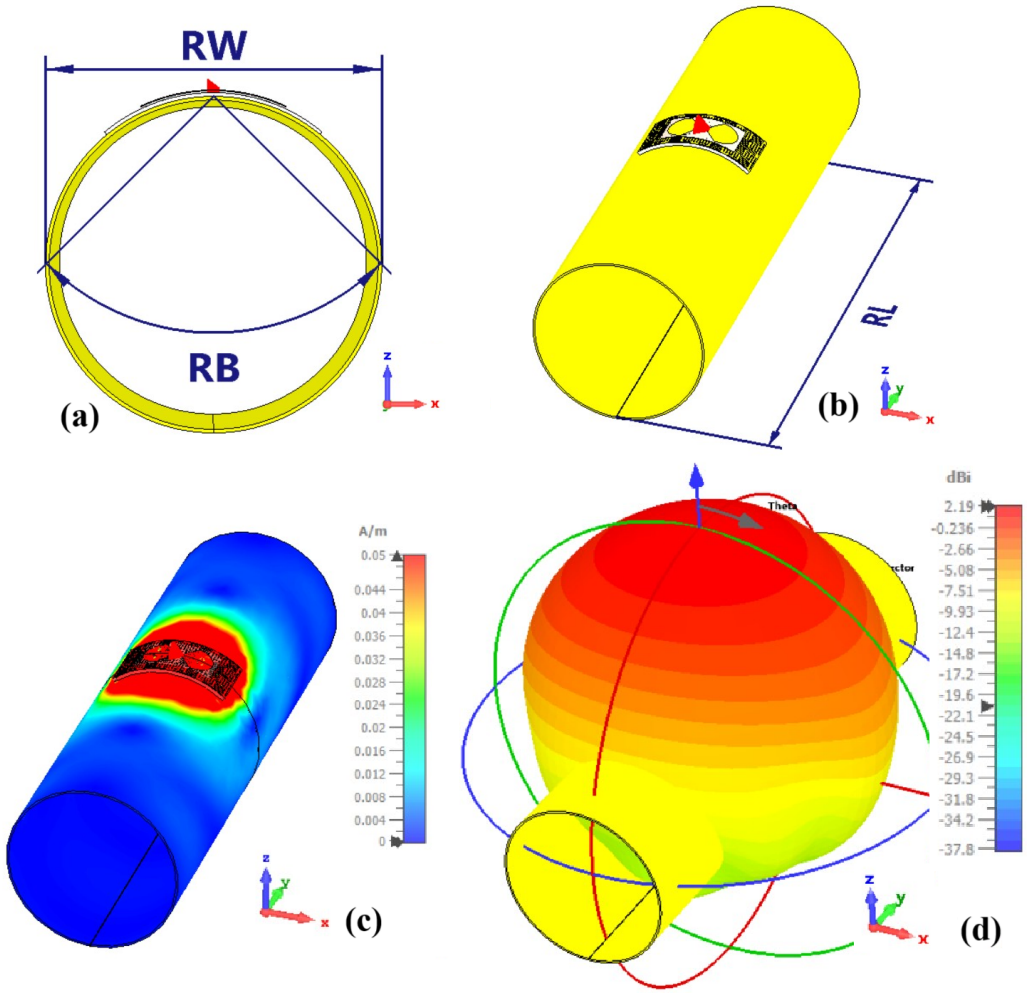

Figure 5.13 Proposed antenna large cylindrical surface placement and simulated results (a) Placement side view with diameter of RW = 0.73 meters and cylindrical center angle of RB = 90 degrees, (b) Placement front view with length RL = 2.3 meters, (c) Surface currents at 0.335 GHz, and (d) 3D gain plot at 0.335 GHz.

glideslope instrument landing system antenna communicates for navigation of the aircraft during landing. Therefore, the proposed ILS glideslope antenna is placed under the nose of the aircraft, as shown in zoomed 3D model of the aircraft front side in Figure 5.14(c). The simulations are done in CST Microwave Studio and frequency domain solver is used for the simulations without the balun and direct feed excitation. The simulated 2D radiation pattern of the proposed antenna placed under the nose of the aircraft with and without the IDC EBG is shown in Figure 5.14(d), in the red and blue curves respectively. The gain of the proposed antenna without the IDC EBG is -7.16 dB and the gain of he proposed antenna with IDC EBG is 4.32 dB as shown in Figure 5.14(d). The proposed antenna maintains its

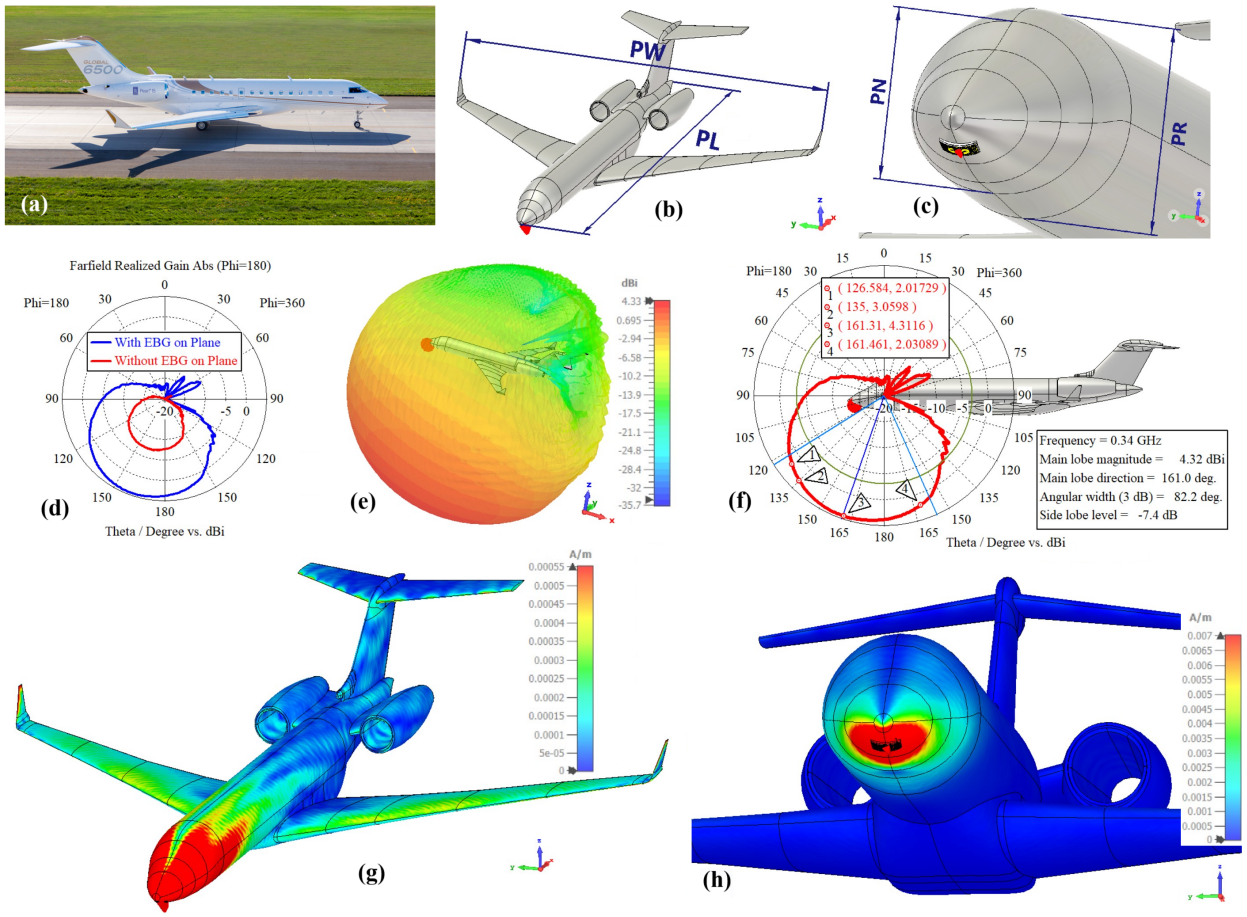

Figure 5.14 Proposed antenna aircraft placement and simulated results (a) Aircraft [40], (b) Aircraft 3D model fuselage length PL = 26.00 meters and wingspan PW = 28.37 meters (c) Proposed antenna placement under aircraft nose, fuselage diameter PR = 2.77 meters, front section diameter PN = 2.31 meters, (d) 2D radiation pattern with and without EBG, (e) 3D gain plot, (f) 2D gain plot details, (g) Surface currents, and (h) Surface currents zoomed view.

directional radiation pattern characteristics when placed on the curved profile aircraft surface and is similar to the radiation pattern plots of the antenna placed on the large flat and conformal metal planes as shown in Figure 5.14(e).

The details of the 2D radiation pattern is shown in Figure 5.14(f), with the peak gain of 4.3 dB at an angle of 160.8 degrees and required gain of more than 0 dB [71], from 114 degrees to 151 degrees. The surface current plots of the proposed antenna on the aircraft are shown in Figure 5.14(g) and zoomed aircraft front area in Figure 5.14(h).

5.7 Conclusion

Low profile printed IDC EBG bowtie antenna is presented in this chapter. The antenna is designed for instrument landing system (ILS) glideslope applications, and the antenna is designed with operational bandwidth from 0.326 GHz to 0.337 GHz with VSWR 6:1 ratio and covers the ILS glideslope band of 0.329 GHz to 0.335 GHz according to the systems requirements from MOPS. Printed bowtie antenna is designed with frequency band from 0.301 GHz to 0.338 GHz and IDC EBG is designed with band of operation from 0.328 GHz to 0.337 GHz. The designed EBG is placed in between the proposed antenna and metal ground plane for reinforcing the currents and revival of the radiation pattern. Grounded coplanar waveguide balun is designed for feeding the two arms of the proposed bowtie antenna. The directional radiation pattern of the proposed is simulated and analyzed for large, conformal and cylindrical metal surfaces with peak gains of 3.21 dB, 2.92 dB and 2.19 dB in the ILS band respectively. The proposed antenna is then placed under the nose of the aircraft and the directional radiation pattern characteristics are verified with the peak gain of 4.3 dB. The proposed antenna has a benefit of low profile as compared to the commercial antenna with the total height of 22 mm as compared to commercial antennas that can have height of 175 mm [72]. The next step is the fabrication of the proposed antenna and verification of the radiation pattern and frequency response on large flat and cylindrical metal surface.

CHAPTER 6 CONCLUSION

6.1 Summary of Works

Antennas for avionics applications are designed, fabricated and tested for DME, TCAS, ADS-B and RadAlt systems. Low profile RadAlt antenna is designed for frequency band of 4.06 GHz to 4.53 GHz and gain of more than 12 dB in the band of operation by designing stacked patch array. Low sidelobe levels less than -40 dB are achieved by designing novel one-dimensional layered electromagnetic bandgap circular structure and is used to suppress the surface currents in the H-plane that is used as forward direction and placement of the transmit and receive antennas under the fuselage. The isolation of 111 dB is achieved at 4.28 GHz and average of 84.65 dB in the whole band of operation from 4.2 GHz to 4.4 GHz. The proposed RadAlt antenna has benefits of enhanced bandwidth and better signal to interference ratio as compared to commercial antennas due to reduced sidelobe levels and increased gain.

Single antenna concept is proposed for DME, TCAS, ADS-B and RadAlt avionics applications and one-port and two-port fed antennas are designed. Two separate feeding paths are designed in the two-port fed antenna for separately feeding in isolation the lower L-band cavity and upper C-band patch array. In one-port fed antenna, a novel Three-dimensional power splitter is designed for feeding both the lower L-band cavity and upper C-band patch array. The lower placed cavity is excited by using circular ring placed at the center of the cavity and upper placed patch array is fed by a feeding path from the splitter. RadAlt currents inside the cavity are suppressed at RadAlt frequency band by designing electromagnetic bandgap layer of 8 x 8 cells in the frequency band range of 4.2 GHz to 4.4 GHz and placing it inside the bottom of the C-band cavity. Frequency band of 0.96 GHz to 1.215 GHz is achieved with omni-directional radiation characteristics for the TCAS, DME and ADS-B applications from the lower C-band cavity. The proposed antenna presents a single antenna design providing benefits of reduced drag, cost, weight and size on the aircraft, as compared to commercially available antennas. The proposed antenna now provides the possibility of integrating this single antenna for TCAS, DME, ADS-B and RadAlt with software defined avionics radio.

Low profile printed bowtie antenna for instrument landing system (ILS) glideslope applications is designed by closely placing with the ground plane and achieving gain of 5 dB for the frequency band of operation from 329 MHz to 335 MHz. Printed bowtie antenna is designed for compact structure as compared to printed dipole antenna.

Figure 6.1 Proposed RadAlt and DME-TCAS-RadAlt antennas flight testing aircraft and placements (a) Antennas placement under aircraft fuselage, (b) Bottom view of antennas placement under aircraft fuselage.

Interdigital capacitor structured electromagnetic bandgap is designed and placed in between the bowtie antenna and metal ground plane for cancelling reflections from the ground plane and reinforcing the currents for revival of the radiation pattern. and large aircraft metallic fuselage. Proposed antenna is placed on large and cylindrical metal surfaces for the verification of the directional radiation pattern. The antenna is also conformed with aircraft fuselage profile and placed under the nose and directional radiation pattern characteristics are verified. The proposed antenna provides benefit of low profile as compared to the commercial glideslope antennas, and that can also be conformed with the airframe of the aircraft.

6.2 Future Research

Proposed RadAlt and DME-TCAS-RadAlt antennas flight testing were performed for the verification of system level parameters and performance. The aircraft used for the flight testing and the placement of our proposed antennas under the aircraft fuselage are shown in Figure 6.1(a), and the bottom view of the placed antennas on the panel under the aircraft fuselage in shown in Figure 6.1(b). The proposed antennas were tested during the flight and real time system parameters of received power (PRx), transmitted power (PTx) and received signal strength indicator (RSSI) were recorded. The next step is the flight-testing data analysis and the acquired system parameters from flight-testing are currently being analyzed and processed by the ETS team. In the next stage of the project, the proposed antennas will be integrated with the software defined avionics radio.

The objectives and next steps for the development of low profile Instrument landing antenna for glideslope applications will be for designing small scale version of the current proposed antenna for the verification of the antenna radiation patterns placed on large metallic planes. For the smaller scale version of the current ILS antenna, the antenna will be restructured for the frequency response to be in the higher frequency of S-band within 2 GHz to 4 GHz range. In the next step, the proposed ILS antenna will also be fabricated at the desired frequency of operation 329 MHz to 335 MHz.

All the proposed antennas were designed assuming ideal weather conditions. In practice, antennas have to operate for many years under harsh weather and icing conditions. Therefore, to make these antennas practical, an extra step in the design would be to ruggedize these structures by adding radomes. This would involve choosing the radome materials (often multilayer dielectrics), retune the antennas to have good matching in presence of the radome, choose an appropriate radome fabrication technique. More tests and design cycles will be necessary for optimizing the frequency response and radiation characteristics.

REFERENCES

[1] *United States Federal Aviation Administration RTCA*, Std. Document RTCA DO-189, 1985.

[2] *United States Federal Aviation Administration RTCA*, Std. Document RTCA DO-155, 1974.

[3] *United States Federal Aviation Administration RTCA*, Std. Document RTCA DO-144A, 1970.

[4] *United States Federal Aviation Administration RTCA*, Std. Document RTCA DO-260B, 2009.

[5] *United States Federal Aviation Administration RTCA*, Std. Document RTCA DO-282B, 2009.

[6] *United States Federal Aviation Administration RTCA*, Std. Document RTCA DO-143, 1970.

[7] *United States Federal Aviation Administration RTCA*, Std. Document RTCA DO-195, 1986.

[8] *United States Federal Aviation Administration RTCA*, Std. Document RTCA DO-192, 1986.

[9] T. M. Macnamara, *Introduction to Antenna Placement and Installation.* John Wiley and Sons, Ltd., 2010.

[10] D. Chaturvedi, A. Kumar, and S. Raghavan, "An integrated siw cavity-backed slot antenna-triplexer," *IEEE Antennas and Wireless Propagation Letters*, vol. 17, no. 8, pp. 1557–1560, 2018.

[11] A. Chen, X. Ying, and K. Ding, "A compact antenna of radio altimeters based on bi-layer substrate technology," in *2013 5th IEEE International Symposium on Microwave, Antenna, Propagation and EMC Technologies for Wireless Communications*, 2013, pp. 402–405.

[12] Jan 2022. [Online]. Available: https://moniem-tech.com/2022/01/20/summary-of-the-5g-interfering-with-aviation-safety-in-the-us/

[13] [Online]. Available: https://www.sensorantennas.com/wp-content/uploads/2023/11/S67-2002.pdf

[14] Y.-X. Guo *et al.*, "Wide-band l-probe fed circular patch antenna for conical-pattern radiation," *IEEE Transactions on Antennas and Propagation*, vol. 52, no. 4, pp. 1115–1116, 2004.

[15] K. Lau and K. Luk, "A wide-band monopolar wire-patch antenna for indoor base station applications," *IEEE Antennas and Wireless Propagation Letters*, vol. 4, pp. 155–157, 2005.

[16] J. Liu *et al.*, "Design and analysis of a low-profile and broadband microstrip monopolar patch antenna," *IEEE Transactions on Antennas and Propagation*, vol. 61, no. 1, pp. 11–18, 2013.

[17] Q. Hou *et al.*, "Effective magnetic-loop array antennas with enhanced bandwidth," *IEEE Transactions on Antennas and Propagation*, vol. 64, no. 8, pp. 3717–3722, 2016.

[18] L. Akhoondzadeh-Asl *et al.*, "Novel low profile wideband monopole antenna for avionics applications," *IEEE Transactions on Antennas and Propagation*, vol. 61, no. 11, pp. 5766–5770, 2013.

[19] C. C. M. Kim, C. Park and S. Jun, "A multi-band smart skin antenna design for flight demonstration," *The 8th European Conference on Antennas and Propagation (EuCAP 2014)*, pp. 2855–2859, 2014.

[20] L. Rufail and J. J. Laurin, "Aircraft cavity-backed nonprotruding wideband antenna," *IEEE Antennas and Wireless Propagation Letters*, vol. 11, pp. 1108–1111, 2012. [Online]. Available: https://ieeexplore.ieee.org/document/6296676

[21] "Fly The Wing — flythewing.com," https://flythewing.com/308/Blog/Entries/2014/4/14_Airplane_Antennae.html, [Accessed 28-03-2025].

[22] A. Ikram and J.-J. Laurin, "On the increase of the directivity of a low profile aircraft antenna," in *The 8th European Conference on Antennas and Propagation (EuCAP 2014)*, 2014, pp. 338–342.

[23] P. K. S. Debajit De, "Design and development of a multi-feed end-fired microstrip antenna for tcas airborne system," *Progress In Electromagnetics Research C*, vol. 78, pp. 69–81, 2017.

[24] L. Akhoondzadeh-Asl, J. J. Laurin, and A. Mirkamali, "A novel low-profile monopole antenna with beam switching capabilities," *IEEE Transactions on Antennas and Propagation*, vol. 62, no. 3, pp. 1212–1220, 2014.

[25] "TAS — flyingbulls.at," https://www.flyingbulls.at/en/stories/tas, [Accessed 30-03-2025].

[26] [Online]. Available: https://www.sensorantennas.com/wp-content/uploads/2023/11/S72-1746-1.pdf

[27] [Online]. Available: https://www.sensorantennas.com/wp-content/uploads/2023/11/S65-5366-735.pdf

[28] "Marker Antenna - HR Smith Group of Companies — hr-smith.com," https://www.hr-smith.com/antennas/marker-antenna/, [Accessed 31-03-2025].

[29] https://x.com/laird_kay/status/868861873457954817, [Accessed 31-03-2025].

[30] "VOR/LOC Loop Antenna - HR Smith Group of Companies — hr-smith.com," https://www.hr-smith.com/antennas/vor-loc-loop-antenna/, [Accessed 31-03-2025].

[31] "Glide Slope antenna - HR Smith Group of Companies — hr-smith.com," https://www.hr-smith.com/antennas/glide-slope-antenna-4/, [Accessed 31-03-2025].

[32] [Online]. Available: https://www.aircraftspruce.ca/catalog/avpages/comant158c.php

[33] D. Sievenpiper *et al.*, "High-impedance electromagnetic surfaces with a forbidden frequency band," *IEEE Transactions on Microwave Theory and Techniques*, vol. 47, no. 11, pp. 2059–2074, 1999.

[34] F.-R. Yang *et al.*, "A novel tem waveguide using uniplanar compact photonic-bandgap (uc-pbg) structure," *IEEE Transactions on Microwave Theory and Techniques*, vol. 47, no. 11, pp. 2092–2098, 1999.

[35] D. Kern *et al.*, "The design synthesis of multiband artificial magnetic conductors using high impedance frequency selective surfaces," *IEEE Transactions on Antennas and Propagation*, vol. 53, no. 1, pp. 8–17, 2005.

[36] H. S. Farahani *et al.*, "Mutual coupling reduction in patch antenna arrays using a uc-ebg superstrate," *IEEE Antennas and Wireless Propagation Letters*, vol. 9, pp. 57–59, 2010.

[37] L. Peng, C.-l. Ruan, and J. Xiong, "Compact ebg for multi-band applications," *IEEE Transactions on Antennas and Propagation*, vol. 60, no. 9, pp. 4440–4444, 2012.

[38] S. Yan, P. J. Soh, and G. A. E. Vandenbosch, "Low-profile dual-band textile antenna with artificial magnetic conductor plane," *IEEE Transactions on Antennas and Propagation*, vol. 62, no. 12, pp. 6487–6490, 2014.

[39] D. M. Pozar, *Microwave Engineering, 4th Edition*. Wiley, November 2011.

[40] [Online]. Available: https://bombardier.com/en/media/news/bombardier-celebrates-entry-service-global-6500-jet

[41] A. Amrhar *et al.*, "Multi-mode reconfigurable software defined radio architecture for avionic radios," in *2017 Integrated Communications, Navigation and Surveillance Conference (ICNS)*, 2017, pp. 2D1–1–2D1–10.

[42] C. Wang, Y. Chen, and S. Yang, "Application of characteristic mode theory in hf band aircraft-integrated multiantenna system designs," *IEEE Transactions on Antennas and Propagation*, vol. 67, no. 1, pp. 513–521, 2019.

[43] A. Vukovic, P. Sewell, and T. M. Benson, "Holistic appraisal of modeling installed antennas for aerospace applications," *IEEE Transactions on Antennas and Propagation*, vol. 67, no. 3, pp. 1396–1409, 2019.

[44] [Online]. Available: https://www.lightningdiversion.com/diversionstrips.aspx

[45] W. Zhang *et al.*, "A pattern-reconfigurable aircraft antenna with low wind drag," *IEEE Transactions on Antennas and Propagation*, vol. 68, no. 6, pp. 4397–4405, 2020.

[46] P. Liu *et al.*, "Omnidirectional dual-polarized antenna with sabre-like structure," *IEEE Transactions on Antennas and Propagation*, vol. 65, no. 6, pp. 3221–3225, 2017.

[47] G. Byun *et al.*, "Design of aircraft on-glass antennas using a coupled feed structure," *IEEE Transactions on Antennas and Propagation*, vol. 60, no. 4, pp. 2088–2093, 2012.

[48] M. D. Wright *et al.*, "Mems reconfigurable broadband patch antenna for conformal applications," *IEEE Transactions on Antennas and Propagation*, vol. 66, no. 6, pp. 2770–2778, 2018.

[49] A. Nekrassov, "On airborne measurement of the sea surface wind vector by a scatterometer (altimeter) with a nadir-looking wide-beam antenna," *IEEE Transactions on Geoscience and Remote Sensing*, vol. 40, no. 10, pp. 2111–2116, 2002.

[50] C. A. Balanis, *Antenna Theory: Analysis and Design*. USA : Wiley-Interscience, 2005.

[51] S. Targonski, R. Waterhouse, and D. Pozar, "Design of wide-band aperture-stacked patch microstrip antennas," *IEEE Transactions on Antennas and Propagation*, vol. 46, no. 9, pp. 1245–1251, 1998.

[52] [Online]. Available: https://www.sensorantennas.com/wp-content/uploads/2024/07/S65-5366-895L.pdf

[53] S. Wittevrongel, "Nouvelles antennes à profil bas multi-standards pour application aéronautique," mémoire de maîtrise, Dép. de génie Aérospatial, École Polytechnique de Montréal, Montréal, QC, 2020. [Online]. Available: https://publications.polymtl.ca/5356/

[54] A. Ikram and J.-J. Laurin, "Reducing the height of a monopole antenna by using magneto dielectric material," in *2016 17th International Symposium on Antenna Technology and Applied Electromagnetics (ANTEM)*, 2016, pp. 1–2.

[55] B. P. S. Kemkemian, I. Naneix S. Mallegol and C. Renard, "Wideband and very wideband thin structural tiles for airborne active antennas," *2013 7th European Conference on Antennas and Propagation (EuCAP), Gothenburg*, pp. 2744–2747, 2013.

[56] X. Tan *et al.*, "Enhancing isolation in dual-band meander-line multiple antenna by employing split ebg structure," *IEEE Transactions on Antennas and Propagation*, vol. 67, no. 4, pp. 2769–2774, 2019.

[57] A. A. Megahed *et al.*, "Sub-6 ghz highly isolated wideband mimo antenna arrays," *IEEE Access*, vol. 10, pp. 19 875–19 889, 2022.

[58] S. Dey, S. Dey, and S. K. Koul, "Isolation improvement of mimo antenna using novel ebg and hair-pin shaped dgs at 5g millimeter wave band," *IEEE Access*, vol. 9, pp. 162 820–162 834, 2021.

[59] A. Khan *et al.*, "Mutual coupling reduction using ground stub and ebg in a compact wideband mimo-antenna," *IEEE Access*, vol. 9, pp. 40 972–40 979, 2021.

[60] Y. Liu *et al.*, "A low correlation and mutual coupling mimo antenna," *IEEE Access*, vol. 7, pp. 127 384–127 392, 2019.

[61] X. Shen *et al.*, "A miniaturized microstrip antenna array at 5g millimeter-wave band," *IEEE Antennas and Wireless Propagation Letters*, vol. 18, no. 8, pp. 1671–1675, 2019.

[62] F. Yang and Y. Rahmat-Samii, "Microstrip antennas integrated with electromagnetic band-gap (ebg) structures: a low mutual coupling design for array applications," *IEEE Transactions on Antennas and Propagation*, vol. 51, no. 10, pp. 2936–2946, 2003.

[63] O. Q.-T. E. Rajo-Iglesias and L. Inclan-Sanchez, "Mutual coupling reduction in patch antenna arrays by using a planar ebg structure and a multilayer dielectric substrate," *IEEE Transactions on Antennas and Propagation*, vol. 56, no. 6, pp. 1648–1655, 2008.

[64] J.-Y. Lee, S.-H. Kim, and J.-H. Jang, "Reduction of mutual coupling in planar multiple antenna by using 1-d ebg and srr structures," *IEEE Transactions on Antennas and Propagation*, vol. 63, no. 9, pp. 4194–4198, 2015.

[65] S. D. Assimonis, T. V. Yioultsis, and C. S. Antonopoulos, "Design and optimization of uniplanar ebg structures for low profile antenna applications and mutual coupling reduction," *IEEE Transactions on Antennas and Propagation*, vol. 60, no. 10, pp. 4944–4949, 2012.

[66] S. Robin and Y. Klein, "Laterally isolated microstrip antenna," Patent application US4 460 894A, 17 July, 1984. [Online]. Available: https://patents.google.com/patent/US4460894A/en

[67] [Online]. Available: https://chelton.com/media/ujoleyiz/chelton-20-21-radalt-patchantenna.pdf

[68] D. Chaturvedi *et al.*, "Siw cavity-backed antenna-triplexer for radio altimeter/wi-fi applications," in *2018 IEEE Indian Conference on Antennas and Propogation (InCAP)*, 2018, pp. 1–3.

[69] [Online]. Available: https://vspu.larc.nasa.gov/

[70] O. M. Khan and J.-J. Laurin, "High isolation and band enhanced radio altimeter antenna for avionics applications," *IEEE Open Journal of Antennas and Propagation*, vol. 5, no. 6, pp. 1592–1597, 2024.

[71] [Online]. Available: https://www.l3harris.com/all-capabilities/n4-17-series-vor-loc-glide-slope-antenna

[72] [Online]. Available: https://www.sensorantennas.com/product/glide-slope-antenna-3/

[73] L. Le Coq *et al.*, "Printed bowtie antenna fed by electromagnetic coupling," in *IEEE Antennas and Propagation Society International Symposium. 1999 Digest. Held in conjunction with: USNC/URSI National Radio Science Meeting (Cat. No.99CH37010)*, vol. 4, 1999, pp. 2710–2713 vol.4.